

Separated Spacecraft Interferometry – System Architecture Design and Optimization

by

Cyrus D. Jilla

B.S. Aerospace Engineering
University of Virginia, 1996

Submitted to the Department of Aeronautics and Astronautics
in partial fulfillment of the requirements for the degree of

Master of Science in Aeronautics and Astronautics
at the

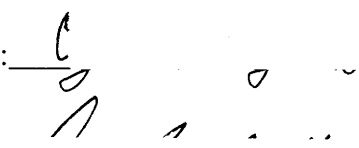
MASSACHUSETTS INSTITUTE OF TECHNOLOGY

February 1999

© 1999 Cyrus D. Jilla. All rights reserved.

The author hereby grants MIT permission to reproduce and distribute publicly
paper and electronic copies of this thesis in whole or in part.

Signature of Author: _____




Department of Aeronautics and Astronautics
December 17, 1998

Certified by: _____

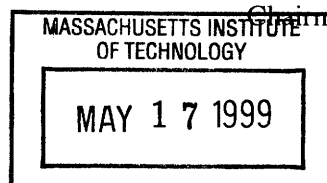


David W. Miller
Assistant Professor of Aeronautics and Astronautics
Thesis Supervisor

Accepted by: _____



Jaime Peraire
Associate Professor of Aeronautics and Astronautics
Chairman, Department Graduate Committee



Separated Spacecraft Interferometry – System Architecture Design and Optimization

by

Cyrus D. Jilla

Submitted to the Department of Aeronautics and Astronautics
On December 17, 1998 in Partial Fulfillment of the Requirements
For the Degree of Master of Science in Aeronautics and Astronautics

ABSTRACT

Through a process of system design, analysis, and optimization, the trade space for future optical separated spacecraft interferometers (SSI's) is explored. Using Distributed Satellite System principles, eleven separate architectures ranging in size from three to five spacecraft are compared on the basis of four metrics: 1) capability, 2) performance, 3) adaptability, and 4) cost per function. The independent SSI architecture variables include the total number of spacecraft, the type of spacecraft, the number of combiner payloads, and the number of collector payloads. Architecture variables held constant in this study, but which may be varied in future studies, include the array's geometric configuration, the maximum baseline, the mass and power requirements of each payload, the spacecraft propulsion system, the component failure rates, and the mission design life. Three models are developed and coupled to analyze each architecture. A capability model calculates the instantaneous u-v coverage, image quality, angular resolution, and imaging rate of each proposed architecture. The reliability model uses combinatorial analysis and Markov techniques to determine both the probability that the system will continue to function over a given amount of time and the likelihood with which the system will function in different partially failed states throughout the mission. The reliability model is then coupled with the capability model to calculate total performance over the mission lifetime. The cost model, which is divided into payload, spacecraft bus, launch, and operations costs, estimates the total lifecycle cost of each architecture. On the basis of the cost per synthesized image metric, two architectures were identified as providing the greatest value for the money. The design features in order of importance are imaging rate, total system cost, and total system reliability.

Thesis Supervisor: David W. Miller

Title: Assistant Professor of Aeronautics and Astronautics

Acknowledgements

“Good friends are good for your health.”

- Dr. Irwin Sarason

There are many individuals who deserve credit for supporting this work and the author. This is a special thanks to those people.

I owe a very large thanks to Professor David Miller for allowing me to do this research. Professor Miller has given me the opportunity and tools to contribute to the MIT Space Systems Lab (SSL), and I intend to do so. Professor Miller is not afraid to give his students responsibility, enabling them to develop professionally and contribute to the field of aerospace engineering in the process. Thanks also to SharonLeah Brown for always being there to make sure everything goes smoothly, and to help smooth out the bumps during those inevitable bumpy times. I also owe a debt of gratitude to Peggy Edwards for always being so helpful.

I would also like to thank the two cosponsors of this work. The NASA Advanced Concepts Research Project (ACRP) with MIT on Advanced Spacecraft Architectural Concepts supported this work : Grant # NAGI-1839 under the supervision of Mr. Brantley Hanks as the technical monitor. The Air Force Research Lab for Grand Challenges in Space Technology: Distributed Satellite Systems – Contract # F29601-97-K-0010 under the technical supervision of Lt. George Schneiderman and Dr. Jim Skinner also supported this work.

I would like to thank Dr. Graeme “The Father of Distributed Satellite Systems” Shaw. Graeme not only developed the foundation for the analysis used in this work, but was also always there to provide support, read and critique work, and create a fun environment to work in. I would also like to thank Edmund “Computer Super-Genius” Kong for being my constant computer consultant technician for the past two years. No mess I ever made on a PC was too big for Edmund to fix. All of the other members of the SSL deserve an appreciative thank you for making the lab a fun place to work.

I would also like to thank all of my Professors at the University of Virginia for preparing me to attend MIT and do significant work. Dr. Earl Thornton merits special mention for always being enthusiastic about my future plans, giving sage advice, and easing my transition from UVA to MIT during my first semester.

I thank all of my mentors from summer jobs at the NASA Marshal Space Flight and Langley Research Centers for teaching me how our country’s space program really works. While there are too many people from these two institutions to mention here, I would like to earnestly thank Don Monell for imparting to me the importance of balancing a fulfilling family life with one’s professional work.

Finally, I would like to thank my family for their constant, unending love and support over the years as I work towards my goals and dreams in life. I dedicate this thesis to them. I would also like to thank those I think of as my extended family, ZAGBA, for embracing me into the Boston community, always being there for me, and helping to provide some balance, perspective, and fun over the past two years.

Biographical Note

“Work to the best of your ability, fulfill your potential, and learn.”

- Anonymous

Cyrus D. Jilla was born February 7, 1974. He graduated jointly from the Roanoke Valley Governor’s School for Science and Technology and Northside High School as Valedictorian in June of 1992. That fall, Jilla then entered the University of Virginia as a Walter S. Rodman Scholar. At The University he acted as president of Sigma Gamma Tau, cofounded the Space Advancement Society, and served as team leader of the 1995-96 1st place UVA AIAA/Loral Space Design Team. He graduated from The University Summa Cum Laude in May 1996 with a Bachelor’s of Science degree, ranking 1st in the graduating Aerospace Engineering class. Jilla spent the summer of 1995 in the NASA ACADEMY Leadership Development Program at the NASA Marshall Space Flight Center, where he served as a research assistant on a project to improve the quality of remotely sensed imagery, met with Senior NASA officials, toured NASA facilities at several field centers, and gained an inside view of how America’s Space Program works via the interaction of government, academia, and the private sector. Jilla then worked on software tools to aid in the design and simulation of spacecraft in the Space Systems and Concepts Division of the NASA Langley Research Center during the summer of 1996. Jilla entered the Massachusetts Institute of Technology September 1996, where he currently works as a research assistant in the Space System Laboratory teaming on projects in distributed satellite systems/constellations, modular & multifunctional spacecraft design, and space-based interferometry. He is a student member of the American Institute of Aeronautics and Astronautics (AIAA), a member of the Planetary Society, a member of the Tau Beta Pi engineering honor society, a member of the Sigma Gamma Tau aerospace engineering honor society, a member of the Sigma Xi honor society for pure and applied science and engineering research, and an associate member of the AIAA Space Systems Technical Committee. Following the completion of an S.M. degree from MIT in February 1999, Jilla will begin work on his PhD. in Aeronautics and Astronautics with the intention to help shape the future of humanity in space.

Publications:

Jilla, C.D., and Miller, D.W. *A Reliability Model for the Design and Optimization of Separated Spacecraft Interferometer Arrays*. Proceedings of the 11th AIAA/USU Conference on Small Satellites. AIAA Paper SSC97-XI-2. September 1997.

Jilla, C.D., and Miller, D.W. *Satellite Design: Past, Present, and Future*. International Journal of Small Satellite Engineering. Vol. 1, Issue 1. ISSN 1360-7014. July 1997.

Mallory, G.J., Jilla, C.D., and Miller, D.W. *Optimization of Geosynchronous Satellite Constellations for Interferometric Earth Imaging*. Proceedings of the 1998 AIAA/AAS Astrodynamics Specialist Conference. Paper AIAA-98-4379. August 1998.

Table of Contents

| | |
|---|----|
| Chapter 1..... | 15 |
| Introduction..... | 15 |
| 1.1 Background..... | 16 |
| 1.1.1 Civilian Applications – Astronomy..... | 18 |
| 1.1.2 Military Applications – Surveillance..... | 20 |
| 1.2 Motivation and Objectives..... | 21 |
| 1.3 Outline..... | 24 |
| Chapter 2..... | 25 |
| Interferometry Fundamentals..... | 25 |
| 2.1 What is Interferometry?..... | 25 |
| 2.2 The Physics of Optical Interferometry..... | 28 |
| 2.3 Synthetic Imaging..... | 31 |
| 2.4 Summary..... | 33 |
| Chapter 3..... | 35 |
| System Analysis Methodology..... | 35 |
| 3.1 Define System Requirements..... | 38 |
| 3.1.1 Identifying the Customer..... | 38 |
| 3.1.2 Define the Customer Requirements..... | 39 |
| 3.2 Define Capability Requirements..... | 40 |
| 3.3a Develop System Metrics..... | 41 |
| 3.3a.1 Cost Per Function..... | 41 |
| 3.3a.2 Performance..... | 42 |
| 3.3a.3 Adaptability..... | 42 |
| 3.3b Functional Analysis..... | 43 |
| 3.3b.1 Model the System as a Network..... | 43 |
| 3.3b.2 Identification of the Key Design Parameters..... | 43 |
| 3.4 Derive Top-Level Architecture(s)..... | 45 |
| 3.5 Evaluate Architecture(s)..... | 45 |
| 3.6 Select Final Architecture..... | 46 |
| 3.7 Summary..... | 46 |
| Chapter 4..... | 47 |
| Capability Model..... | 47 |
| 4.1 Integrity – u-v Coverage and Image Quality..... | 48 |
| 4.1.1 u-v Coverage..... | 48 |
| 4.1.2 Image Quality..... | 50 |
| 4.2 Isolation - Angular Resolution..... | 53 |
| 4.3 Rate - Imaging Rate..... | 54 |
| 4.3.1 Modeling Imaging Rate..... | 54 |
| 4.3.2 Snapshot Imaging Results..... | 61 |

| | |
|--|-----|
| 4.3.3 High Resolution Imaging Results – Part 1..... | 62 |
| 4.3.4 High Resolution Imaging Results – Part 2..... | 66 |
| 4.4 Availability – Percentage of Time Imaging..... | 67 |
| 4.5 Capability Model Summary..... | 67 |
| Chapter 5..... | 69 |
| Reliability Model..... | 69 |
| 5.1 Background..... | 70 |
| 5.2 Total System Reliability..... | 71 |
| 5.3 Markov Modeling..... | 77 |
| 5.4 Reliability Model Summary..... | 85 |
| Chapter 6..... | 87 |
| Cost Model..... | 87 |
| 6.1 Background..... | 88 |
| 6.2 Payload Cost Model..... | 89 |
| 6.3 Spacecraft Bus Cost Model..... | 90 |
| 6.4 Learning Curve..... | 92 |
| 6.5 Launch Cost Model..... | 93 |
| 6.6 Operations Cost Model..... | 95 |
| 6.7 Cost Model Summary..... | 96 |
| Chapter 7..... | 97 |
| System Architecture Results..... | 97 |
| 7.1 Architectures Analyzed..... | 97 |
| 7.2 System Architecture Design and Optimization Process..... | 99 |
| 7.3 Model Outputs and the Cost Per Function Metrics..... | 100 |
| 7.3.1 Reliability..... | 101 |
| 7.3.2 Performance..... | 102 |
| 7.3.3 Cost..... | 103 |
| 7.3.4 Cost Per Function..... | 105 |
| 7.3.5 Architecture Rankings..... | 106 |
| 7.4 Uncertainty Analysis..... | 107 |
| 7.4.1 Spacecraft Bus Cost..... | 107 |
| 7.4.2 Learning Curve..... | 108 |
| 7.4.3 Failure Rates..... | 109 |
| 7.5 Sensitivity Analysis..... | 110 |
| 7.5.1 Costs..... | 111 |
| 7.5.2 Learning Curve Slope..... | 112 |
| 7.5.3 Component Reliability..... | 113 |
| 7.5.4 Imaging Rate..... | 113 |
| 7.5.5 Mission Design Life..... | 114 |
| 7.6 Results Summary..... | 115 |
| Chapter 8..... | 117 |
| Conclusions..... | 117 |

References..... 123

Appendix A: u-v Coverage Results.....127

Appendix B: Imaging Rate Results.....139

Appendix C: Markov Model Results.....145

Appendix D: Cost Model Results.....151

List of Figures

| | |
|---|-----|
| Figure 1.1: Two Proposed Space-Based Single Satellite (a) [JPL, 1998] and Multiple Satellite (b) [ESA, 1998]..... | 17 |
| Figure 1.2: Resolutions Enabled by Different Space-Based Observatories..... | 19 |
| Figure 1.3: Deep Space 3 Mission Concept [Colavita et al, 1996]..... | 19 |
| Figure 1.4: Ground Resolution of a Nadir Looking Single Aperture Telescope or Separated Spacecraft..... | 20. |
| Figure 2.1: Angular Resolution of the Hubble Space Telescope vs. Proposed Space-Based Interferometers..... | 26 |
| Figure 2.2: Geometry Between Two Collectors in an Optical Interferometer..... | 29 |
| Figure 2.3: Point Spread Function for an Irregularly Sampled u-v Plane..... | 33 |
| Figure 3.1: The Systems Engineering and Architecting Process..... | 36 |
| Figure 4.1: 8 Collector Spacecraft Cornwell Array (a) and Associated u-v Coverage (b)..... | 49 |
| Figure 4.2: Snapshot Sampling of 21 Spatial Frequencies by 5 Collector Cornwell Array (a), and a 5 Collector Randomly Spaced Circular Array..... | 50 |
| Figure 4.3: Snapshot PSF for a 5 Collector Cornwell Array (a) and a Hypothetical Filled Aperture (b)..... | 51 |
| Figure 4.4: Normalized Point Spread Function for the Snapshot Image of Four Separate Cornwell..... | 52 |
| Figure 4.5: Optical SSI Temporal Model..... | 55 |
| Figure 4.6: Array Reconfiguration Protocol..... | 57 |
| Figure 4.7: Time to Obtain A Single Snapshot Image for Cornwell Arrays with m Combiner Satellites..... | 61 |
| Figure 4.8: Time to Obtain a Single High Resolution Image, with 100 u-v Points using a Cornwell Array..... | 62 |
| Figure 4.9: Number of Baselines Available Per Configuration (a) and the Total Number of Array..... | 63 |
| Figure 4.10: Reconfiguration Distance Intervals ($B_{max}=1000$ m, 100 u-v points)..... | 64 |
| Figure 4.11: Single Reconfiguration Times (a) and Total Reconfiguration Times (b)..... | 65 |
| Figure 4.12: Theoretical Maximum Number of Images Possible Over a 1 Year Mission – Cornwell Array..... | 66 |
| Figure 4.13: Time Required for a Single High Resolution Image with a Cornwell Array as a Function of the..... | 67 |
| Figure 5.1: Heterogeneous Single Function Spacecraft Design (SFD) (a) and Homogeneous Modular and Multifunctional Spacecraft Design (MAMSC) (b) for a 3 Satellite Interferometer..... | 71 |
| Figure 5.2: Total System Reliability at the End of One Year for SFD and SSI Arrays as a Function of the..... | 74 |
| Figure 5.3: Total System Reliability as a Function of Time and the Number of | |

| | |
|--|-----|
| Combiner (m) Spacecraft (a)..... | 75 |
| Figure 5.4: Total System Reliability as a Function of Time for MAMSC Arrays with n Spacecraft..... | 76 |
| Figure 5.5: Fault Tree for the Three Spacecraft SSI SFD Architecture..... | 78 |
| Figure 5.6: Fault Tree for the Three Spacecraft SSI MAMSC Architecture..... | 78 |
| Figure 5.7: Markov Model for the 3 Spacecraft SSI SFD Architecture | 79 |
| Figure 5.8: Markov Model Results for the 3 Spacecraft SFD and MAMSC Architectures (a) and the Results..... | 84 |
| Figure 6.1: DSS Lifecycle Costs..... | 88 |
| Figure 6.2: Structure of the SSI Cost Model | 89 |
| Figure 6.3: Per Unit Average Cost as a Function of Units Produced for Different Learning Curve Slopes..... | 93 |
| Figure 6.4: Total Launch Cost as a Function of Total SSI Mass..... | 95 |
| Figure 7.1: SSI Architectures Analyzed..... | 98 |
| Figure 7.2: Reliability of the SSI Architectures..... | 101 |
| Figure 7.3: Performance of the SSI Architectures..... | 102 |
| Figure 7.4: Cost of the SSI Architectures..... | 103 |
| Figure 7.5: Cost of the SSI Architectures as a Function of the Number of Combiners in the Array..... | 104 |
| Figure 7.6: Cost Per Function of Each SSI Architecture..... | 105 |
| Figure 7.7: Effect on the Cost Per Image Metric of the Spacecraft Bus Cost Uncertainties in..... | 108 |
| Figure 7.8: Effect on the Cost Per Image Metric of the Learning Curve Slope Uncertainties..... | 109 |
| Figure 7.9: Sensitivity of the Cost Per Function Metric to the Reliability Ratio..... | 110 |
| Figure 7.10: Cost Per Image Elasticity to (clockwise from top left corner) Payload Costs, Spacecraft Bus..... | 112 |
| Figure 7.11: Elasticity of the Cost Per Image to the Learning Curve Slope..... | 112 |
| Figure 7.12: Cost Per Image Elasticity to Component Reliability..... | 113 |
| Figure 7.13: Cost Per Image Elasticity to the Imaging Rate..... | 113 |
| Figure 7.14: Cost Per Image Elasticity to Mission Design Life..... | 114 |
| Figure 7.15: Sensitivity of the Cost Per Image Metric to the Mission Design Life..... | 115 |

List of Tables

| | |
|---|-----|
| Table 1.1: Proposed Separated Spacecraft Interferometer Missions..... | 17 |
| Table 3.1: The GINA "Quality of Service" Parameters Applied to an SSI..... | 40 |
| Table 3.2: SSI System Architecture Metrics..... | 41 |
| Table 3.3: Matrix of the GINA Capability Parameters vs. SSI Architecture Design Variables... | 43 |
| Table 3.4: Matrix of the GINA Capability Parameters vs. SSI Assumptions & Requirements... | 44 |
| Table 4.1: Estimated SSI Optical Imaging Task Times..... | 55 |
| Table 5.1: Aggregated Functioning States for the MAMSC Model..... | 83 |
| Table 6.1: Selected SSCM Cost Estimating Relationships - Version 7.4 [Bearden, 1996]..... | 91 |
| Table 6.2: Selected SSCM Cost Estimating Relationships - Version 8.0 [Bearden, 1996]..... | 91 |
| Table 6.3: Learning Curve Slopes as a Function of Production Quantity in the Aerospace Industry..... | 92 |
| Table 6.4: Delta II Performance Characteristics to L2 [Boeing, 1997]..... | 94 |
| Table 7.1: Architecture Parameters Held Constant Across All Architectures..... | 100 |
| Table 7.2: Best Cost Per Function Architecture for Different Budgets..... | 106 |
| Table 8.1: Optimal System Design Architectures..... | 117 |

Chapter 1

Introduction

*“Everywhere I look I see the potential for growth, for discovery
far greater than anything we have seen in the 20th century.”*

- David Packard

VISION – to see the unknown. This is the desire of both space scientists and military/intelligence commanders alike. Interferometry, a technique that uses multiple apertures to achieve image resolutions unobtainable by any reasonably sized single aperture instrument, holds the potential to provide this vision as never before.

This research provides a detailed systems analysis of a separated spacecraft interferometer (SSI) mission. The specific interest is to apply a formal Systems Engineering and Architecting (SE&A) methodology to find a design architecture(s) that maximizes the value of every dollar spent on the mission over its lifetime, where value is measured by the number of images the system produces. A maximum return on investment is sought because funding approval of expensive space missions is difficult in today’s fiscal environment.

First, a set of unified metrics for comparing different design architectures are adopted from Distributed Satellite Systems (DSS) theory [Shaw, 1998]. Next, three quantitative models – a capability, reliability, and cost model – are developed and coupled to evaluate the DSS metrics for any SSI architecture. Additionally, the sensitivity of these metrics to different architecture assumptions and requirements is calculated. On the basis of the DSS cost per function metric, the best design(s) for a future SSI mission are identified.

The next section of this chapter discusses the rationale for placing an interferometer in space and reviews current proposed designs. Sections 1.1.1 and 1.1.2 outline the potential application of interferometry to civilian and military missions. Section 1.2 provides more detail on the research motivation and objectives, placing this work within the context of other recent system studies in the field of space-based interferometry. Finally, Section 1.3 outlines the remainder of this thesis.

1.1 Background

In optical interferometry, light is reflected by at least two separate collector mirrors into the optics of a combiner in which the light is interfered in real time. On the detector, fringes appear in the interference pattern. From the amplitude and phase information of the fringes for a number of different separations and orientations of the collector mirrors, a cross-correlation map is formed in the u - v plane, where u and v are free variables in the image's Fourier transform domain. By taking the inverse Fourier transform, a brightness map (image) of the observed object is formed in x - y space. NASA has identified space-based interferometry as a key technology for future space science programs, such as the Origins program [Beichman, 1996], due to the ability of an interferometer to deliver an angular resolution orders of magnitude greater than that possible by single aperture telescopes. For this same reason, interferometry could play a key role in the National Reconnaissance Office's (NRO) Future Imagery Architecture.

Interferometry with radio waves is a common practice in radio astronomy, while interferometry for imaging in the visible spectrum is more difficult and has been demonstrated only with ground-based telescopes [Su, 1998]. Placing such an instrument in space, however, provides many advantages over ground-based systems. First, the sensitivity of the interferometer increases due to the removal of the Earth's partially opaque, turbulent atmosphere. Second, diffraction limited observations become possible over wider fields of view [Shao et al, 1992]. Third, the imaging of faint objects next to bright ones, as would be required for the direct detection of extra-solar planets, becomes easier. Finally, if placed in the proper orbit, the system could be used for the surveillance of the Earth.

A space-based interferometer, by combining light from widely separated collector mirrors, has the capability to provide the angular resolution of a filled aperture telescope whose diameter is equal to the baseline, or separation distance, between the collectors. While the size of a ground-based telescope is limited by the force of gravity and the size of a single aperture space telescope is limited by the diameter of current rocket shrouds and the capabilities of deployment mechanisms, the size of a separated spacecraft interferometer is only limited by the line of sight between spacecraft and the diffraction effects of the relay optics.

Original concepts for space-based interferometers involved a single large satellite measuring tens to hundreds of meters in size [Kaplan, 1996]. The sole driver of this large size

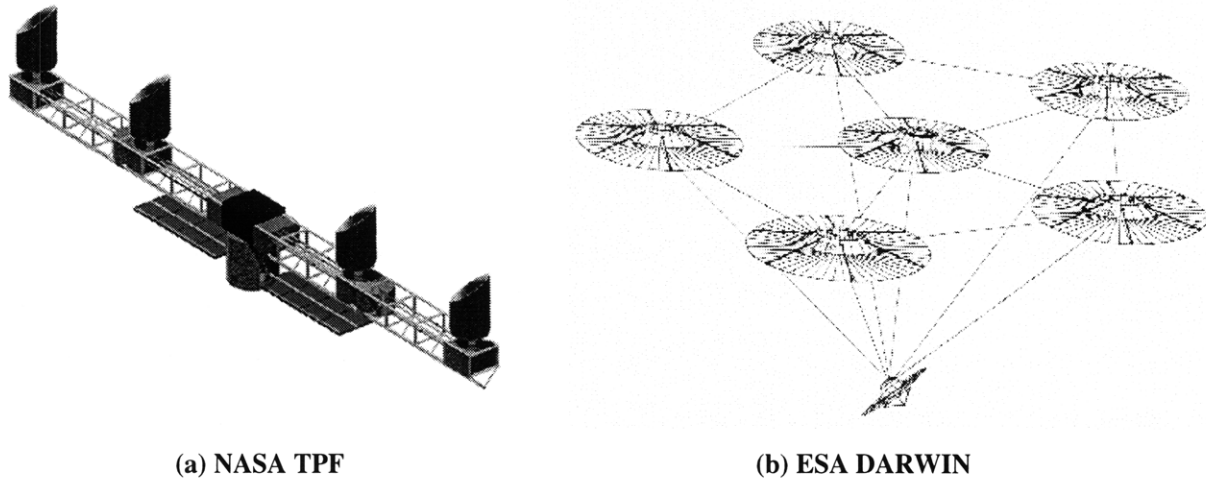


Figure 1.1: Two Proposed Space-Based Single Satellite (a) [JPL, 1998] and Multiple Satellite (b) [ESA, 1998] Interferometer Designs

was to provide a long baseline between the optics. More recently, NASA is considering distributing the key elements of an optical interferometer, namely the collector and combiner optics, on a minimum of three separate, smaller spacecraft [Colavita et al, 1996]. One satellite contains the combiner optics, while the other two satellites contain the collector optics. This configuration allows for longer baselines, up to kilometers in length, than possible with a single satellite. Figure 1.1 illustrates two early structurally connected and separated spacecraft interferometer designs, while Table 1.1 lists the SSI's currently being designed along with the characteristics of each system.

The National Aeronautics and Space Administration (NASA) has developed several SSI

Table 1.1: Proposed Separated Spacecraft Interferometer Missions

| Mission | # Spacecraft | Spectrum of Observation | Orbit | Maximum Baseline(km) | Target Launch Date |
|--------------------------|---------------------|--------------------------------|-----------------------------|-----------------------------|---------------------------|
| DS3 (NASA JPL) | 3 | Visible | Heliocentric (1AU) | 1 | 2001 |
| Free-Flyer (ESA) | 7 | Visible | Lagrange (L2) | 2.5 | Indefinite |
| Darwin/IRSI (ESA) | 6 | IR | Heliocentric (≥ 4 AU) | 5 | 2009 |
| TPF (NASA) | 5 | IR | Heliocentric (5.2 AU) | 0.075 | 2010 |
| Music (NASA JPL) | 18 | Visible | Lagrange (L2) | 100 | Indefinite |

designs. The first mission, named Deep Space 3, is intended to serve as a technology demonstration mission to validate the high-risk technologies; such as formation flying, combiner optics, and high resolution metrology; that will be required for future, more complex SSI missions. Another mission, the Terrestrial Planet Finder (TPF), has been proposed for the Origins program as either a structurally connected or separated spacecraft interferometer that seeks to directly detect extra-solar planets in the infra-red spectrum. The European Space Agency (ESA) has proposed a similar mission, named Darwin, to serve as one of ESA's four cornerstone space science missions in the first decade of the next century. As technology progresses, one may envision future arrays of a dozen or more small satellites working synergistically to image extra-solar Earth-like planets or to obtain high resolution images of the Earth.

1.1.1 Civilian Applications – Astronomy

Civilian space-based interferometry in the visible spectrum has three potential applications: astrometry, imaging, and spectroscopy. Astrometry involves making precise measurements of the positions of celestial objects. Imaging, on the other hand, involves producing high resolution intensity maps of celestial objects or the Earth itself. Finally, spectroscopy is the process of determining the chemical composition of a celestial body from the study of its spectral signature.

The NASA Origins Program seeks to learn about the formation of planetary systems within the galaxy, with the ultimate goal of directly imaging planets orbiting about other stars [Kaplan, 1996]. This cannot be accomplished with today's technology due to the limited resolution of single aperture telescopes. Thus, a new system is needed to enable high resolution studies of the night sky. This system is an optical interferometer.

Angular resolution improves proportionally with the diameter of filled aperture telescopes and with the maximum baseline between apertures of an interferometer. Figure 1.2 compares the angular resolution possible with different space-based observatories. A higher angular resolution is delineated as a smaller angle on the milliarcsec scale. As one can see, an interferometer provides the capability of producing images with orders of magnitude improvement in angular resolution in comparison with other methods. Such an improvement will enable the following NASA goals for the 21st century [Lau et al, 1996]:

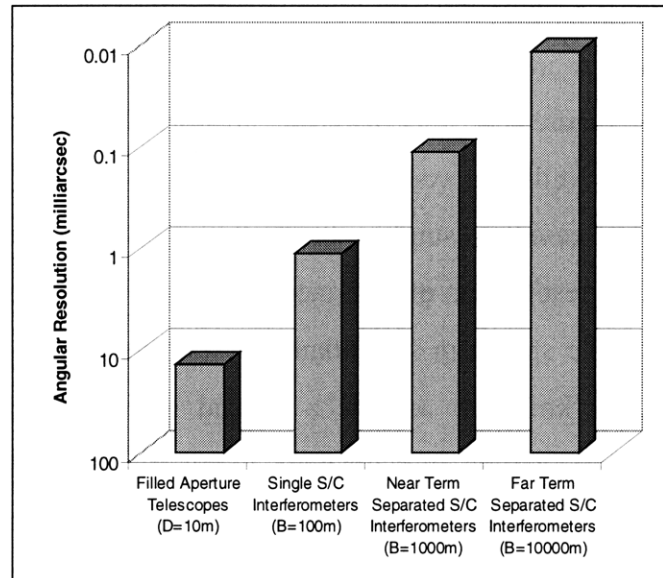


Figure 1.2: Resolutions Enabled by Different Space-Based Observatories (D= Aperture Diameter, B=Baseline, $\lambda=550$ nm)

- 1) Submilliarcsec measurement of stellar diameters.
- 2) Resolution of close and interacting binary systems.
- 3) Direct detection of extra-solar planets.
- 4) Precise measurement of galactic and cosmic distance scales.

Figure 1.3 illustrates the concept for the precursor SSI mission, known as Deep Space 3.

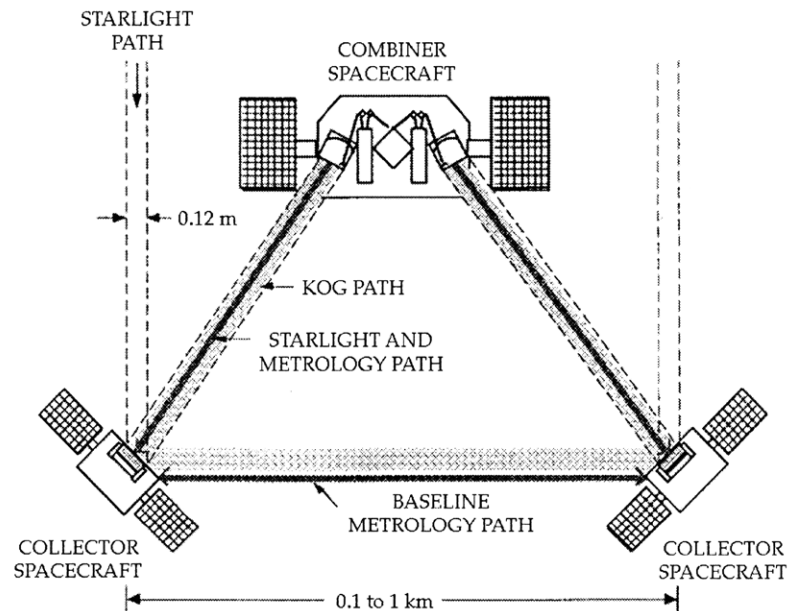


Figure 1.3: Deep Space 3 Mission Concept [Colavita et al, 1996]

1.1.2 Military Applications - Surveillance

In the military space arena, optical interferometers promise to increase the country's surveillance capability. Figure 1.4 illustrates the imaging resolution capabilities of a nadir looking visible spectrum surveillance system as a function of the altitude of the satellite(s) and the aperture diameter in the case of a single aperture telescope or the baseline in the case of an SSI. As one can see, high resolutions of five meters or less require large apertures. Take the specific example of a visible spectrum surveillance system in a geosynchronous (GEO) orbit with an altitude of 35,786 km. To achieve a ground resolution of a half meter requires diffraction limited optics 48 meters in diameter. Likewise, obtaining images with 10 cm resolution requires a 240 m aperture! Needless to say, single aperture telescopes of this size are impractical. Even if they could be manufactured, the apertures would not fit in any launch vehicle's payload shroud. The Titan IV rocket, with the largest shroud in the U.S. launch vehicle fleet, can only launch payloads up to approximately five meter in diameter [Isakowitz, 1995]. Even a segmented mirror that would be deployed once in orbit is unlikely to achieve the desired results. However, by employing multiple satellites formation flying as an SSI to achieve the required large synthetic aperture of 50 m or more, modest sized optics may be used.

While inherently complex due to near field observing effects and stringent pathlength requirements, designs of Earth observing optical interferometers have been proposed. Most of these designs have focused on placing the interferometric array in a geosynchronous orbit [Kong, 1998]. Geosynchronous orbits, which are orbits at an altitude of 35,786 km in which the orbital

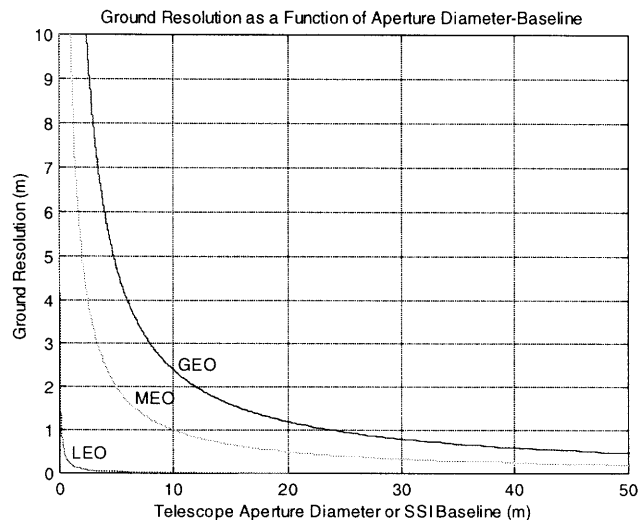


Figure 1.4: Ground Resolution of a Nadir Looking Single Aperture Telescope or Separated Spacecraft Interferometer From Different Earth Orbits

period of the satellite is equal to the period of rotation of the Earth, provide several advantages for an interferometer observing the Earth. First, at a geosynchronous altitude each satellite in the array has an overlapping field of view and remains over the target area of interest during the entire course of a twenty-four hour day. This allows continuous monitoring of areas of concern with the same high resolution as current low Earth orbit (LEO) surveillance satellites, which are in view of the target area only for a period of minutes during particular orbital passes. In other words, a geosynchronous SSI provides the adversary no windows of opportunity to maneuver during the intermittent times when no LEO surveillance satellites are overhead. This current weakness of military surveillance has been exploited several times in recent history [CNN, 1998]. Second, at a geosynchronous altitude the satellites always have line-of-sight contact, and the baseline vectors between satellites vary naturally in a periodic manner every twenty-four hours. Finally, at this high altitude the gravity gradient and resulting differential acceleration on each satellite is very low, minimizing the amount of fuel required for corrective maneuvers. Such SSI's surveying the Earth, with baselines ranging from tens to hundreds of meters, possess the capability to provide visible images with orders of magnitude better resolution than any Earth observing telescopes today.

1.2 Motivation and Objectives

Several system level studies have recently been completed in the field of separated spacecraft interferometry. One such study aimed to find the cross-over baseline for when it makes sense to transition a space-based visible spectrum interferometer from a single spacecraft to multiple spacecraft on the basis of a launch mass metric. Depending upon the operational mode of the interferometer, this cross-over baseline was found to range from 400 m to 650 m [Surka et al, 1996]. Another study performed a similar analysis for the 75 m baseline Terrestrial Planet Finder mission in the infrared spectrum, and found the SSI to be slightly more mass efficient than a single spacecraft interferometer both in a 1 AU orbit and a 5.2 AU orbit [Stephenson et al, 1998]. This study also found the ability of the SSI architecture to vary baselines for synthetic imaging purposes very attractive. Another study found the optimal imaging trajectories for an SSI operating outside a gravity-well and viable orbits for an SSI operating within the Earth's gravity-well [Kong, 1998]. While the first two of these studies determine *whether* an SSI should be used and the latter study optimizes the *operation* of an SSI

during an imaging sequence, the research presented here focuses on how to *design* an SSI architecture to provide maximum performance at minimum cost over the lifetime of the mission.

The current design of SSI's is analogous to that of conventional ground-based interferometers. This conventional design entails multiple collectors spaced equally apart from a single combiner, with every spacecraft bus carrying only a single collector or combiner as its payload. At first, this appears to be a logical course of action as such a design is successful for ground-based observatories. However, there are important distinctions between ground-based and space-based interferometers. On the ground, whenever a component fails and renders the system inoperable, a technician simply repairs the interferometer by replacing the faulty component. In space, one does not have this luxury. A failure of a single component in one of the spacecraft in a multiple-spacecraft array can yield the entire system useless, even if the remaining spacecraft in the array are working perfectly. Thus, a space-based interferometer must be designed to be extremely reliable and robust to partial failures.

It is well known that the best way to improve the reliability of a system is through redundancy - both within a spacecraft and between spacecraft. However, the amount of redundancy required for a series of interdependent spacecraft in a conventional design to be robust to partial failures simply costs too much. The increased redundancy in a space-based interferometer is implemented in one of two ways: 1) insert redundant components that are nominally operable (operational redundancy) or serve in a standby mode (backup redundancy) in the subsystems of each collector, combiner, and bus (mass penalty) or 2) use components with a higher mean-time-to-failure (mttf) in the collector, combiner, and bus (development cost penalty). Both methods increase reliability by improving redundancy or reliability within each spacecraft.

To minimize these additional costs and make future SSI's affordable so that they will be embraced by the astronomy and surveillance communities, the *system architecture* must be designed such that it inherently provides high performance along with high reliability. System architecture variables that affect the reliability, performance, and cost of an SSI include the degree of multifunctionality in each spacecraft and the total number of spacecraft in the array.

This leads to the goal of this thesis - *To explore and "optimize" via Distributed Satellite System (DSS) principles the trade space involved in the design of future visible spectrum astronomical separated spacecraft interferometers.* The hope is that by viewing a space-based

interferometer as an interdependent *network*, rather than in the conventional context of a ground-based system, significant improvements in reliability, performance, and cost over current SSI designs can be achieved.

The key architectural variables being traded are the type of spacecraft used in the array and the level of distribution (number of spacecraft, number of payloads) within the system. The two types of spacecraft that may be placed within the array are single function design (SFD) spacecraft and modular and multifunctional spacecraft (MAMSC). SFD spacecraft are spacecraft in the interferometer that serve as *only* a collector or *only* a combiner. SFD satellites are cheaper, simpler, and smaller, but provide less inherent performance and redundancy in the SSI. MAMSC can function as *both* a collector and a combiner. MAMSC are more expensive, more complex, and heavier than SFD satellites, but provide greater performance and redundancy for a SSI. A system architecture optimized with respect to capability, performance, adaptability, and cost per function may contain a combination of these two types of spacecraft.

The number of satellites chosen determines the level of distribution within the SSI. The term “Distributed Satellite System” refers to a system of more than one satellite designed to operate in a coordinated fashion to perform some specific function [Shaw et al, 1998]. This definition encompasses a wide range of possible applications in commercial, civilian, and military sectors. The advantages offered by such systems can mean improvements in performance, cost, and survivability compared to traditional single-satellite deployments. However, the operations complexity and thus the operations cost of the system may also increase as the number of satellites in the interferometer increases. For an SSI, distribution is a necessity. However, there probably exists a number of spacecraft beyond which the marginal improvement in terms of system performance and reliability of adding more spacecraft to the array is no longer worth the marginal cost of building, deploying, operating, and maintaining these additional spacecraft.

Therefore a methodology for analyzing Distributed Satellite Systems will be demonstrated and documented for future use. This methodology is named GINA – Generalized Information Network Analysis [Shaw, 1998]. While tailored to the interferometry mission in this thesis, the methodology and its analytical tools can be applied to any space mission with multiple satellites.

Specific objectives of this work include:

1. To develop capability, reliability, and cost models that quantify the SSI system cost per function for a variety of architectures.
2. To optimize the SSI system architecture with respect to the cost per function metric.
3. To evaluate quantitatively the advantages and disadvantages of incorporating modular and multifunctional spacecraft into SSI arrays.
4. To identify how the performance of SSI arrays evolves with respect to each metric as a function of the number of spacecraft in the array.
5. To determine the sensitivity of the cost per function metric to different design assumptions and requirements.
6. To develop design rules of thumb for optical separated spacecraft interferometers.
7. To document the Distributed Satellite System (DSS) Generalized Information Network Analysis (GINA) methodology on a real space system for reuse in the future.

Specific areas that are *not* goals of this work include:

1. Providing a detailed Phase A design for an SSI – this thesis stresses architectural *system* issues as a function of the number of spacecraft.
2. Providing detailed satellite subsystem designs.
3. Deciding whether or not an SSI *should* be deployed for astronomy or surveillance.
4. Determining the best viewing geometry (Cornwell, Golay, etc.) or maneuvering profile (minimum time, minimum fuel, etc.) for an SSI.

1.3 Outline

Chapter 2 presents an overview of the fundamental physics behind optical interferometry to a level necessary to guide the system analysis. An understanding of this physics is needed to build an accurate capability model of the system. Chapter 3 outlines the DSS GINA systems engineering and architecting process, and applies this process to the SSI mission. Chapter 4 addresses the SSI capability model, while Chapters 5 and 6 develop the SSI reliability and cost models. Chapter 7 presents results for the optimized SSI architectures as a function of the number of satellites in the array on the basis of the reliability, performance, and cost model outputs as well as the cost per function metric. Finally, Chapter 8 concludes with some observations and rules of thumb for designing separated spacecraft interferometers based on the preceding analysis.

Chapter 2

Interferometry Fundamentals

“Less is more.”

- Ludwig Mies van der Rohe

2.1 What is Interferometry?

The *interferometry principle* states that for an optical or radio telescope, one does not need to use a filled aperture of diameter D to obtain the angular resolution corresponding to that aperture diameter. Rather, one may use multiple smaller apertures separated by the same distance as the single aperture diameter [Wohlleben, 1991]. A group of collector mirrors on separate spacecraft forms a synthetic aperture. The resolution of this synthetic aperture is equivalent to the resolution of a hypothetical single aperture telescope whose diameter is comparable to the maximum separation distance between the collector mirrors in the synthetic aperture.

An interferometer is an instrument in which electromagnetic (EM) radiation from a single source travels along two separate, equal-length paths and is then combined either physically (optical) or electronically (radio). When the EM waves combine, alternating bright and dark fringes are observed as differential pathlength is introduced, corresponding to areas of constructive and destructive interference, respectively. By measuring the amplitude and phase of these fringes at different baselines, information about the source in the Fourier plane is gained as the correlation matrix is filled. By taking the inverse Fourier transform of this information, an image of the source in the x-y plane may be retrieved.

Angular resolution, the ability to resolve fine detail, improves proportionally with the diameter of the aperture for a single aperture telescope and with the maximum separation baseline between the collectors of an interferometer. The achievable diffraction limited resolution (θ_r) of a filled aperture telescope is

$$\theta_r = 1.22 \frac{\lambda}{D} \quad (2.1)$$

where λ is the central wavelength of observation and D is the diameter of the filled aperture telescope [Larson et al, 1992]. The resolution of an interferometer is

$$\theta_r = \frac{\lambda}{B} \quad (2.2)$$

where B is the maximum baseline between a pair of collector mirrors as viewed from the source.

Figure 2.1 plots the angular resolution of the Hubble Space Telescope (HST) and several proposed space-based optical interferometers as a function of baseline. The solid line denotes the angular resolution of an optical interferometer according to Equation 2.2 for $\lambda=550$ nm. Hubble falls slightly above this line because it is a filled aperture telescope, and the Terrestrial Planet Finder (TPF) falls well above the line because this interferometer functions in the thermal infra-red spectrum ($\lambda=12$ μm). Notice where the Hubble Space Telescope and DS3, a proposed three-spacecraft SSI mission, fall on this plot. Even though DS3 contains smaller optics and is an order of magnitude cheaper than the Hubble Space Telescope, the images it can produce have up to two orders of magnitude greater angular resolution than those possible with Hubble. Herein lies the advantage of interferometers – they provide a means for obtaining superior angular resolution for optical imaging.

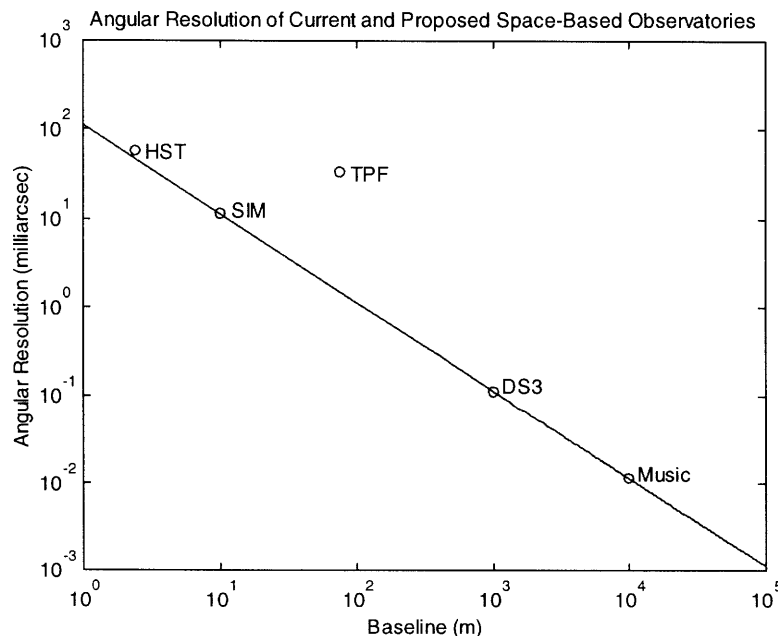


Figure 2.1: Angular Resolution of the Hubble Space Telescope vs. Proposed Space-Based Interferometers

It is important to note that a synthetic aperture only provides the equivalent angular resolution, *not* signal strength, of a comparable sized single aperture. Sensitivity is dependent on the size of the individual apertures in the synthetic aperture array. The total sensitivity of the system is a function of the total collecting area within the array.

The interference pattern produced by the recombination of the EM radiation is a visibility map of the source object. A true image of this source may then be recovered by taking the inverse Fourier transform of the measured visibility map. Each data point or spatial frequency in Fourier (u-v) space corresponds to a unique vector baseline between a pair of collectors

$$u_{ij} = \frac{\pm |x_i - x_j|}{\lambda} \quad (2.3)$$

$$v_{ij} = \frac{\pm |y_i - y_j|}{\lambda} \quad (2.4)$$

where u and v are the spatial frequencies in the Fourier plane, x and y are the coordinates of satellites i and j as projected onto the x-y plane which lies normal to the line of sight, and λ is the wavelength of observation. Each vector baseline is defined by both the angular orientation between the collectors and the magnitude of the separation distance between the collectors. To sample a subset of the spatial frequencies in the Fourier plane requires that the collector spacecraft continuously reorient such that fringe measurements are collected over many different vector baselines. Finally, it is important to note that only partial coverage of the spatial frequencies in the Fourier plane, not complete coverage, is required to obtain valuable information about the true image via the inverse Fourier transform as several techniques currently exist for "cleaning" the image.

Unlike radio signals, optical signals must be interfered in real time, increasing the complexity of the system. This also introduces the additional design and operational constraint on optical interferometers that the EM radiation must travel along both paths an identical total length to the combiner to within a fraction of the wavelength of observation. While this has not yet been demonstrated in space, engineers predict that visible light imaging via space-based interferometry will become technologically feasible in the next few years [Doody, 1997]. The space science community is already preparing for this advent with the design of several different SSI's. Before discussing the details of SSI system architectures, however, let us review the

fundamental physics behind optical interferometry. This physics plays a key role in determining the design requirements and constraints for the SSI architectures.

2.2 The Physics of Optical Interferometry

Interference occurs when light from the same source travels along two separate, equal length paths and then recombines. For monochromatic light, the intensity (I) of the observed fringes in the interference pattern is

$$I = I_1 + I_2 + 2\sqrt{I_1 I_2} \cos \Delta\phi \quad (2.5)$$

where I_1 and I_2 are the intensity of light beams one and two, and $\Delta\phi$ is the phase difference between the two light beams. In equations 2.6 and 2.7 it can be seen that the maximum and minimum intensities occur when the phase difference is $2m\pi$ and $(2m+1)\pi$, respectively, where m is an integer. The maximum and minimum observed intensities are

$$I_{\max} = I_1 + I_2 + 2\sqrt{I_1 I_2} \quad (2.6)$$

$$I_{\min} = I_1 + I_2 - 2\sqrt{I_1 I_2} \quad (2.7)$$

The science information is found by measuring the amplitude and phase of the observed fringes. The greater the contrast of this fringe pattern, the easier it is to measure this information. The visibility function (V) is a measure of the contrast of the observed fringes, and is defined as

$$V = \frac{(I_{\max} - I_{\min})}{(I_{\max} + I_{\min})} \quad (2.8)$$

While a visibility of one is ideal, a visibility of 0.7 is the current design target for astronomical optical interferometers [Miller et al, 1995].

Several conditions are required for the successful interference of light to take place. First, the light traveling each path of the interferometer must originate from the same source and have the same frequency and intensity. Otherwise, the signals will be incoherent, resulting in poor visibility. Second, the light beams must travel identical pathlengths to ensure that the same wavefronts are interfered. Unequal pathlengths will lead to a large phase difference between the

signals, which in turn degrades the visibility of the fringes. The optical path difference (Δp) at which interference fringes disappear is defined as the coherence length, and is a function of the speed of light (c) and the spectral bandwidth ($\Delta\nu$) of the radiation being observed [Hariharan, 1992].

$$\Delta p = \frac{c}{\Delta\nu} = \frac{\lambda}{2\pi} \Delta\phi \tag{2.9}$$

One way to help accommodate this constraint is to introduce an optical delay line in the path of the light through the interferometer. Figure 2.2 illustrates the geometry of a two collector optical interferometer with an optical delay line. Light from the source is redirected into the optics of a combiner in which the light is interfered. The amplitude and phase of the interference fringes are then measured by the fringe detector. If the incoming wavefront is not orthogonal to the line-of-sight of the interferometer, then an additional optical pathlength Δp is introduced into the path of the light reflected off Collector 1.

$$\Delta p = d \sin \theta \tag{2.10}$$

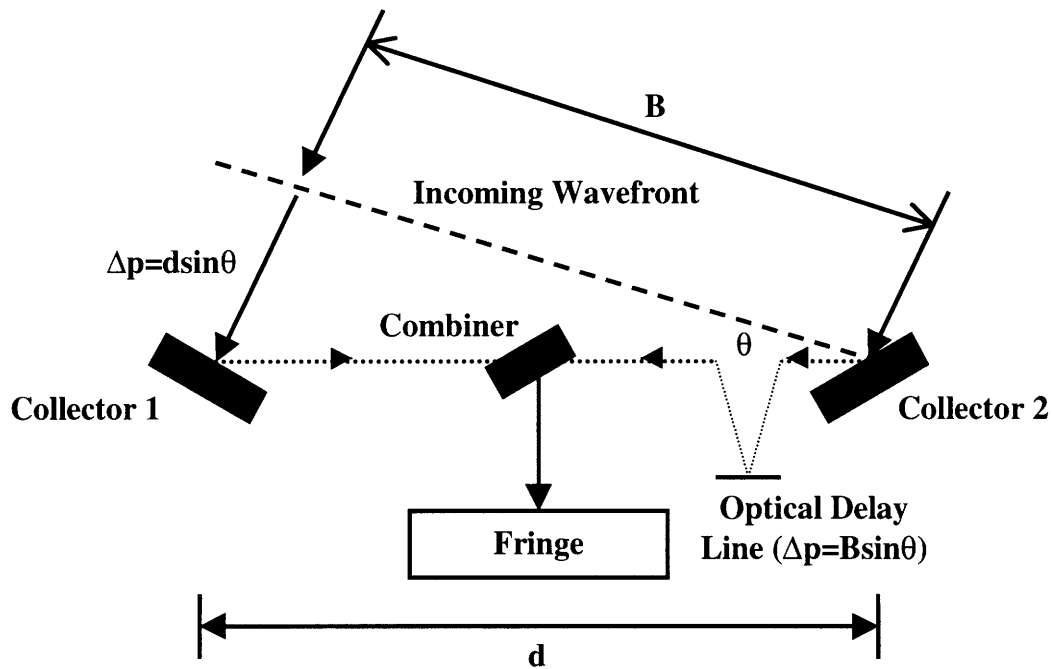


Figure 2.2: Geometry Between Two Collectors in an Optical Interferometer

To maintain coherence, an optical delay line is introduced into the path of the light reflected off Collector 2. The length of travel through the optical delay line is equivalent to the magnitude of the optical path difference induced by the angle θ between the incoming wavefront and the separation between collector mirrors.

Finally, the two light beams being interfered must have the same polarization. Polarization is defined as the orientation between the electric field in the EM wave and its direction of motion. If two beams are polarized in orthogonal planes or are circularly polarized in opposite senses, then no interference pattern will result. If the planes of polarization are slightly offset at an angle α , then the visibility of the fringes will become

$$V_{\theta} = V_0 \cos \alpha \quad (2.11)$$

where V_0 is the maximum possible visibility of the interference fringes, which occurs when the two light beams have identical states of polarization and α equals zero.

Assuming these three conditions are met, the interference pattern produced on the detector is the amplitude of one harmonic of the spatial Fourier transform of the true image [Nisbet, 1992], where the Fourier transform is defined as

$$F[g(x)] = \int_{-\infty}^{\infty} g(x) e^{-[i2\pi(\xi x)]} dx = G(\xi) \quad (2.12)$$

The true image may be recovered by taking the inverse Fourier transform.

$$F^{-1}[G(\xi)] = \int_{-\infty}^{\infty} G(\xi) e^{-[i2\pi(\xi x)]} d\xi = g(x) \quad (2.13)$$

It should be noted that this only holds true when the source being observed satisfies the far field condition of the interferometer

$$R \gg \frac{B^2}{\lambda} \quad (2.14)$$

where R is the distance from the source to the interferometer, B is the baseline between the apertures of the interferometer, and λ is the wavelength of observation [Thompson et al, 1986]. For the remainder of this thesis it is assumed that the arrays are steered such that θ is always small. In this case $d \cong B$.

With knowledge of the fundamental physics, definitions, and formulas behind optical interferometry, the details involved in producing images with an SSI may now be addressed.

2.3 Synthetic Imaging

Synthetic imaging, also known as aperture synthesis mapping, is the process of proceeding from the measured complex visibility function to the brightness distribution, or image, of the source. To obtain such an image, this visibility function, also known as the spatial coherence function, must be sampled over many discrete vector baselines. Each vector baseline between apertures in an interferometer is converted into Fourier space via the transformations in Equations 2.3 and 2.4.

By sampling the u-v plane over many baselines, the brightness distribution (image) of the object being observed may now be mapped. Let $J(x,y)$ represent the true brightness distribution of the source mapped onto a two-dimensional plane with coordinates x and y (i.e., the true image) and $V(u,v)$ denote the measured visibility function. These two functions form a two-dimensional Fourier transform pair

$$J(x, y) \stackrel{FT}{=} V(u, v) \quad (2.15)$$

where FT denotes the Fourier transform. The Fourier transform is carried out through the following double integral:

$$J(x, y) = \int_{-\infty}^{+\infty} \int_{-\infty}^{+\infty} V(u, v) e^{(2\pi j(ux+vy))} dudv \quad (2.16)$$

This is an idealized explanation of the synthetic mapping process as the reconstruction of an image via the above Fourier transform only works if $V(u,v)$ is uniformly sampled across a regularly spaced grid. In reality, however, $V(u,v)$ is sampled at irregularly spaced points. In order to reconstruct the image, a uniformly sampled grid is created by interpolating between the measured values of $V(u,v)$ and the points on the grid.

This process is carried out in the following manner. Let $S(u,v)$ denote a sampling function which is non-zero only for values (u,v) where the visibility $V(u,v)$ has been directly measured by the interferometer.

$$S = \begin{cases} 1 & \text{if } V(u,v) \text{ exists} \\ 0 & \text{otherwise} \end{cases} \quad (2.17)$$

Taking the inverse Fourier transform of the non-uniformly sampled visibility function yields a “dirty” map or “dirty” image $J^D(x,y)$ [Rohlfs et al, 1996].

$$J^D(x,y) = \sum_k S(u_k, v_k) V(u_k, v_k) e^{-i2\pi(u_k x + v_k y)} \quad (2.18)$$

If one assumes that a point source is located at the center of the dirty map, then the visibility $V(u,v)$ is unity at the center of the Fourier plane. The brightness map (image) of such a point source is the point spread function (*PSF*) or the “synthesized beam” of the array and is the Fourier transform of the sampling function:

$$PSF(x,y) \stackrel{FT}{=} S(u,v) \quad (2.19)$$

$$PSF(x,y) = \sum_k S(u_k, v_k) e^{-i2\pi(u_k x + v_k y)} \quad (2.20)$$

Figure 2.3 illustrates the point spread function for an irregularly sampled $V(u,v)$. The main beam is the central point source, while the smaller surrounding beams, known as sidelobes, are artificial structures that result from holes in the u - v coverage (*i.e.*, the irregular spacing of the sampled points in the u - v plane – there exist unsampled points within u_{\max} and v_{\max}). Thus, the point spread function may be thought of as a metric for evaluating the quality of a particular u - v coverage for an interferometric array. Poor u - v coverage results in a short and wide central beam and tall sidelobes, while optimal u - v coverage results in a point spread function with a tall and thin central beam and short sidelobes.

As has been illustrated, the visibility function $V(u,v)$ is the Fourier transform of the true image $J(x,y)$, and the point spread function $PSF(x,y)$ is the Fourier transform of the sampling function $S(u,v)$. Therefore according to the convolution theorem [Bracewell, 1978], the “dirty”

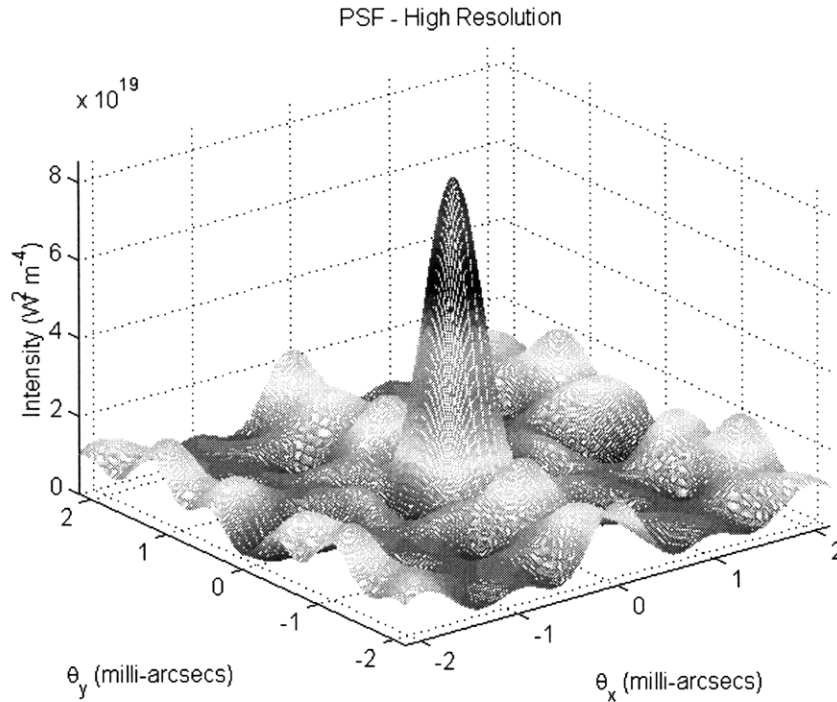


Figure 2.3: Point Spread Function for an Irregularly Sampled u-v Plane

image is the convolution of the point spread function with the true image.

$$J^D(x, y) = PSF(x, y) \otimes J(x, y) \quad (2.21)$$

where \otimes denotes the convolution. Thus, the true image may be obtained through a deconvolution.

It should be noted that the fast Fourier transform (FFT) is often used over the Fourier transform to improve computational speed. Finally, additional algorithms to improve the quality of the final image are often applied. Two such algorithms are the CLEAN algorithm [Schwarz, 1979] and the MEM (maximum entropy method) algorithm [Narayan et al, 1986].

2.4 Summary

In this Chapter, we have defined the interferometry principle, explained the basic physics of interferometry, and reviewed the synthetic imaging process. With this knowledge of the fundamentals behind interferometry, we may now proceed to the SSI system analysis.

Chapter 3

System Analysis Methodology

“The need for a well-integrated approach to system design and development can be better appreciated when it is realized that approximately 80%-90% of the development cost of a large system is predetermined by the time only 5%-10% of the development effort has been completed.”

- International Council on Systems Engineering (INCOSE)

Distributed Satellite Systems represent investments ranging from hundreds of millions to billions of dollars on the behalf of a national government or private commercial entity. With so much at stake, it is important to apply a formal systems engineering methodology, at the conceptual design stage, that captures the unique qualities of Distributed Satellite Systems to ensure that the final design provides the best value to the customer and creates a satisfactory return on investment. Such a Systems Engineering and Architecting (SE&A) methodology for the design and analysis of Distributed Satellite Systems, which is also compatible with the formal SE&A process, has recently been developed. This new methodology is named GINA – the Generalized Information Network Analysis methodology for Distributed Satellite Systems [Shaw, 1998].

This chapter provides a brief overview of the GINA methodology and then applies it to the SSI mission. First, the traditional SE&A process is reviewed, and GINA is introduced within the context of this process. Next, the customer requirements are defined, the capability requirements are derived, system metrics for evaluating alternate architectures are developed, and the functional analysis is introduced. Finally, methods for deriving top-level architectures, evaluating these architectures, and selecting the final architecture are discussed.

Figure 3.1 illustrates the SE&A process as defined by the International Council on Systems Engineering (INCOSE). The first step is always to define the customer requirements (1), answering the question “What mission must the system fulfill to satisfy the customer?” Next, the capability requirements of the system are defined (2). This step represents a translation

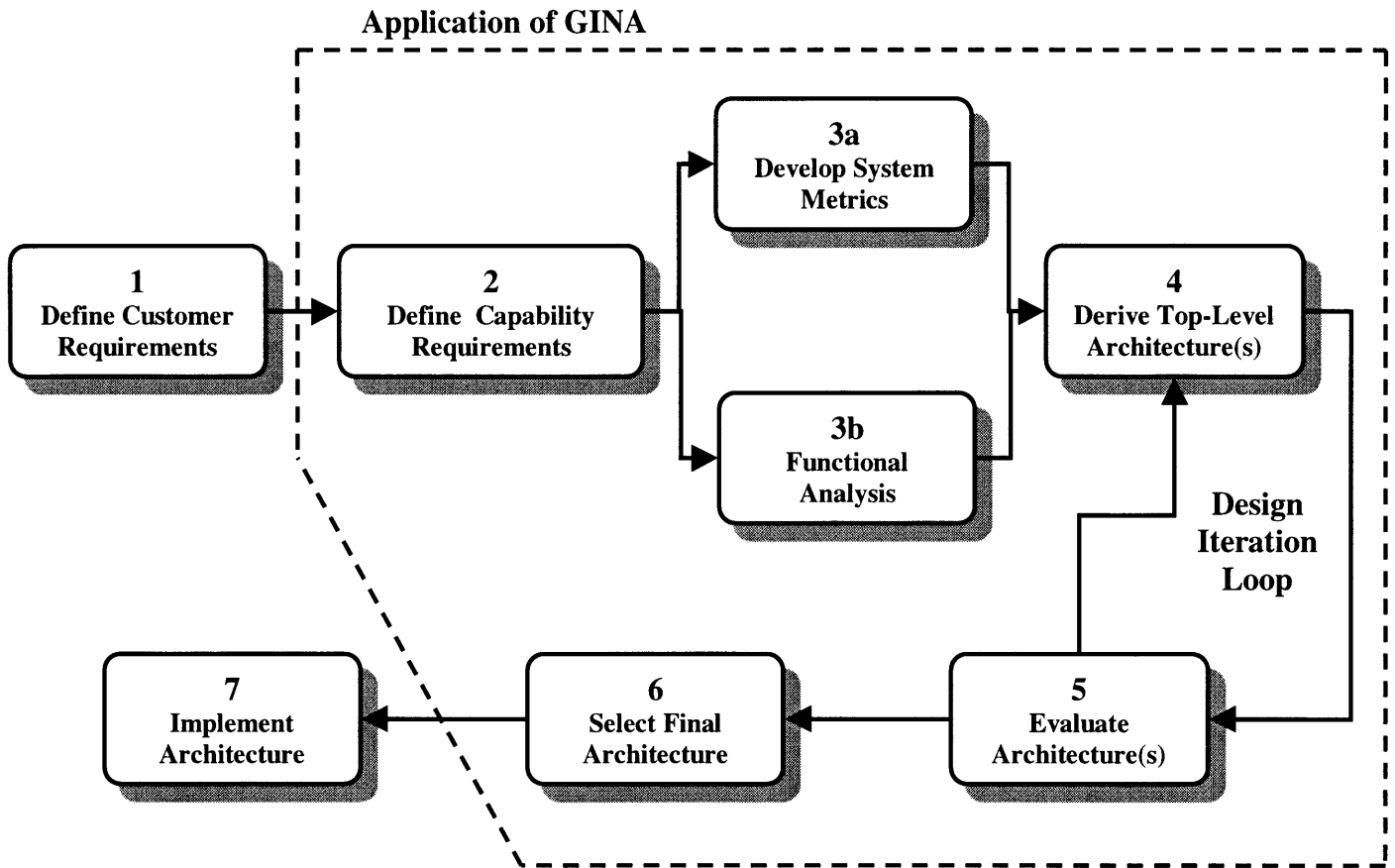


Figure 3.1: The Systems Engineering and Architecting Process

of quantitative requirements stated in the language of the customer into a set of capability requirements, stated in the language of the engineer, that the system must meet to satisfy the customer. These capability requirements define the level to which specific attributes of an architecture must perform in order for that architecture to be considered functional and therefore viable. After the capability requirements have been defined, the next two steps in the SE&A process may be carried out concurrently. Functional analysis (3b) is the process of describing all the tasks the system must do to accomplish its mission and satisfy all requirements, but not how to do these tasks. At the same time, the metrics (3a) by which each candidate architecture will be evaluated may also be derived from the capability requirements. Once these two concurrent steps have been completed, candidate architectures (4) that meet the capability requirements may be proposed and then evaluated (5) on the basis of the system metrics. Notice that this is an iterative process during which multiple architectures are developed and evaluated. Also note that this step requires a mathematical model of the system on which simulations may be run to

evaluate the system metrics of each architecture as a function of a set of architecture design variables. This is often not done, but is necessary to quantify differences between architectures. Once the systems engineer has evaluated a number of different architectures, a final architecture must be selected (6) on the basis of the metrics developed in step 3a, realizing that this one decision will have a profound effect on the rest of the program, both technically and fiscally. Once this decision has been made, the system may be decomposed, designed in detail, manufactured, integrated, tested, deployed, operated, and eventually disposed (7).

The dashed line in Figure 3.1 shows the sphere of influence over which the GINA methodology may be applied within the SE&A process. One of the shortcomings of the process shown in Figure 3.1 for SE&A is that no guidance is given as to how the metrics should be selected, how the functional analysis should be executed, the level to which analyses should penetrate the details of the architectures, etc. Given this ambiguity in the SE&A process, two teams designing an identical mission following the steps laid out in Figure 3.1 could yield two completely different system architectures. For example, if the metrics developed in step 3a only capture performance, the final system architecture might contain an inherently high level of risk and be prohibitively expensive. Conversely, metrics that focus exclusively on cost may lead to system architectures that do not meet all capability requirements. Likewise, if the models developed in step 3b do not sufficiently capture the pertinent physics, important trades may be overlooked which could lead to the selection of an inappropriate architecture and a subsequent costly redesign. The GINA methodology removes this ambiguity in the SE&A process by providing a framework for consistently capturing all of the pertinent system architecture design issues.

The foundation behind the GINA methodology is the belief that all satellite systems are information disseminators that can be represented as information transfer networks [Shaw, 1998]. A summary of the procedural steps in the GINA methodology within the context of Figure 3.1 follows. The remaining sections of this Chapter discuss these steps in more detail and apply them to the SSI mission.

1. Define Customer Requirements
 - Identify the customer.
 - Define the customer requirements.

2. Define Capability Requirements
 - Translate the customer requirements into the four Capability “Quality of Service” parameters: isolation, rate, integrity, and availability.
3. A) Develop System Metrics
 - Define the performance, cost per function, and adaptability metrics by which all proposed system architectures will be compared and evaluated.

B) Functional Analysis

 - Model the system as a network, defining all origin-destination (O-D) pairs.
 - Matrix the four Capability “Quality of Service” parameters against the design variables, assumptions, and requirements to identify the key design trades within the system.
4. Derive Top-Level Architecture(s)
 - Allocate values to the key design parameters identified in 3B.
5. Evaluate Architecture(s)
 - Perform a system abstraction by defining the simplest models that still quantitatively capture these tradable design parameters.
 - Using these models, calculate the capability, performance, cost per function, and adaptability of each architecture that meets or exceeds the specified capability “Quality of Service” parameters.
6. Select Final Architecture
 - Select the final architecture that provides the best overall system value in terms of the cost per function metric.

Through these steps, GINA allows the systems engineer to make meaningful, quantitative trades at the conceptual design level by directly relating lifecycle performance to lifecycle cost.

3.1 Define System Requirements

3.1.1 Identifying the Customer

For a Distributed Satellite System, the customer is the entity that derives utility from the system, such as troops determining their position from GPS or companies teleconferencing through a broadband satellite network. In the case of an SSI, there exist two separate customers. The first is the space science and astronomy community. This community will receive all of the images from the SSI for scientific study, and would ideally prefer a system that produces the greatest number of high quality images so that as many targets as possible can be studied over the lifetime of the system. Because such a system will most likely be financed by a single

federal government or through a combination of governments, the second customer is the taxpayer community. In contrast to the astronomers, this community would prefer the least expensive system that meets the capability parameters. The conflict between these two opposing communities will be captured shortly by the cost per function metric.

3.1.2 Define the Customer Requirements

Requirements come in two forms – customer and capability, both of which should be considered tradable. Customer requirements are a communication from the customer to the engineer about what the system must do and how well it must do it. Capability requirements are a translation of the customer requirements from quantitative characteristics in the language of the customer to quantitative requirements in the language of the engineer. The process of requirements definition in aerospace projects has taken on increased importance in the past decade as the first, most important step in the systems engineering process of complex systems. This has come with the realization that the cost of fixing a defect in a design is directly proportional to the stage within the systems engineering process where it is found [Boppe, 1998]. If the problem is identified early on in the requirements or design phases of the program, then it is relatively inexpensive to fix. But if the problem is not found until the later manufacturing and testing phases, then it becomes extremely expensive to fix. For this reason, both customer and capability requirements must be explicitly defined at the conceptual design stage to identify potential conflicts earlier rather than later.

Additionally, constraints may be applied to a design to eliminate those alternate system architectures that exceed available resources. Examples of constraints include limited funding, a tight schedule, and the laws of physics. In this study, the number of constraints are minimized in order to fully understand the trade space for separated spacecraft interferometers. It is important here to stress that this study investigates the architectural design of an SSI over a general class of missions. Constraints would come into play during the design of an SSI for a single, specific mission. The customer requirements for an SSI may now be introduced.

From the literature and personal communications with members of NASA, the following customer requirements were collected for the SSI mission:

1. Perform synthetic imaging in the visible spectrum ($\lambda= 0.4\text{-}0.7 \mu\text{m}$).
2. Achieve a very high angular ($F(B,\lambda)$) resolution ($\theta_r=113 \mu\text{arcsec}$).
3. Maximize the total number of images over the mission life (≥ 100).

4. Minimize total cost (design+manufacture+launch+operations) (< \$500 M).
5. Be capable of surveying a wide variety of desired targets.

3.2 Define Capability Requirements

In the GINA methodology, the capability of a DSS is characterized by four “Quality of Service” parameters that relate to the detection process and to the quantity, quality, and availability of the information that is processed through the network. These four parameters are signal isolation, information rate, information integrity, and the availability of these services over time [Shaw, 1998]. Once formulated, these four parameters serve as the minimum instantaneous capability requirements the system must meet to satisfy the customer.

Table 3.1 translates the GINA “Quality of Service” parameters into capability metrics for the SSI mission. These metrics assess how well the customer requirements presented in the previous section are met. Isolation refers to the ability of a system to isolate and distinguish information signals from different sources within the field of view [Shaw, 1998]. For an SSI, the cluster’s angular resolution, which is a function of the maximum vector baseline between a pair of collector satellites in the array, determines the smallest sized objects the SSI can image and discriminate between in the field of view. Rate measures the speed at which the system transfers information between the sources and sinks in the network [Shaw, 1998]. In an imaging system, the imaging rate is simply the total number of images the system can produce per unit time. Integrity is a measure of the quality of the information being transferred through the network. In the case of an SSI, the integrity of an individual image is a function of the u-v coverage used to obtain that image and can be quantitatively evaluated by calculating the mean square error (MSE) of the image, which is a comparison between an idealized point spread function (PSF) and the true PSF for a particular u-v coverage [Kong, 1998]. SSI architectures with greater integrity will produce images with less ambiguity. Finally, availability characterizes the instantaneous probability that information symbols are being transferred through the network

Table 3.1: The GINA "Quality of Service" Parameters Applied to an SSI

| Capability | SSI Application | Metric |
|---------------------|--|-------------------------|
| Isolation | Acquiring and isolating the target | Angular Resolution |
| Rate | Time to construct an image of the target | Images Per Unit of Time |
| Integrity | Image sensitivity to u-v coverage | Mean Square Error |
| Availability | Sun angles, Imaging time vs. Calibration | % Time in Use |

between all of the sources and sinks [Shaw, 1998]. For the SSI, targets close to the sun, or those whose imaging violates sun avoidance angles within the optical train, reduce the availability of the system. The actual imaging time versus calibration, retargeting, and other tasks also affects the availability of the system. Since availability does not distinguish between the selected architectures, the SSI case study presented in the remainder of this thesis focuses on the first three capability “Quality of Service” parameters.

3.3a Develop System Metrics

To compare all the different architectural concepts that are formulated in the design iteration loop, GINA uses a quantifiable set of metrics – *capability*, *performance*, *cost per function*, and *adaptability* [Shaw, 1998]. Table 3.2 specifically applies these general metrics to the analysis of SSI architectures. These are the metrics that will be used to evaluate all of the SSI architectures.

3.3a.1 Cost Per Function

The cost per function metric provides a clear measure of the cost of an architecture versus its performance. It is a measure of the cost to achieve a common level of performance and includes expected development, launch, failure compensation, and operations costs [Shaw, 1998]. Examples include the cost per billable minute of a telecommunications system or the cost per megabyte of data for a weather reconnaissance system. This metric has always driven the design of commercial space systems, but has only recently been applied to government systems. Recalling that the SSI mission has two customers, the space science and astronomy community as well as the taxpaying community, the cost per function for an SSI is defined as the cost per synthesized image, and is calculated by dividing the total lifecycle cost of the SSI by the total number of images it produces over its mission life. This metric epitomizes the key tradeoff in SSI architecture design. The two ways to lower the cost per image are to decrease total

Table 3.2: SSI System Architecture Metrics

| Metric | SSI Application |
|-------------------|--|
| Capability | u-v Coverage, Image Quality (MSE), Angular Resolution, and Imaging Rate (images/month) |
| Performance | Total Number of Synthesized Images |
| Adaptability | Sensitivity of CPF to Assumptions and Requirements |
| Cost Per Function | Cost Per Image |

system cost and increase the number of images the system may produce over its lifetime. System cost may be reduced by using fewer spacecraft. Increasing the number of images, on the other hand, requires a decrease in the time to produce a single image as well as an increase in the total mission design life. This drives the architecture towards using more spacecraft, which increases the total system cost. Finding the optimal set of design parameters in the system architecture trade space between these two conflicting goals of maximizing performance and minimizing cost is one of the objectives of this work, and is addressed in greater detail in the results of the system architecture analysis of Chapter 7.

3.3a.2 Performance

While the four capability “Quality of Service” parameters introduced in Section 3.2 measure how well the architecture meets the capability requirements at any instantaneous point in time, the performance metric measures how the architecture satisfies the demands of the market over the entire life of the mission [Shaw, 1998]. For an SSI, the performance may be expressed as the total number of images the system produces over the mission design life. To calculate this quantity, however, the additional complication of taking into account all of the possible failures that may occur within the different components of the system must be taken into account. As individual payloads or satellites fail over time, the imaging rate of the system will decrease while attempting to maintain the same pre-failure level of integrity (image ambiguity). Conversely, an identical imaging rate could be maintained, but only by sampling fewer spatial frequencies (u-v points) in each image, thus reducing the integrity of the images. To take into account potential failures and the effect they have on system performance, a reliability model is needed. This model, which uses the technique of Markov modeling to compute total system degradation and performance, is developed in Chapter 5.

3.3a.3 Adaptability

In GINA, adaptability is a measure of how flexible a Distributed Satellite System is to changes in design assumptions and mission requirements [Shaw, 1998]. In one sense, adaptability may be thought of as the sensitivity or elasticity of the cost per function of a particular architecture to incremental changes in an assumption or requirement. For the SSI mission, potential assumptions that could be altered to measure architecture sensitivity include component costs, learning curve slopes, and component reliabilities. In another sense,

adaptability may be thought of as the flexibility of a particular architecture to a new set of mission requirements, such as the mission design life. An example of flexibility for an SSI might be the ability of an architecture to transition from an imaging mission to a planetary detection mission in order to garner greater advocacy for the mission’s development. The adaptability metric is explained in detail in Chapter 7.

3.3b Functional Analysis

3.3b.1 Model the System as a Network

Modeling a Distributed Satellite System as a network entails defining all of the origin-destination (O-D) pairs in the system. For an SSI, the origin is the object being imaged and the destination is where the final image is assembled, either in a computer on the combiner itself, at a groundstation, or at a control/data center. In between O-D pairs, the electromagnetic radiation passes through multiple collectors to be interfered in, perhaps, multiple combiners. Tracking the functionality of this network of O-D interconnections, which impacts both the imaging rate and cost, requires probabilistic models of network failures over the lifetime of the mission. A probabilistic reliability model is developed in Chapter 5. Modeling a system in this manner also allows for the application of network optimization algorithms to the system design.

3.3b.2 Identification of the Key Design Parameters

The matrices in Tables 3.3 and 3.4 show the effect of the design variables, assumptions, and requirements on the four capability “Quality of Service” parameters. The explanation below

Table 3.3: Matrix of the GINA Capability Parameters vs. SSI Architecture Design Variables

| Design Variable | Isolation | Rate | Integrity | Availability |
|------------------------------|------------------|---|--|------------------------------|
| Total Number of S/C | NA | Increases by reducing the # of reconfigurations | Improves by increasing the # of u-v points | Decreases due to calibration |
| Functionality of the S/C | NA | Increases by reducing the # of reconfigurations | NA | NA |
| Number of Combiner Payloads | NA | Increases by allowing for simultaneous measurements | NA | NA |
| Number of Collector Payloads | NA | Increases by reducing the # of reconfigurations | Improves by increasing the # of u-v points | Decreases due to calibration |

Table 3.4: Matrix of the GINA Capability Parameters vs. SSI Assumptions & Requirements

| Design Variable | Isolation | Rate | Integrity | Availability |
|-------------------------|---|---|--|--------------|
| Payload Mass | NA | Decreases by increasing the reconfiguration time | NA | NA |
| Payload Power | NA | Decreases by increasing the reconfiguration time | NA | NA |
| Array Geometry | NA | Increases or Decreases, depending upon the existence of redundant baselines | Improves or Worsens, depending upon the existence of redundant baselines | NA |
| Maximum Baseline | Improves by increasing the angular resolution | Decreases by increasing the reconfiguration time | NA | NA |
| S/C Propulsion System | NA | Increases or Decreases, depending upon thrust | NA | NA |
| Component Failure Rates | NA | Decreases by increasing the # of reconfigurations | NA | NA |

each parameter states how increasing that design variable affects that capability parameter. If a design variable does not affect a particular capability parameter, an *NA* for not applicable is listed. For example, the total number of spacecraft in the SSI is shown to affect the rate, integrity, and availability of the system. As the total number of spacecraft in the array increases, the number of available baselines to sample the u-v plane increases. For an image with a given number of sampled spatial frequencies (integrity requirement), this reduces the total number of required array reconfigurations and thus increases the imaging rate. In snapshot mode, the fact that more spacecraft provide more interference baselines reduces image ambiguity and thus improves image integrity. Finally, the availability of the system may decrease as the total number of spacecraft increases, because the total calibration time increases.

Notice that almost all of the design variables affect the imaging rate of the system, while relatively few design variables affect the isolation, integrity, or availability of the SSI. In fact, the isolation capability of an SSI is a function of angular resolution, which is strictly a function of the largest baseline in the cluster, independent of all other parameters. Likewise, the integrity is a function of the u-v coverage of the array, which is strictly a function of the chosen imaging locations. Any SSI cluster can achieve any desired isolation capability (maximum baseline) and integrity capability (imaging locations). For these reasons, isolation and integrity are held

constant in the trade studies as will be explained in greater detail in Chapter 4. The capability discriminator between competing SSI architectures will then be the imaging rate. In this case study, the payload mass, payload power, array geometry, spacecraft propulsion system, and component failure rates are held fixed for each viable architecture. From this matrix in Table 3.3, the key design variables that affect the imaging rate are:

1. The number of spacecraft in the array.
2. The functionality of the spacecraft (modular and multifunctional vs. single function design satellites).
3. The number of combiner and collector payloads in the array (redundancy).

3.4 Derive Top-Level Architecture(s)

A top-level architecture may be derived by allocating values to the design variables listed in Table 3.3. The baseline architecture is usually taken from an existing design. Alternate architectures are then developed by changing one or more of the baseline architectures parameters. The chosen baseline architecture is the New Millennium Interferometer (NMI) proposed for the Deep Space 3 (DS3) mission. The NMI architecture, illustrated in the top left corner of Figure 7.1, contains one combiner payload and two collector payloads, each of which resides on a separate spacecraft bus. Alternate architectures are also illustrated in Figure 7.1.

3.5 Evaluate Architecture(s)

Now that the key trades have been identified and architectures have been proposed, the next step is to develop the simplest models that will quantitatively capture the system metrics in Section 3.3a. For this case, three separate models are required – a capability, reliability, and cost model. The cost per function (*CPF*) metric is calculated by dividing the lifecycle cost of the SSI architecture by the total number of images it produces.

$$CPF = \frac{\$Lifecycle}{\#images} \quad (3.1)$$

A cost model is needed to compute the numerator of this expression. The cost model in Chapter 6 provides a means for estimating the total lifecycle cost of each candidate architecture. Lifecycle cost includes the cost of payload development, spacecraft bus development, launch, and operations. The denominator requires a performance model of the system over the lifetime of the mission in the presence of failures. The capability, or instantaneous performance, model in Chapter 4 calculates how each design variable affects the imaging rate of the SSI. The

reliability model in Chapter 5 determines the probability from the O-D network that the SSI is functioning in each possible state as a function of time. The outputs from these two models are then coupled in a utility function to calculate the total lifetime performance of the architecture, taking into account failures.

$$\# \text{ images} = \int_0^T \sum_{i=1}^n C_i P_i(t) dt \quad (3.2)$$

In this case, T is the mission design life, C_i is the imaging rate in each SSI state i , and $P_i(t)$ is the probability that the SSI is functioning in state i at time t . Once these models have been created, the cost per synthesized image of each architecture may be evaluated and compared (Chapter 7). Finally, the adaptability metric may be applied to determine the sensitivity of each SSI architecture's cost per image to the design variables, assumptions, and requirements (Chapter 7).

3.6 Select Final Architecture

The DSS GINA methodology provides a careful, quantitative analysis of the various system architectures. At the end of this process, the system designers must choose what they believe to be the best design to carry into the next phase of the systems engineering process. While this selection may depend on non-technical, programmatic factors; it is believed that the more quantitative analysis executed up front in the conceptual design stage, the better the final design. Therefore, according to the GINA methodology, the best architecture is the one with the lowest cost per function that still meets all of the capability requirements and fits within the budgetary constraints.

3.7 Summary

In this chapter, we have outlined the GINA systems analysis methodology, or "recipe," for the design and analysis of Distributed Satellite Systems. We have also applied this methodology to the specific example of an SSI. The next three chapters develop the capability, reliability, and cost models that will be required to fully execute the analysis.

Chapter 4

Capability Model

*“One-tenth of the participants produce over one-third of the output.
Increasing the number of participants merely reduces the average output.”*
- Norman Augustine

Merely adding satellites under the guise of distribution will seldom lead to the best architecture. It is important to know not only when distribution adds value, but also when adding more detracts from mission effectiveness. To this end, the cost per function metric was developed in the preceding chapter. The “function” in this metric is defined as the total performance over the mission’s lifetime. For an SSI, this is the total number of images synthesized. Before the cumulative performance over the mission lifetime can be calculated, however, a model must be created to determine the instantaneous performance – the *capability* – of different architectures.

Recall that in Chapter 3 the four GINA capability “Quality of Service” parameters were introduced and mapped onto the SSI mission (Table 3.1). This chapter will now apply these parameters to develop a mathematical SSI capability model. The capability model is divided into three components:

1. Image Quality – u-v Coverage and Mean Square Error (MSE) (Integrity)
2. Angular Resolution (Isolation)
3. Imaging Rate (Rate)

In Table 3.3, we saw that while all the design variables affect the imaging rate of an SSI, only a few design variables affect SSI integrity, isolation, or availability. For this reason, the integrity and isolation capabilities are constrained to be constant in this study and availability is not considered, leaving the rate to be the capability discriminator between competing architectures.

The capability model allows us to see how varying different design architecture variables, assumptions, and requirements – the number of collector spacecraft, number of combiner spacecraft, the degree of multifunctionality in each spacecraft, maximum baseline, array

geometry, and the number of u-v sampled spatial frequencies – affect the instantaneous performance of the system. In other words, the capability model begins to give us a tangible feel for the trade space of SSI design.

The following two sections mathematically define integrity and isolation, and then explain how they are held constant in the capability model. The methodology for calculating imaging rate is then covered in detail. Finally, availability is briefly discussed.

4.1 Integrity – u-v Coverage and Image Quality

Integrity is a measure of the quality of the information being transferred through the network [Shaw, 1998]. In the case of an imaging system, the integrity of an individual image is a function of the u-v coverage used to obtain that image and can be quantitatively evaluated by calculating the mean square error (MSE) of the image. MSE is defined as the comparison between an idealized point spread function, which is the point spread function produced by a filled aperture, and the true point spread function for a particular u-v coverage obtained through a sparse aperture [Kong, 1998].

4.1.1 u-v Coverage

Define u-v coverage as a measure of the number and location of spatial frequencies sampled by an interferometer. Recall from Chapter 2 that the “dirty” image in x-y space is the Fourier transform of the u-v coverage. The better the u-v coverage, the better the image.

One measure of u-v coverage is simply the number of u-v points, or spatial frequencies, sampled. As shown by the u-v coverage Equations 2.3 and 2.4, each baseline between a pair of collector spacecraft provides for two sampled u-v points. Define *snapshot* coverage as an instantaneous account of all the possible baselines at a time t in a single configuration. *High resolution* coverage is then defined as the total account of all the baselines at which measurements are taken of a single target over a period of time t after multiple reconfigurations of the array.

Snapshot u-v coverage is a function of the array geometry. For visible spectrum observations, potential geometric configurations include linear arrays, evenly spaced circular arrays, randomly spaced circular arrays, Golay arrays (for Fizeau, not Michelson, interferometry) and Cornwell arrays. This study assumes that all architectures employ Cornwell arrays for starlight observations as the other arrays are inefficient in comparison [Cornwell, 1988].

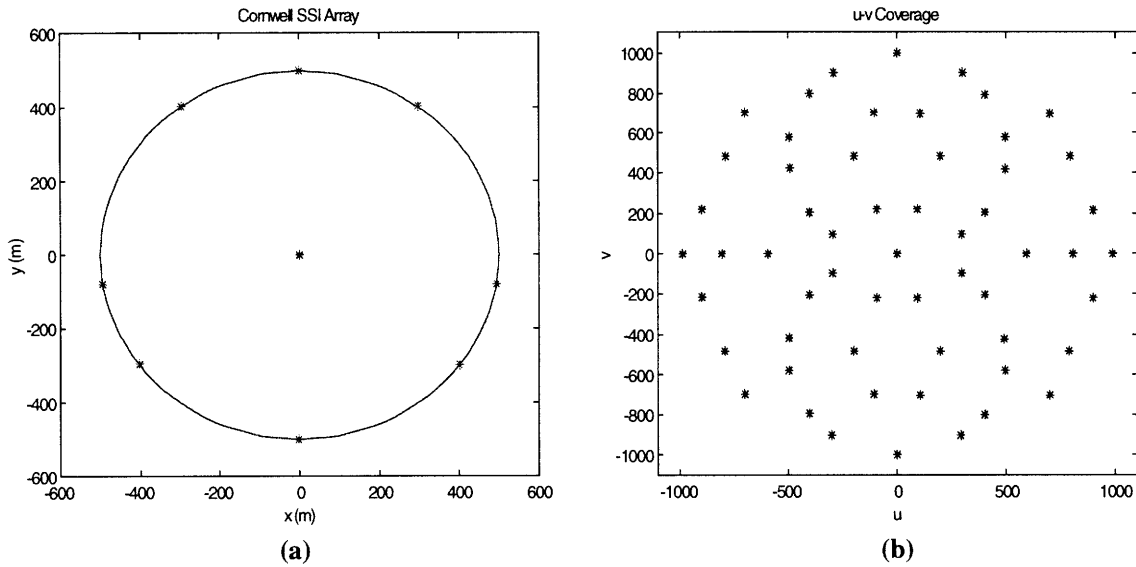


Figure 4.1: 8 Collector Spacecraft Cornwell Array (a) and Associated u-v Coverage (b)

Cornwell arrays are geometric configurations developed by Cornwell to optimize the u-v coverage of a radio interferometer on the surface of the Earth by placing the antennas on the edge of a circle with unique angles with respect to each other [Cornwell, 1988]. Figure 4.1a illustrates an eight collector spacecraft Cornwell array with the combiner satellite in the center and the line-of-sight normal to the figure. Figure 4.1b shows the associated snapshot u-v coverage.

The number of unique baselines ($\#BL$) that exist in a Cornwell array may be expressed as

$$\#BL = \frac{n(n-1)}{2} \quad (4.1)$$

where n is the number of collector spacecraft. Because each baseline provides for the sampling of two spatial frequencies, the total number of u-v points (p) covered in a single snapshot is simply

$$p = n(n-1) \quad (4.2)$$

Thus, the number of points sampled in the u-v plane grows on the order of n^2 ($O(n^2)$) with the number of collector satellites in the interferometer. In other words, the marginal utility, in terms of the *absolute* number of spatial frequencies sampled in a snapshot image, of adding an

additional satellite to the array is always greater than the marginal utility of adding the previous satellite.

We have seen that the marginal utility in terms of u-v coverage of adding an additional collector satellite will always increase with the size of the constellation as long as no baselines are redundant. This will influence the SSI architecture optimization as it will push the designs towards larger arrays with a greater number of spacecraft. However, this comes at the expense of cost. The cost per image metric should capture the best compromise between the two opposing architecture parameters of rate and cost, taking into account the complex interactions with the remaining design variables. For this study, the number of sampled spatial frequencies (u-v points) is held fixed at 100 across all architectures. As a result, architectures with fewer collectors will require more reconfigurations in order to sample this fixed number of u-v points. This is done to prevent integrity from being a discriminator between competing designs. Rather, integrity is fixed as a capability *requirement* that every design must meet in order to be considered a viable architecture. The number of desired sampled spatial frequencies may be set to any value in the capability model code for future studies.

4.1.2 Image Quality

Figure 4.2 illustrates two separate snapshot samplings of the u-v plane by two different arrays. Each snapshot samples 21 u-v points, but at different spatial frequencies. Does this mean that the quality of the image obtained from each of the u-v coverages is identical because

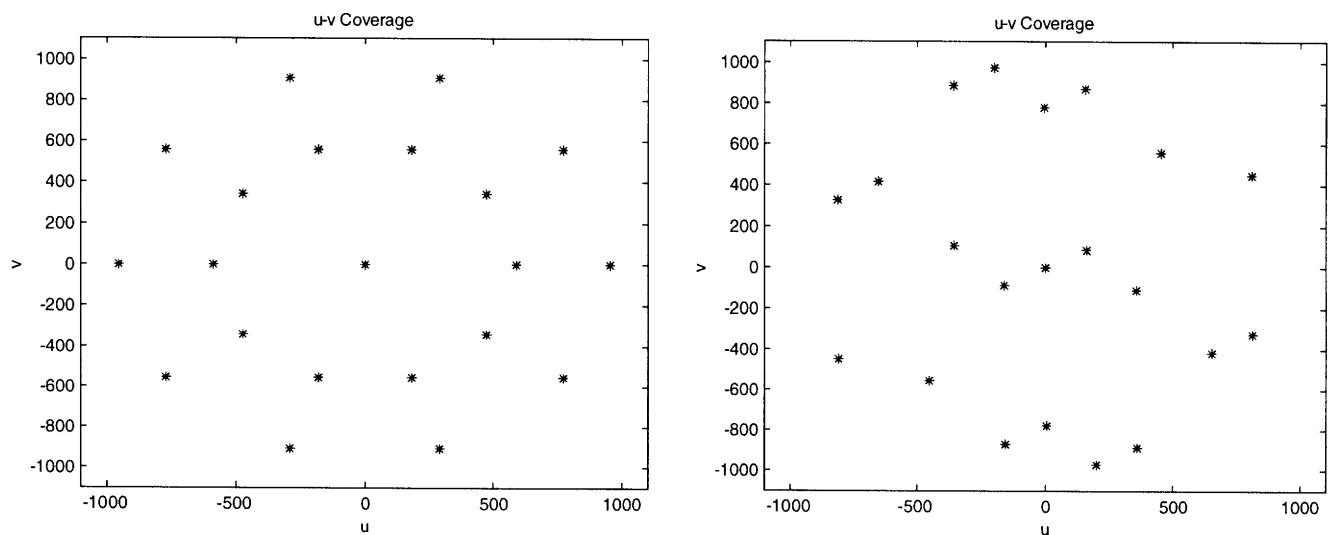


Figure 4.2: Snapshot Sampling of 21 Spatial Frequencies by 5 Collector Cornwell Array (a), and a 5 Collector Randomly Spaced Circle

an identical number of u-v points are measured? The answer to this question is *no* and points to the need for an integrity metric that not only measures the *quantity* of spatial frequencies sampled in the u-v plane, but also the *quality* of the u-v coverage such that it will lead to a suitable image. Two items that will help us develop this second integrity metric are the point spread function and mean square error.

4.1.2.1 Point Spread Function

A point spread function (PSF) is defined as the intensity map of a point source as measured by a single, filled aperture telescope of a given diameter. A filled aperture produces an ideal PSF, whereas a sparse aperture (which is the case for all interferometers) produces a less than ideal PSF, the quality of which is dependent on the u-v coverage of the array. Thus, the shape of an interferometer’s PSF can reveal the quality of a particular u-v coverage.

Figure 4.3 shows a side by side comparison of the snapshot PSF for the five collector Cornwell array in Figure 4.2 and a hypothetical filled aperture with a diameter equal to the maximum baseline of the synthetic aperture (1000 m). While the filled aperture accurately images the source, the snapshot PSF produced by the interferometric array contains too many ambiguities to allow for an accurate image of the source. In fact, if we didn’t know ahead of time that we were looking at a point source, we wouldn’t even know there exists only a single point in our field of view if it wasn’t for the known array factor. For more complex sources with multiple features, even knowledge of the array factor won’t be enough to produce a clean image from the PSF in Figure 4.3a.

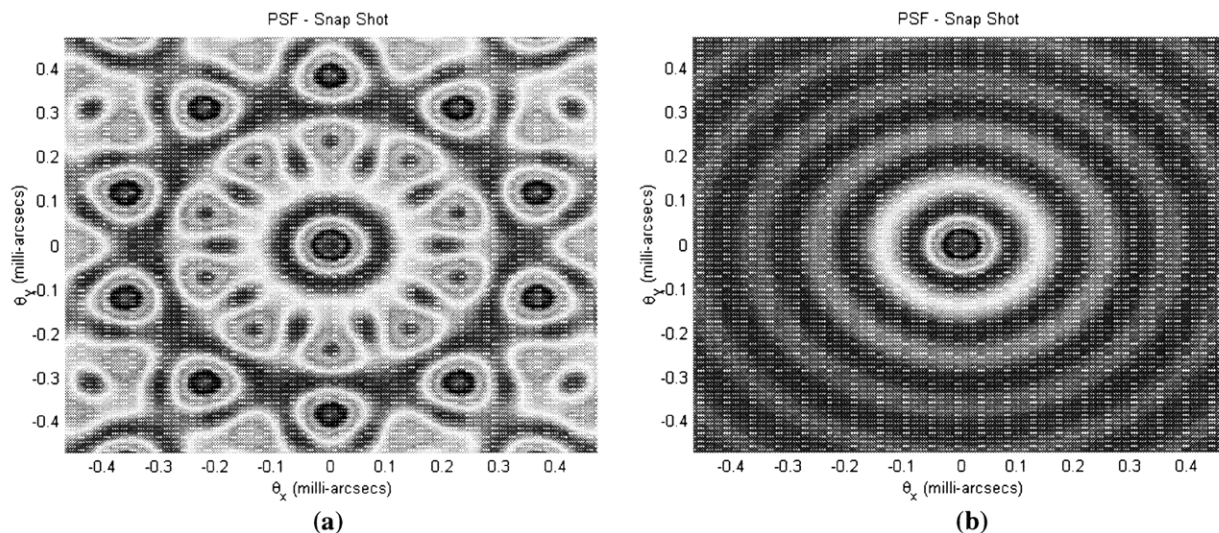


Figure 4.3: Snapshot PSF for a 5 Collector Cornwell Array (a) and a Hypothetical Filled Aperture (b)

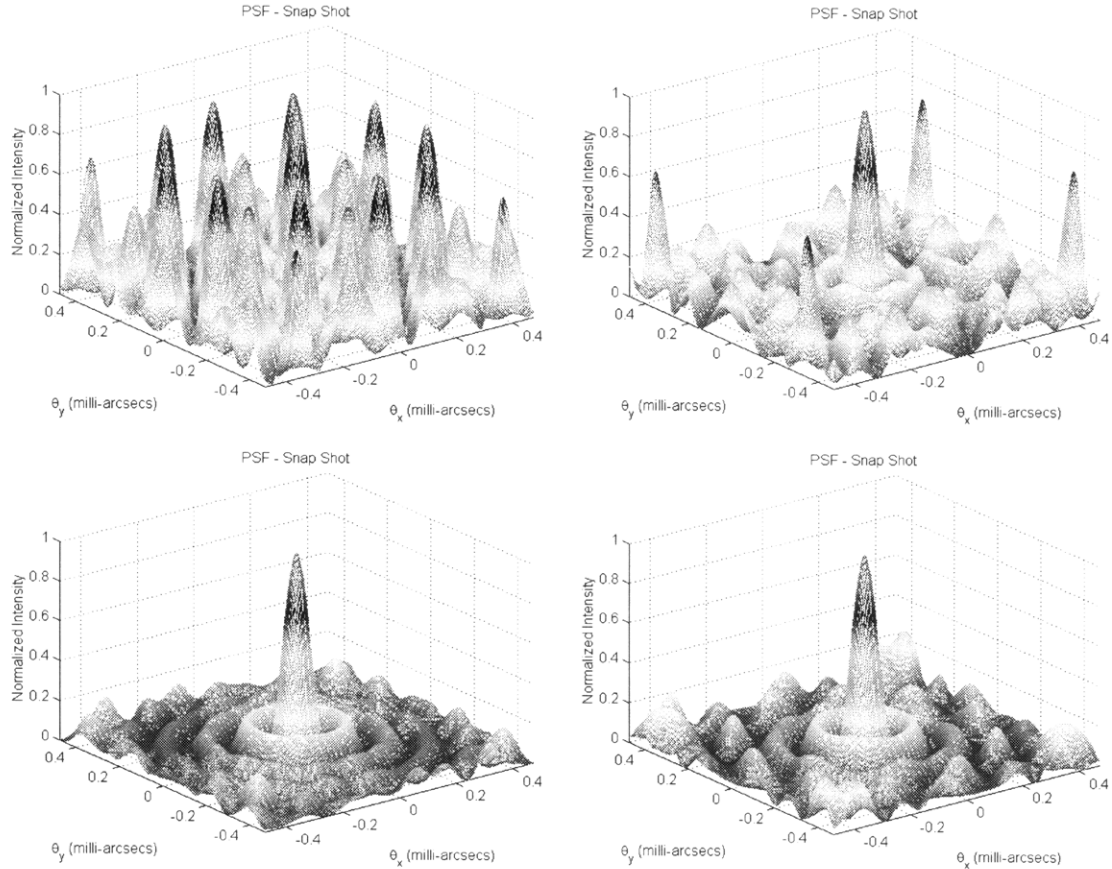


Figure 4.4: Normalized Point Spread Function for the Snapshot Image of Four Separate Cornwell Interferometric Arrays. Clockwise from the top left: 5 Collector Array, 10 Collector Array, 15 Collector Array, and 20 Collector Array.

Figure 4.4 illustrates four different point spread functions for snapshot images taken by a Cornwell array with 5, 10, 15, and 20 collector satellites, respectively. As expected, the quality of the PSF, and thus the image quality, improves as n increases. With only five collector spacecraft, the central peak is indistinguishable from the sidelobes. By the time the array size reaches fifteen spacecraft, a PSF with a large central peak and small sidelobes is achieved.

4.1.2.2 Mean Square Error

By comparing the PSF for a given interferometric array with the idealized PSF, we develop a quantitative metric to evaluate the quality of a particular image. This comparison is executed by calculating the mean square error [Kong et al, 1998]. If I_o is the idealized intensity map, I is the measured intensity map, and p^2 is the total number of pixels in the image, then the MSE is calculated as

$$MSE = \frac{\sum_{i=1}^p \sum_{j=1}^p (I(\Phi_i \Phi_j) - I_o(\Phi_i \Phi_j))^2}{p^2} \quad (4.3)$$

If we know the threshold MSE required to create a suitable image, then we can use this metric to determine the minimum number of collector spacecraft we need in an array of a particular geometry to obtain a suitable snapshot image. For high resolution imaging, using a fixed number of collector spacecraft, this metric determines the minimum number of array reconfigurations. Thus, the MSE may be thought of as an integrity *requirement* the system must meet to create a satisfactory image. Note that any SSI with any number of collectors can meet this requirement by using the same imaging locations. However, for high resolution imaging, clusters with more collector spacecraft will be able to move through the same number of imaging locations faster than clusters with fewer collector spacecraft. This will become important when we begin to assess the imaging rate of the different architectures. In this study, it is assumed that 100 sampled spatial frequencies using Cornwell configurations at different evenly spaced radii from the combiner will lead to a satisfactory MSE. Appendix A illustrates the array geometry, u-v coverage, PSF, and MSE for each of the 11 architectures evaluated in this study.

4.2 Isolation - Angular Resolution

Angular resolution is defined as the smallest angle that can be resolved between two locations on a target source and determines the fineness of detail in the image. The greater the angular resolution, the greater the capability of the interferometer to *isolate* the signal of interest and discriminate between objects within the field of view. The angular resolution (θ_r) of an interferometer is proportional to the wavelength of observation (λ) and is inversely proportional to the maximum baseline (B).

$$\theta_r = \frac{\lambda}{B} \quad (4.4)$$

The larger the baseline, the better the angular resolution. This study assumes observations will be carried out in the visible spectrum, with a central wavelength at $\lambda=550$ nm. Future systems, such as the Terrestrial Planet Finder, will most likely operate in the IR spectrum ($\lambda=12-17$ μm).

For this study, the angular resolution was held constant by fixing the maximum baseline for all SSI arrays at 1000 m. However, the model has been developed such that the maximum baseline, and thus the angular resolution, could become an independent design variable if one so chooses.

4.3 Rate - Imaging Rate

Rate measures the speed at which the system transfers information between the sources and sinks in the network [Shaw, 1998]. For an SSI, the source is the object being imaged and the sink is where the final image is assembled, either in a computer on the combiner itself, at a groundstation, or at a control/data center. In an imaging system, the imaging rate is simply the total number of images the system can take per unit time. While integrity and isolation have been held fixed in this analysis, rate has not and will be the capability discriminator between competing architectures. Recall from Table 3.3 that all of the independent SSI architecture variables affect the imaging rate.

4.3.1 Modeling Imaging Rate

For an SSI, let us define temporal resolution as the time it takes to obtain a single image. The inverse of this quantity is the rate at which the system can obtain images – the imaging rate. Imaging rate is an important capability metric as it directly determines how many targets can be imaged in a given amount of time or the entire system lifetime. In other words, the imaging rate of an SSI dictates the amount of information learned.

Figure 4.5 illustrates the steps involved in the imaging process for an optical SSI. First, all of the collector satellites within the array must acquire the target. After the target has been acquired, the array must acquire its internal metrology system to accurately determine the relative positions of all of the satellites. Next, the pathlengths between the two collector satellites whose science light will be interfered must be coarsely equalized. Once the pathlengths have been coarsely equalized, the process of searching for and acquiring the fringe may begin. Upon finding a fringe, its magnitude and phase are measured over the required integration time. After measuring the fringe, three different courses of action may be taken. A new vector baseline (pair of collectors) may be chosen for the next fringe interference measurement, the entire array may be reconfigured, or the image may be generated because enough spatial frequencies have been sampled.

Table 4.1 lists the estimated amount of time to carry out each of these steps. The metrology acquisition, source light integration, and new baseline acquisition times are based on NASA JPL studies [Linfield, 1998]. The fringe search is a function of the source magnitude/brightness and the pathlength delay. If the pathlength delay between the two science light beams can be estimated to within 2 mm, then given a fringe search rate of 1 $\mu\text{m/s}$, the total

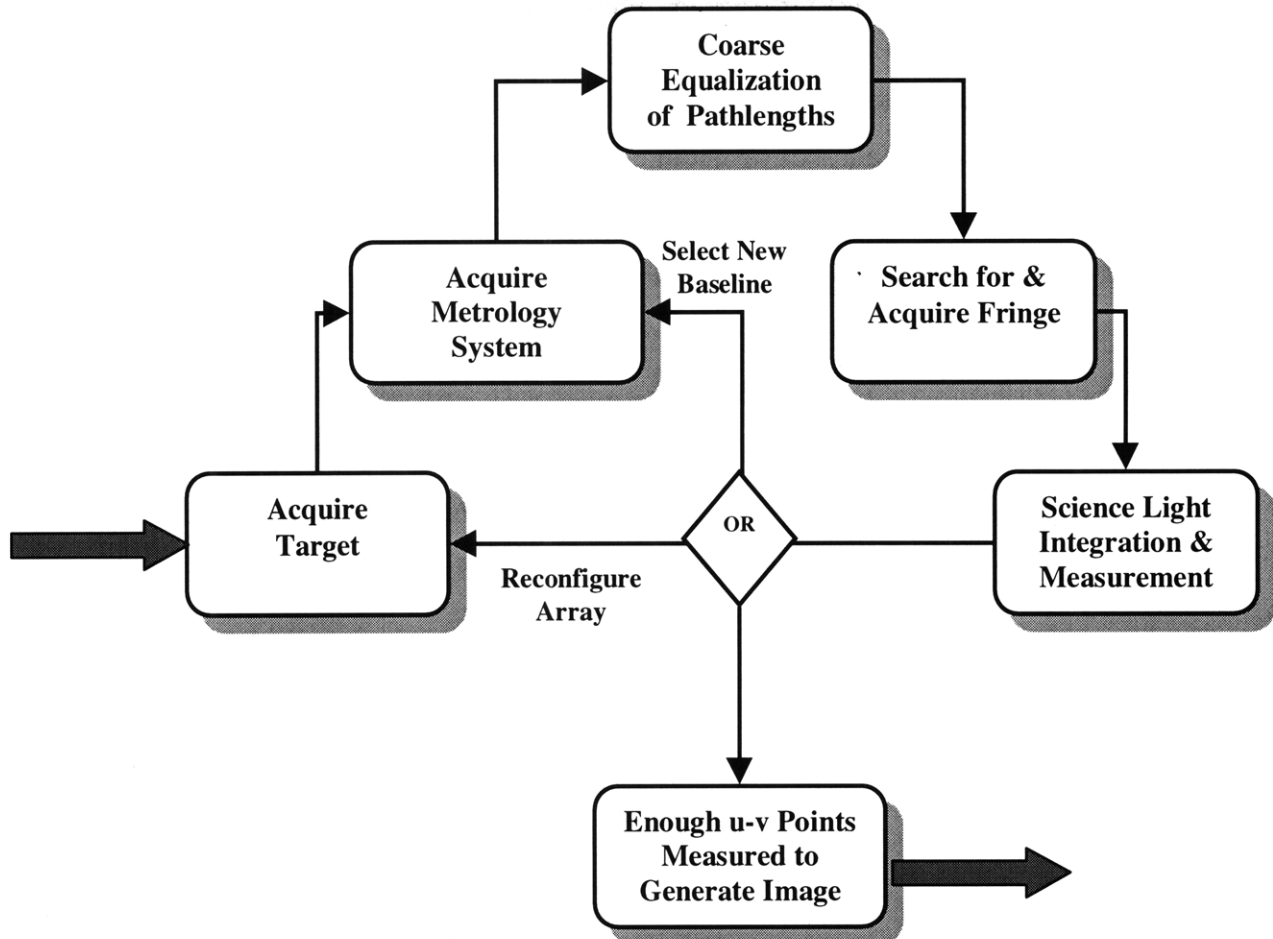


Figure 4.5: Optical SSI Temporal Model

fringe search time can range from a couple of seconds to a maximum of 2000 seconds. Because this number varies for each baseline, we used the median value of 1000 sec for the model. The target acquisition and pathlength equalization times were estimated by the author. Finally, the total array reconfiguration time varies on a case by case basis because it is a function of the maximum baseline, reconfiguration distance, number of required reconfigurations, propulsion system thrust, and spacecraft mass. Appendix B lists the cumulative amount of time required to execute each of these tasks for each of the 11 architectures examined in this study.

Table 4.1: Estimated SSI Optical Imaging Task Times

| Task | Estimated Time (Sec) | Symbol |
|---|----------------------|----------------------|
| Acquire Target | 600 | T_{target} |
| Acquire Metrology | 30 | $T_{metrology}$ |
| Equalize Science Light Pathlengths | 60 | $T_{equalize\ path}$ |
| Search for and Acquire Fringes | 1000 | $T_{fringearch}$ |
| Science Light Integration & Measurement | 60 | $T_{integration}$ |
| New Baseline Selection | 30 | $T_{newbaseline}$ |
| Array Reconfiguration | Varies | T_{single_recon} |

Recall that the number of vector baselines ($\#BL$) available in any SSI is a function of both the array geometry and the number of satellites within the array. Let com equal the number of combiners and col equal the number of collectors within the array. The total time required for switching between baselines in a snapshot image is

$$T_{total_newbaseline} = \left(\frac{\#BL - 1}{com} \right) * T_{newbaseline} \quad (4.5)$$

Likewise, the total times required for equalizing all of the pathlengths, acquiring all of the interference fringes, and measuring the amplitudes of all of the fringes are

$$T_{total_equalizepaths} = \left(\frac{\#BL}{com} \right) * T_{equalizepath} \quad (4.6)$$

$$T_{total_fringearch} = \left(\frac{\#BL}{com} \right) * T_{fringearch} \quad (4.7)$$

$$T_{total_integration} = \left(\frac{\#BL}{com} \right) * T_{integration} \quad (4.8)$$

Notice that the addition of one or more combiners into the array reduces the total time of each of these tasks by an integer factor. Summing up each of these tasks gives us the total snapshot image time

$$T_{snapshot_image} = T_{target} + T_{metrology} + T_{total_equalizepaths} + T_{total_fringearch} \\ + T_{total_integration} + T_{total_newbaseline} \quad (4.9)$$

In contrast to snapshot imaging, the imaging rate model for high resolution imaging must also take into account array reconfigurations. In high resolution SSI images, the number of spatial frequencies to be sampled, or the number of u-v “pixels” p to be imaged, is determined ahead of time. Remembering that the number of baselines ($\#BL$) available during any particular

configuration is a function of the number of collectors in the array, the number of array reconfigurations ($\#recon$) required for a single high resolution image is

$$\#recon = \text{floor}\left(\frac{P}{2*\#BL}\right) \tag{4.10}$$

where floor denotes the operation of rounding down.

The imaging rate model assumes that the distance d_{recon} each collector spacecraft travels during an array reconfiguration is a fraction of the array baseline:

$$d_{recon} = \frac{\left(\frac{B}{2}\right)}{\#recon + 1} \tag{4.11}$$

For example, take the case of a five collector circular array with a maximum baseline B of 1000 m that requires three reconfigurations to sample enough spatial frequencies for a single image. The first set of u-v pixels will be measured at a radius of 125 m, the second set at 250 m, the third set at 375 m, and the final set at 500 m (Figure 4.6). While the reconfiguration profile shown in the figure is rather simplistic, it is sufficient to capture the physics of spacecraft maneuvering.

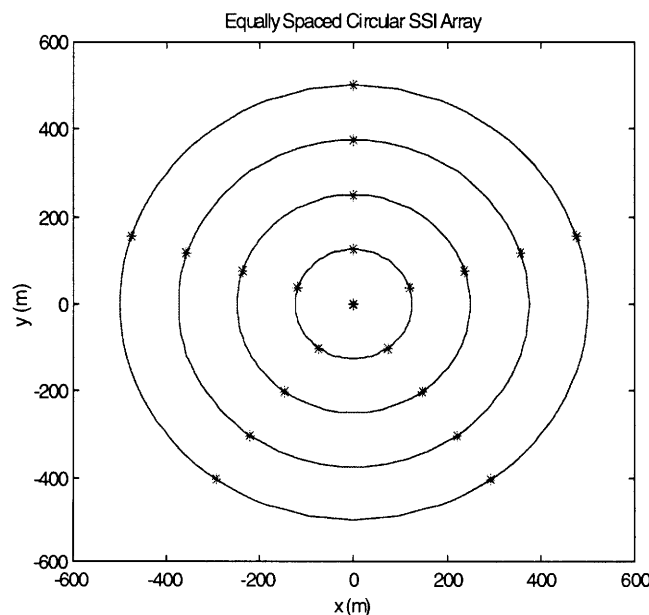


Figure 4.6: Array Reconfiguration Protocol

The equations of motion for the satellites during array reconfigurations outside of a gravity well may be derived from Newton's second law:

$$F = ma \quad (4.12)$$

where F is the force applied to the collector satellite by its propulsion system (thrust), m is the mass of the satellite, and a is the satellite's acceleration during the array maneuvers.

This imaging rate model assumes that pulsed plasma thrusters (PPTs) are the propulsion device of choice for array maneuvers, even though any propulsion system (chemical, electric, etc.) may be input to the model. NASA JPL has selected PPTs as a strong candidate for their future SSI's due to the high specific impulse (I_{sp}), low mass, and low impulse bit of pulsed plasma thrusters [JPL, 1996]. According to the U.S. Air Force Research Laboratory, standard PPTs have an I_{sp} of 1150 seconds, an impulse bit of $750 \mu\text{N}\cdot\text{sec}$, and a thrust-to-mass ratio of $230 \mu\text{N}/\text{kg}$ [LeDuc et al, 1997]. If standard 5.83 kg PPTs are used, then each PPT applies a force of 1.34 mN to a collector satellite. Assuming a collector satellite mass of 150 kg [Blackwood et al, 1998], the constant acceleration of each collector satellite during continuous thrusting is $8.94 \times 10^{-6} \text{ m/s}^2$.

For linear motion with constant acceleration,

$$x = x_o + v_o t + \frac{1}{2} a t^2 \quad (4.13)$$

where x is the distance traveled by the satellite, x_o is the initial position of the satellite, v_o is the initial velocity of the satellite, and t is the time of travel. Setting x_o and v_o equal to zero and solving for the time of travel gives us

$$t = \sqrt{\frac{2x}{a}} \quad (4.14)$$

Substituting equation 4.12 into equation 4.14 yields

$$t = \sqrt{\frac{2xm}{F}} \quad (4.15)$$

Given the reconfiguration distance x , the spacecraft mass m , and the propulsive thrust F , we now have a relationship to determine the time of travel. In other words, we now know how to calculate the time it takes to reconfigure an SSI during high resolution imaging and can incorporate this calculation into our imaging rate model.

However, one additional modification must be made. The time of travel in equation 4.15 assumes that the spacecraft thrusts continuously from its starting location through its destination location. In reality, however, each collector spacecraft must both accelerate and decelerate in order to *stop at*, not *drift through*, its final location. Currently, the imaging rate model uses a triangular velocity profile, accelerating up until the midpoint of its path of travel, and then decelerating to its final location. This thrust profile was selected as a compromise between other faster and slower profiles. For example, a slower, more fuel efficient velocity profile is the trapezoidal profile, where the spacecraft first accelerates, then coasts, and finally decelerates to its final position. On the other hand, a faster total reconfiguration time could be achieved by measuring fringes from all vector baselines in which a particular spacecraft participates and then reposition that spacecraft while repeating this process for the other spacecraft. In the end, the triangular velocity profile was selected as the best compromise between these two alternate reconfiguration profiles.

For triangular velocity profile array configuration maneuvers, the acceleration distance x_a and deceleration distances x_d are half the reconfiguration distance.

$$x_a = x_d = \frac{d_{recon}}{2} \quad (4.16)$$

The acceleration and deceleration times are then

$$t_a = \sqrt{\frac{2x_a m}{F}} \quad (4.17)$$

$$t_d = \sqrt{\frac{2x_d m}{F}} \quad (4.18)$$

Finally, the time for a single array reconfiguration and the total time for all of the array reconfigurations in a single high resolution image are

$$t_{\text{single_recon}} = t_a + t_d \quad (4.19)$$

$$T_{\text{total_recon}} = t_{\text{single_recon}} * \# \text{recon} \quad (4.20)$$

The total amount of time it takes to perform each of the other imaging functions is

$$T_{\text{total_target}} = T_{\text{target}} * \# \text{recon} \quad (4.21)$$

$$T_{\text{total_metrology}} = T_{\text{metrology}} * \# \text{recon} \quad (4.22)$$

$$T_{\text{total_equalpaths}} = \frac{\left(\frac{p}{2}\right) * T_{\text{equalpaths}}}{\text{com}} \quad (4.23)$$

$$T_{\text{total_fringearch}} = \frac{\left(\frac{p}{2}\right) * T_{\text{fringearch}}}{\text{com}} \quad (4.24)$$

$$T_{\text{total_integration}} = \frac{\left(\frac{p}{2}\right) * T_{\text{integration}}}{\text{com}} \quad (4.25)$$

$$T_{\text{total_newbaseline}} = \frac{\left(\frac{p}{2}\right) * T_{\text{newbaseline}}}{\text{com}} \quad (4.26)$$

Finally, summing the times for each imaging function gives us the total time it takes to obtain a high resolution image with a given number of pixels.

$$T_{\text{highresolution_image}} = T_{\text{target}} + T_{\text{metrology}} + T_{\text{total_equalizepaths}} + T_{\text{total_fringearch}} \\ + T_{\text{total_integration}} + T_{\text{total_newbaseline}} + T_{\text{total_recon}} \quad (4.27)$$

The imaging rate is then the inverse of Equation 4.27.

$$Rate_{Image} = \frac{1}{T_{highresolution_image}} \tag{4.28}$$

4.3.2 Snapshot Imaging Results

We first look at the trends associated with snapshot imaging, in which there are no array reconfigurations. Figure 4.7 plots the total time it takes Cornwell arrays with different numbers of collector and combiner spacecraft to obtain a single snapshot image as computed by the imaging rate model. Array baselines were fixed at 1000 m, while the number of collectors (n) and combiners (m) were allowed to vary. The snapshot imaging times for Cornwell array SSI's containing between 2 and 20 collector spacecraft and 1 and 5 combiner spacecraft range from several minutes to just over 60 hours. In Section 4.1, we set the integrity requirement at 100 sampled u-v points. The vertical line in Figure 4.7 represents this requirement. Snapshot images obtained with arrays to the left of the vertical line do not meet the integrity requirement, while snapshot images from arrays on the right side of the line do. As expected, the imaging time increases $O(n^2)$ with the number of collector satellites within the array. On the other hand, adding additional combiner satellites to the SSI decreases the imaging time in a linear fashion. Thus, we have found that designing two or more combiner satellites into an SSI can significantly reduce the snapshot imaging time of a Cornwell array, even if the array has many collector satellites. Later on, the trades between the reduction in reconfiguration time of having many

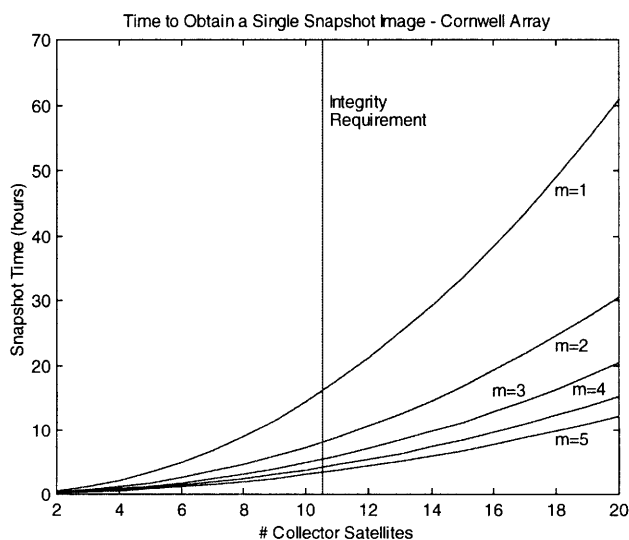


Figure 4.7: Time to Obtain A Single Snapshot Image for Cornwell Arrays with m Combiner Satellites

collector satellites, the improvement in temporal resolution of having multiple combiner satellites, and cost will play a key role in evaluating and optimizing various SSI architectures on the basis of the cost per image metric.

4.3.3 High Resolution Imaging Results – Part 1

Now that we understand the trends associated with snapshot imaging, we may proceed to high resolution imaging. In a sense, high resolution imaging may be thought of as a compilation of snapshot images, with the additional step of reconfiguring the array between snapshots. In Part 1, we look at the effect of the number of collector and combiner spacecraft on the imaging time for images with the fixed integrity requirement of 100 u-v points. In Part 2, we examine how changing the integrity requirements affects the high resolution imaging time.

Figure 4.8 plots the total time it takes to obtain a single high resolution image by a Cornwell array as computed by the imaging rate model. The array baselines were fixed at 1000 m, while the number of collectors (n) and combiners (m) were allowed to vary. Additionally, each high resolution image was developed by measuring 100 u-v points, and each collector satellite was specified to have a mass of 150 kg and use PPTs for propulsive maneuvers.

High resolution (100 u-v point) images for Cornwell SSI's containing between 2 and 15 collector spacecraft and 1 and 5 combiner spacecraft range from several hours to just over 50

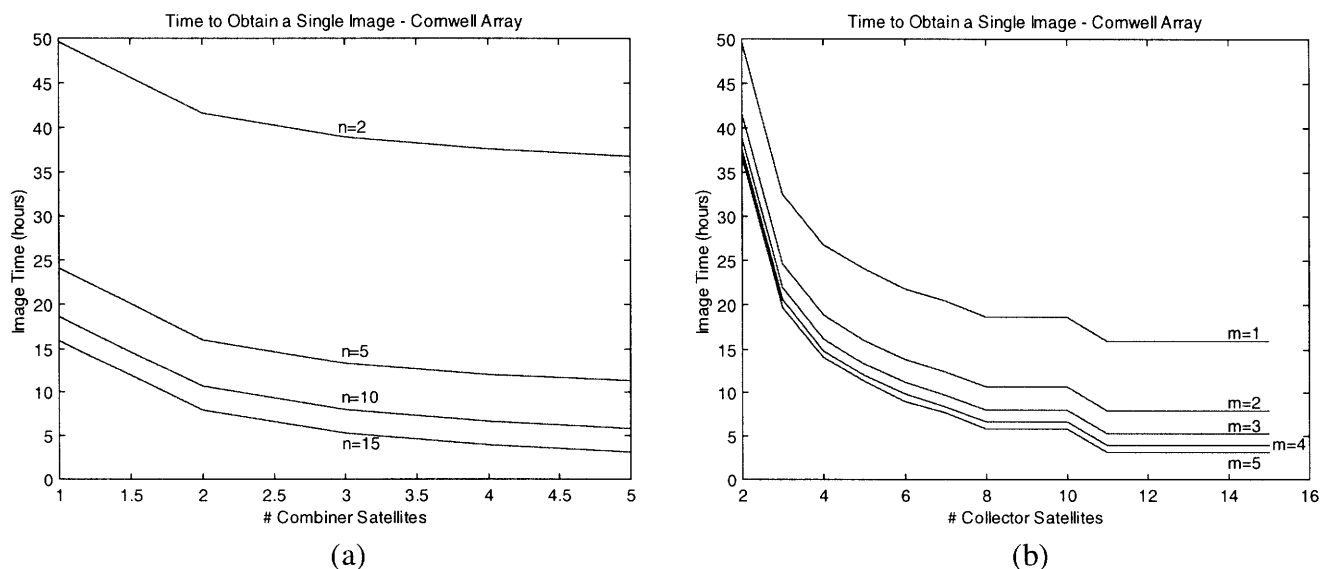


Figure 4.8: Time to Obtain a Single High Resolution Image, with 100 u-v Points using a Cornwell Array, as a Function of the Number m of Combiner (a) and the Number n of Collector (b) Satellites

hours. Figure 4.8a illustrates the relationship between the number of combiner spacecraft in the array and the high resolution imaging time. As was the case with snapshot imaging, increasing the number of combiner spacecraft allows different pairs of collectors to be interfered simultaneously. This in turn decreases the total time to obtain a single high resolution image. Figure 4.8b illustrates the dependence of the high resolution imaging time on the number of collector satellites within the array. This unique, non-linear relationship is a function of the number of vector baselines available at any particular configuration, the integrity requirement, and the number of array reconfigurations required to meet the integrity requirement. Also notice that the fastest imaging times are achieved by clusters with the most total collector and combiner spacecraft.

Figure 4.9a shows the number of available baselines in a Cornwell array with a given number of satellites, where each baseline accounts for two u-v points (sampled spatial frequencies). This curve follows the relationship in Equation 4.1. Figure 4.9b shows the number of array reconfigurations required to meet the 100 u-v point integrity requirement as a function of the number of collector satellites in the array. For an array with only two collector satellites (*i.e.* only one instantaneous vector baseline available), interference measurements over 50 separate array configurations are needed to obtain the image. This number continues to decrease in a non-linear fashion as the number of collector satellites in the array increases. Arrays with 11

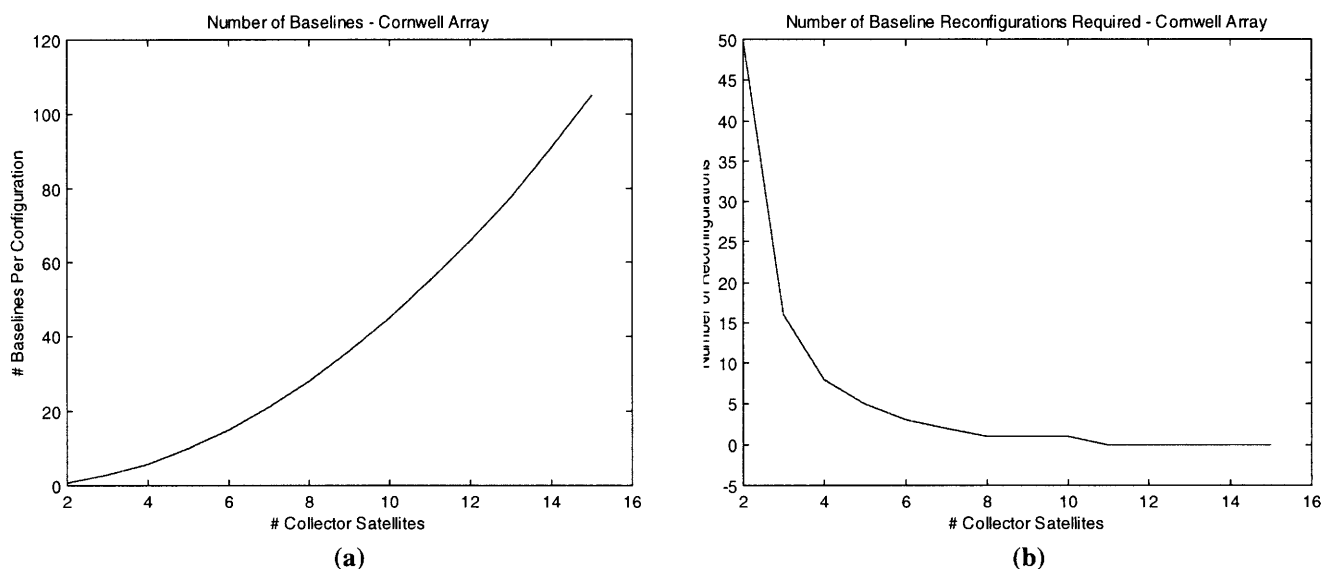


Figure 4.9: Number of Baselines Available Per Configuration (a) and the Total Number of Array Reconfigurations Required to Obtain a High Resolution Image that Samples 100 Different Spatial Frequencies (b)

or more collectors have enough vector baselines available in a single configuration that they can sample 100 spatial frequencies without maneuvering. In essence, they can take the image as a “snapshot.” Also note that the number of required array reconfigurations to obtain a high resolution image is independent of the number of combiner satellites in the cluster.

Figure 4.10 illustrates the reconfiguration distances for these same arrays. The plot conveys how the incremental array reconfiguration distances increase as the number of collector satellites in the array increases. The maximum allowable baseline in these simulations was 1000 m, which corresponds to a 500 m radius for a circular Cornwell array. The array reconfiguration distances are found by dividing the maximum circular radius by the number of configurations required to obtain the image. For example, a nine collector satellite array measures 72 u-v points in a snapshot and thus requires one reconfiguration to complete a 100 u-v point high resolution image. The first configuration takes place at a radius of 500 m and the second configuration at a radius of 250 m (reconfiguration distance equals 250 m). Likewise, a 6 satellite array requires four configurations to complete an image, resulting in a reconfiguration distance interval of 125 m with measurements made at radii of 500 m, 375 m, 250 m, and 125 m. The reconfiguration distance interval drops to zero beyond eleven spacecraft because, for arrays of this size, no reconfigurations are necessary to measure 100 u-v points.

For the same arrays and imaging parameters, Figure 4.11a plots, using the equations of motion developed in Section 4.4.1, the time for a single array reconfiguration as a function of the number of collector spacecraft in the array. Figure 4.11b is then obtained by multiplying the

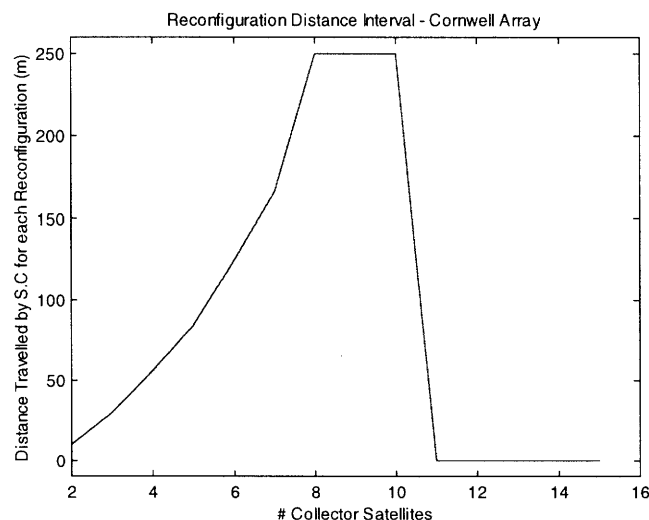


Figure 4.10: Reconfiguration Distance Intervals ($B_{max}=1000$ m, 100 u-v points)

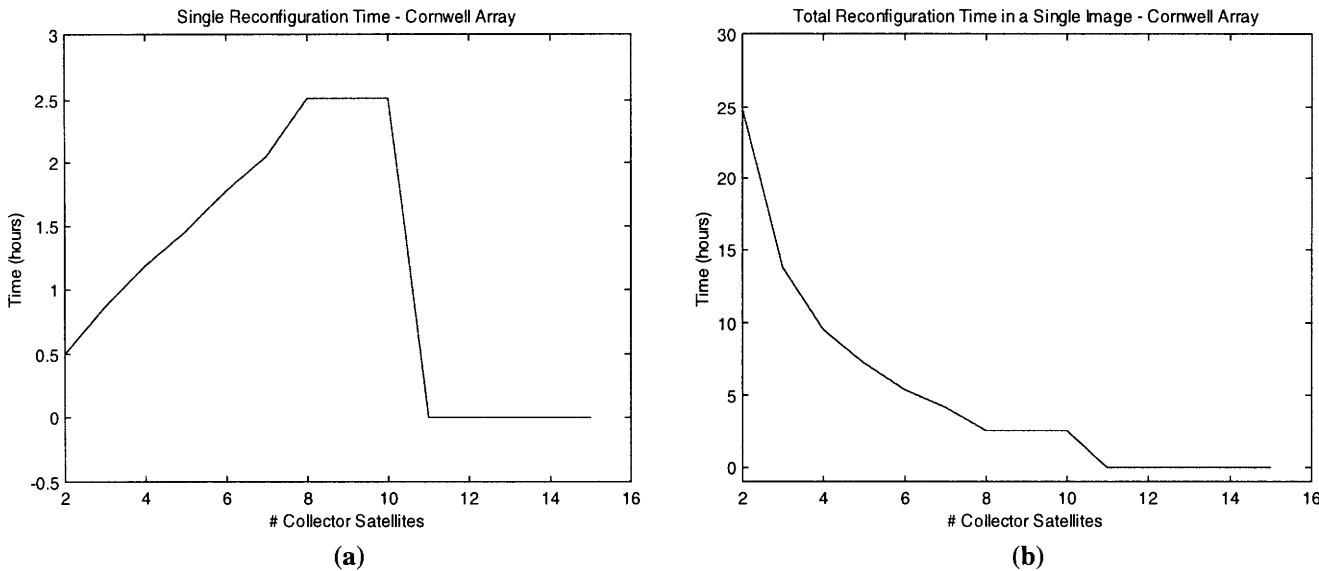


Figure 4.11: Single Reconfiguration Times (a) and Total Reconfiguration Times (b) ($B_{max}=1000$ m, 100 u-v points)

single reconfiguration times by the number of required reconfigurations in Figure 4.9b. The total reconfiguration times are independent of the number of combiner satellites within the array, and are inversely proportional to the number of collector satellites within the array. Appendix B lists, for each SSI architecture examined, the cumulative time for each of the imaging tasks in Figure 4.5. For each architecture, the cumulative reconfiguration time dominated, comprising anywhere from 35% to 59% of the total image time.

Another way to think of imaging rate capability is to determine the number of images an SSI can take over a particular mission lifetime, which ideally is the total mission lifetime divided by the time it takes to obtain a single image. In reality, other factors, such as system reliability, make this calculation more complicated. This will be covered in greater detail in the next chapter, which develops the SSI reliability model. Figure 4.12 contains a surface plot that shows the maximum possible number of images a Cornwell array can obtain in one year as a function of the number of collector and combiner satellites in the array. Inherent in this figure are the integrity requirement (100 u-v points) and the isolation requirement (1000 m maximum baseline). Notice the smooth relationship between the number of combiner satellites in the array the number of images. In contrast, the number of images varies in a non-smooth manner as the number of collector satellites increases. This nonlinear relationship may be traced back to Equation 4.1.

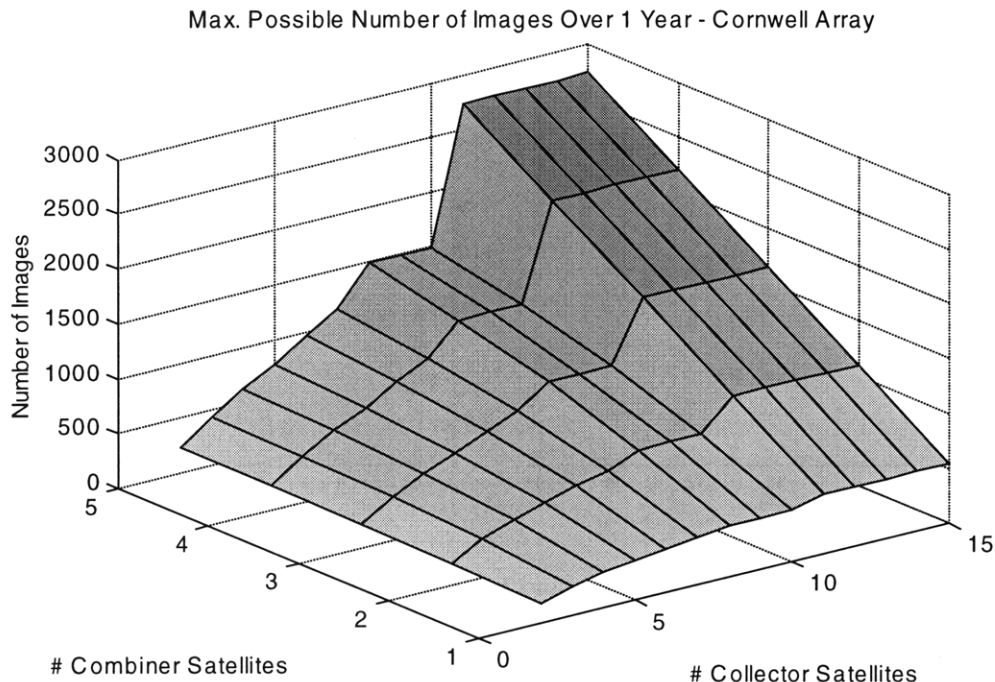


Figure 4.12: Theoretical Maximum Number of Images Possible Over a 1 Year Mission - Cornwell Array

4.3.4 High Resolution Imaging Results – Part 2

In Section 4.3.3, we examined the relationship between the number of spacecraft (collector and combiner) and the imaging time for images with the fixed integrity requirement of 100 u-v points. In this section, we explore how changing the integrity requirement affects the high resolution imaging time.

Figure 4.13 plots the total time it takes to obtain a single high resolution image from a given number of u-v points by a Cornwell array as computed by the model. The maximum baselines and number of combiner satellites in the array were fixed at 1000 m and one, respectively; while the number of collector satellites and the number of u-v points required were allowed to vary. The satellite and propulsion specifications were the same as in the previous case.

Depending upon the number of collector satellites and the integrity requirement, the high resolution imaging time ranged from 1 to 3000 hours. In addition to the $O(n^2)$ relationship already explained, the imaging time is directly proportional to the number of spatial frequencies that must be sampled to develop the image. This makes intuitive sense because each vector baseline measurement and array reconfiguration requires a discrete amount of time, and the number of reconfigurations scales directly with the integrity requirement (number of u-v points).

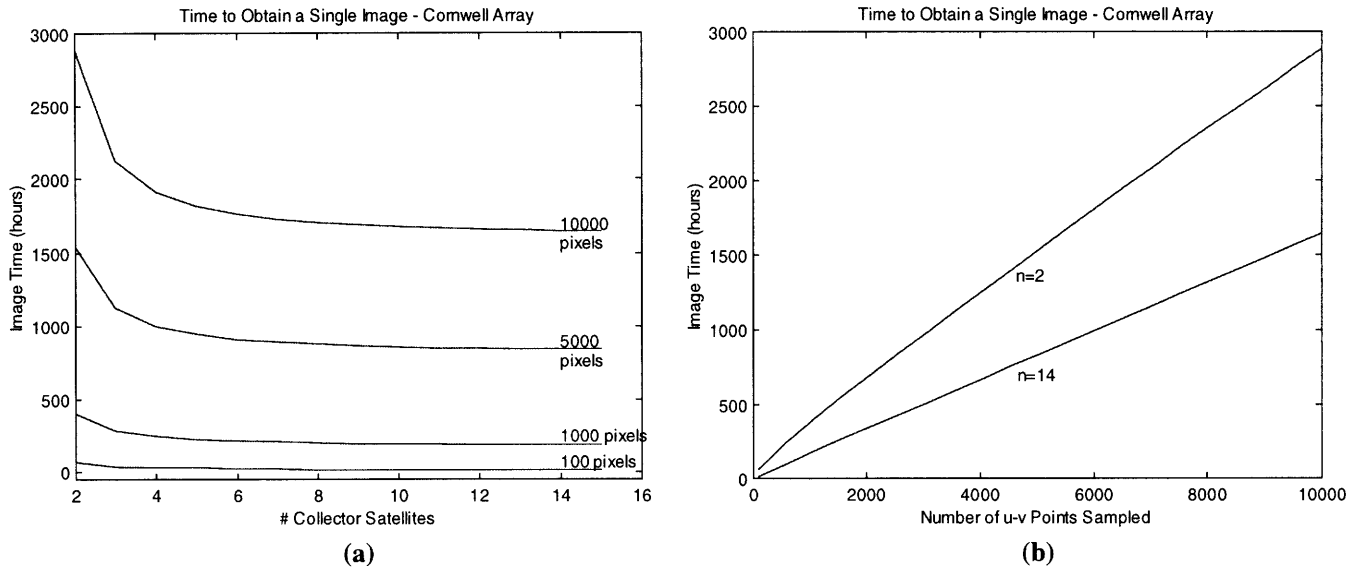


Figure 4.13: Time Required for a Single High Resolution Image with a Cornwell Array as a Function of the Number of Collector Satellites n (a) and u - v Points Sampled (b)

This section has shown that the number of spatial frequencies that must be sampled for high resolution images also affects the imaging rate. This integrity requirement is held fixed at 100 u - v points for the remainder of this study.

4.4 Availability – Percentage of Time Imaging

Availability characterizes the instantaneous probability that information is being transferred between all O-D pairs at a given rate and integrity [Shaw, 1998]. For an SSI, this determines the percentage of time the system is actually imaging. One factor that affects the availability of an SSI is the viewing geometry. If the target itself or the line-of-sight from a collector to a combiner is close to the sun, the SSI is unavailable for that source. Other factors, such as calibration time, may also affect the availability of an SSI. In this study, availability is not modeled.

4.5 Capability Model Summary

The capability model we have developed in this chapter tells us how the number of measured u - v points, image quality, angular resolution, and imaging rate vary with the SSI architecture variables, assumptions, and constraints. This model will enable us to perform a complete DSS analysis of various SSI architectures and will be used to quantify the capability and cost per function metrics for each architecture. The capability model has provided our first glimpse into the SSI design trade space. In the remainder of this work, both the integrity (#

sampled uv points = 100) and isolation ($B_{max} = 1000$ m) are held fixed, leaving only the imaging rate as the capability discriminator between competing architectures. Availability is not addressed in this study.

In this chapter, we have modeled and simulated the *ideal* performance of SSI system architectures. In reality, however, the performance of any system degrades with time and is a function of the system architecture's reliability. Spacecraft failures over time will result in smaller arrays which require more reconfigurations to meet the image integrity requirement. This will reduce the imaging rate and therefore the productivity of the system. The next chapter develops a reliability model for separated spacecraft interferometers so that this productivity versus spacecraft failure dependency can be explored.

Chapter 5

Reliability Model

“Simple systems are not feasible because they require infinite testing.”
- Norman Augustine

Reliability is a difficult characteristic to quantify, particularly when new components are being considered which do not possess an extensive operational and test heritage with documented failure rates. Stochastic methods, such as Markov modeling, are not receiving wide acceptance for this reason as well as the fact that the reliability behavior of a single component on a spacecraft will not necessarily match the expected behavior of a collection of components on a spacecraft. However, replicated components and spacecraft characterize Distributed Satellite Systems (DSS). As more components are added, it becomes reasonable to expect that the behavior of the system will more closely match the behavior that would result if its components behave as statistically expected. In other words, the actual behavior of a system approaches its statistically expected behavior when large sets of samples are made available. Therefore, stochastic reliability analysis becomes more applicable when principles of DSS are employed.

Reliability is defined as the probability of a system meeting its mission requirements over a given period of time under the operating conditions encountered [Gordon, 1980]. The reliability of a system determines the ultimate degree of success for the project, whether the metric of mission success is to generate revenue through a constellation of communication satellites or to gather scientific data with an array of environmental remote sensing spacecraft. A system with a higher reliability will operate in a state of greater utility for a longer amount of time before degrading, increasing mission success. Utility is the productivity of the system as a function of time in the presence of failures. Increased system reliability, however, comes at a cost. For space systems, this cost manifests itself as both an increase in the mass that must be launched into orbit and an increase in system cost. Thus, the boost in system performance provided by a design architecture with a high degree of reliability must be traded versus the cost

of such an architecture. Before carrying out this trade, however, we must develop a model to evaluate the reliability of different SSI design architectures – a reliability model.

The first section of this chapter provides background information on how to improve the reliability of a system. Next, combinatorial mathematical expressions for the total system reliability as a function of the number of combiner spacecraft, collector spacecraft, multifunctional spacecraft, and the time in the mission are derived. The method of Markov modeling to determine the probability of the system being in any particular state at any given time is then introduced. The previous chapter developed a capability model to calculate the instantaneous performance of an SSI. Upon completion of the reliability model in this chapter, these two models are coupled to compute the total performance of an SSI architecture over the *entire mission life*.

5.1 Background

The two recognized methods of improving system reliability are fault avoidance and fault tolerance. Fault avoidance refers to developing a design that completely eliminates all possible failures through generous design margins, the use of the highest quality military standard (MIL-STD) class S components, continuous inspection during manufacturing, and extensive testing before launch [Hecht, 1992]. While ideal, fault avoidance is very expensive to achieve and becomes impractical for large systems with many satellites.

Fault tolerance refers to the ability of a system to continue to function even after one or more of the components within the system fails. This is usually achieved through redundancy. Redundancy comes in many forms – backup, operational, functional, and analytic. Backup up redundancy refers to placing identical components in parallel with the primary component. The identical components can then be brought on line in the event of the failure of the primary. An example of backup redundancy in an SSI would be placing a second combiner payload on the combiner spacecraft in the three spacecraft SFD array. In operational redundancy, the identical components are operational throughout the mission. In the event of a failure, the performance of the system is degraded. Prior to a failure, however, the performance exceeds that of a system with an identical number of payloads that employs backup redundancy instead of operational redundancy. Functional redundancy uses non-identical components which serve another function, but possess the capability to partially pick up the function of the failed component. Finally, analytic redundancy entails the reconfiguration of software in conjunction with a model

of the system behaviour to achieve the function of the failed component. In the SSI case study presented here, only the first two types of redundancy - backup and operational - are considered.

5.2 Total System Reliability

Define system reliability as the probability of obtaining a fringe (R_{Fringe}) through a separated spacecraft interferometer (SSI). Further, divide the SSI system into its three core components - the collector, combiner, and bus. The collector component relays starlight to a combiner. The combiner component interferes the starlight, processes the information, and obtains a fringe measurement. Finally, every spacecraft in the system requires a bus, which performs all of the vital spacecraft functions such as attitude determination and control, communication, etc. Thus, the minimum functionality required to obtain an image is one combiner and two collectors on three separate spacecraft, each with their own functioning bus.

The two extreme SSI architectures that may be employed are heterogeneous arrays in which every satellite functions as a combiner *or* collector (single function design (SFD)) and homogeneous arrays in which all spacecraft can function as both a collector *and* a combiner (modular and multifunctional spacecraft (MAMSC)). Figure 5.1 illustrates both the SFD and MAMSC designs for a three spacecraft interferometer. In the heterogeneous SFD design (5.1a), light is reflected from the two collector spacecraft into the optics of the combiner spacecraft. The three spacecraft define the plane which contains the line-of-sight to the star [Colavita et al , 1996]. Only one baseline is available for sampling the u-v plane per configuration, and failure

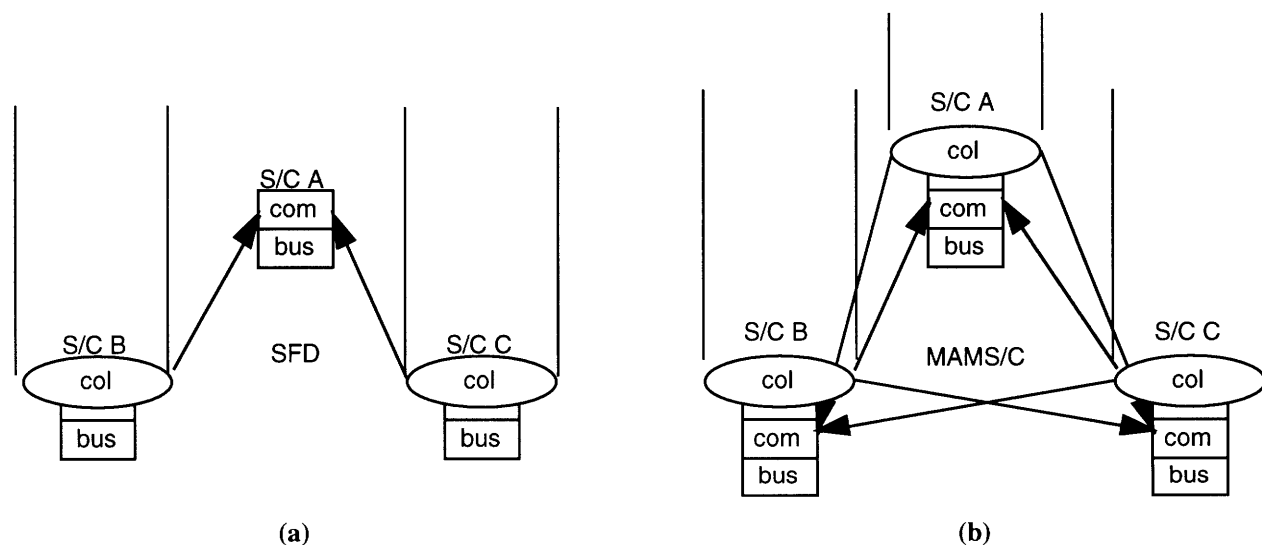


Figure 5.1: Heterogeneous Single Function Spacecraft Design (SFD) (a) and Homogeneous Modular and Multifunctional Spacecraft Design (MAMSC) (b) for a 3 Satellite Interferometer

of any combiner, collector, or bus leads to total system failure. In the homogeneous MAMSC design (5.1b), each spacecraft is at the vertex of an equilateral triangle. The three spacecraft now define the plane normal to the line-of-sight to the star. Each collector relays its light to the two other spacecraft combiners. Three equal length, but different orientation, baselines are available for sampling the u-v plane per configuration. This system can lose one collector or two combiners in a specific combination and still measure fringes and obtain images.

In the SFD configuration, all six components of the system are in series, meaning that if any one component fails, the entire system is useless. The probability of obtaining and measuring a fringe is the product of the reliability of each component in the system.

$$R_{Fringe} = R_{com} R_{col}^2 R_{bus}^3 \quad (5.1)$$

where R_{com} is the reliability of the combiner, R_{col} is the reliability of the collector, and R_{bus} is the reliability of the spacecraft bus.

The reliability R of a component is formally defined as

$$R = e^{-\lambda t} \quad (5.2)$$

where λ is the failure rate of the component and t is the time as measured from the beginning of the mission. With this notation, Equation 5.1 can be rewritten as

$$R_{Fringe} = e^{-(\lambda_{com} + 2\lambda_{col} + 3\lambda_{bus})t} \quad (5.3)$$

Equations 5.4 through 5.7 derive an expression for the total system reliability of an SFD SSI as a function of any number of combiner (m) and collector (n) spacecraft.

$$R_{Fringe} = [1 - (1 - R_{com} R_{bus})^m] [1 - (1 - R_{col1} R_{col2})(1 - R_{col2} R_{col3})(1 - R_{col1} R_{col3}) \dots (1 - R_{col(n-1)} R_{col(n)})] \quad (5.4)$$

If

$$R_{col1}R_{col2} = R_{col2}R_{col3} = R_{col1}R_{col3} = R_{col(n-1)}R_{col(n)} \quad (5.5)$$

then

$$R_{Fringe} = [1 - (1 - R_{com}R_{bus})^m][1 - (1 - R_{col}^2R_{bus}^2)^{\frac{n(n-1)}{2}}] \quad (5.6)$$

or

$$R_{Fringe} = [1 - (1 - e^{-(\lambda_{com} + \lambda_{bus})t})^m][1 - (1 - e^{-2(\lambda_{col} + \lambda_{bus})t})^{\frac{n(n-1)}{2}}] \quad (5.7)$$

By taking the limit of Equation 5.6 as n approaches infinity for SFD arrays with only one combiner spacecraft, $R_{Fringe} \sim R_{com}R_{bus}$. This is because the combiner spacecraft represents a single point failure for any sized SFD array with only one combiner spacecraft.

In the MAMSC configuration, the buses of the three spacecraft may be modeled as being in series, while the combiners and pairs of collectors are in parallel. The probability of obtaining a fringe with this parallel system architecture is one minus the product of the complements of obtaining a fringe through each combiner.

$$R_{Fringe} = 1 - (1 - R_{com}R_{bus}(R_{col}R_{bus})^2)^3 \quad (5.8)$$

or

$$R_{Fringe} = 1 - (1 - e^{-(\lambda_{com} + \lambda_{bus})t}(e^{-2(\lambda_{col} + \lambda_{bus})t}))^3 \quad (5.9)$$

Equations 5.10 through 5.13 derive an expression for the total system reliability of a MAMSC array as a function of the number, n , of spacecraft in the array.

$$R_{Fringe} = 1 - (1 - R_{fringe})^n \quad (5.10)$$

If

$$R_{fringe} = R_{com}R_{bus}(1 - (1 - R_{col}^2R_{bus}^2)^{\frac{(n-1)(n-2)}{2}}) \quad (5.11)$$

then

$$R_{Fringe} = 1 - [1 - (R_{com} R_{bus})(1 - (1 - R_{col}^2 R_{bus}^2)^{\frac{(n-1)(n-2)}{2}})]^n \quad (5.12)$$

or

$$R_{Fringe} = 1 - [(1 - (e^{-(\lambda_{com} + \lambda_{bus})t})(1 - (1 - e^{-2(\lambda_{col} + \lambda_{bus})t})^{\frac{(n-1)(n-2)}{2}}))]^n \quad (5.13)$$

In this case, taking the limit as n approaches infinity for MAMSC arrays with large numbers of spacecraft results in $R_{Fringe}=1$.

Figure 5.2 plots the total system reliability of an SSI at the end of one year as a function of the number of collector and combiner satellites in a heterogeneous SFD array and the number of MAMSC satellites in a homogeneous array. Failure rates were estimated, taking into account the varying complexities and heritage of the three model components. Satellite bus designs have continued to improve over the past 30 plus years. The mttf for commercial communication satellites is typically quoted as 100,000 hr (11.4 yr.) [Gordon, 1980]. For this science mission, assuming enough fuel is on board for 8 years worth of maneuvering, let $mttf_{bus}=8yr=70,080hr$. This corresponds to a failure rate for the bus of $1.427 \times 10^{-5} hr^{-1} = 0.01042 month^{-1}$. The collector is the simplest of the three model components, containing only a flat 12 cm 3-axis gimbaled mirror.

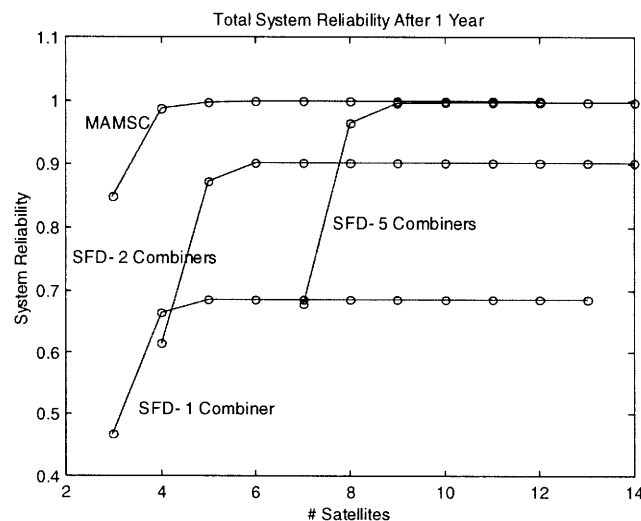


Figure 5.2: Total System Reliability at the End of One Year for SFD and SSI Arrays as a Function of the Total Number of Satellites

Thus, the mttf for the collectors should be much higher. Let $mttf_{collector}=15yr= 131,400hr$. This corresponds to a failure rate for the collector of $7.610 \times 10^{-6} hr^{-1} = 0.005555 \text{ month}^{-1}$. The combiner represents a newer, high-risk technology with more moving parts. Thus, its reliability will be lower. Let $mttf_{com}=4yr=35,040hr$. This corresponds to a failure rate for the combiner of $2.8539 hr^{-1} = 0.02083 \text{ month}^{-1}$.

As one can see in Figure 5.2, the number of combiner spacecraft in an SFD array exerts a greater influence on the total system reliability than the number of collector spacecraft. In essence, it sets an upper bound on the system reliability. This is due to the fact that the combiner, a complex system of moving optical and mechanical components, has a failure rate that is approximately three times greater than the failure rate of a collector. Additionally, arrays typically have fewer combiners than collectors, yet all light must eventually pass through the combiners. Thus, one may conclude that adding one or more additional combiner spacecraft to a heterogeneous SFD SSI array can significantly increase the reliability and useful lifetime of the system. The figure also reinforces what we learned by taking the limit of Equations 5.6 and 5.12 – that as the number n of MAMSC spacecraft increases, the total system reliability approaches unity. This is due to the parallel redundancy present in such an architecture. Finally, for a given number of total spacecraft, the MAMSC array always has a greater total system reliability than the SFD array.

Figure 5.3 plots the total system reliability as a function of time and the number of collector or combiner spacecraft in the SFD array. Figure 5.3a assumes three collector satellites

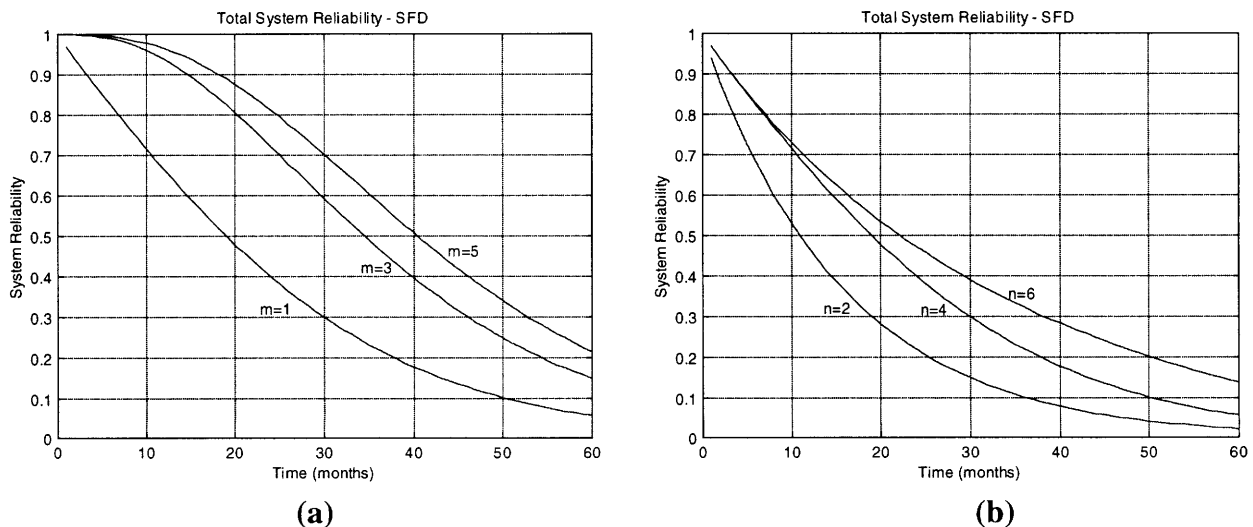


Figure 5.3: Total System Reliability as a Function of Time and the Number of Combiner (m) Spacecraft (a) and the Number of Collector (n) Spacecraft (b) for an SFD SSI Array

with m combiner satellites and Figure 5.3b assumes one combiner satellite with n collector satellites. Both plots lead to the same conclusions that we have already drawn from the mathematical derivations in this chapter. First, total system reliability decreases exponentially with time. Second, the slopes in both plots reinforce the observation that of all the architecture variables, the number of combiner spacecraft in the array exerts the greatest influence on the total system reliability due to its high failure rate and critical path role.

Figure 5.4 plots the total system reliability as a function of time and the number of MAMSC spacecraft n in a homogeneous array. Again, we see that while the reliability of the array decreases exponentially with time for small arrays, the reliability of large arrays remains near unity. Again, for a given number of spacecraft in the array, the homogeneous MAMSC architecture will always provide a greater total system reliability than an SFD architecture. Thus, if total system reliability were the only metric, then the MAMSC architecture would always be best. Total system reliability may not be the best metric for judgment, however, because it does not tell the entire story. Increased system reliability through redundancy is conventionally accompanied by increased cost. In this case, the cost is the total system mass that must be built and then launched from Earth. A given increase in R_{Fringe} may not be practical if it requires a prohibitively large increase in the mass of the system, such that the system can no longer be constructed within budget or launched on the vehicle of choice. In order to make a more realistic comparison, the model outputs of performance and cost will also have to be taken into account in designing the system architecture. These trades are performed in Chapter 7.

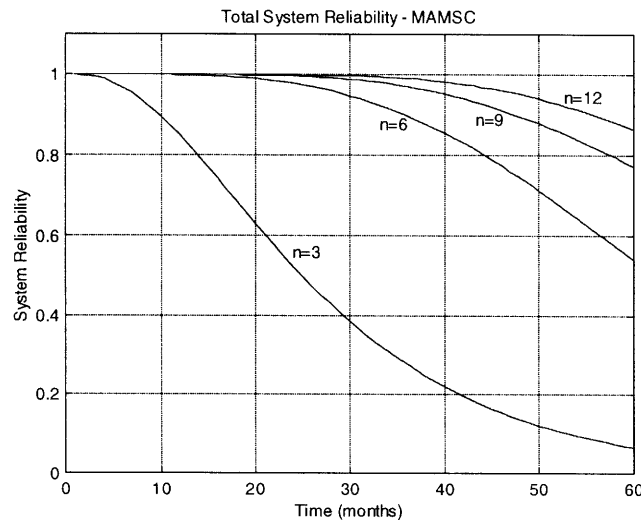


Figure 5.4: Total System Reliability as a Function of Time for MAMSC Arrays with n Spacecraft

5.3 Markov Modeling

The combinatorial formulas in the previous section tell us *if* the system is functioning, but not *how well* the system is functioning. In order to do a complete analysis and comparison of the different SSI architectures, we need a method for determining the probable state of the system. In other words, we need to know how *effectively* the mission is being accomplished when failures occur. For this, we will use Markov modeling.

Markov models have been traditionally used to evaluate the reliability of complex systems. In order to apply a Markov modeling methodology, the states of the system must be time dependent, sequential, and mutually exclusive. If the system satisfies these requirements, then a set of differential equations can be written to model the evolution of the system. By taking advantage of the Markov property, which states that given full knowledge of the current state of the system, one can predict all future states by integrating the set of differential equations, irrespective of the past states of the system [Gelb, 1974].

In this section, we illustrate by example how to create a Markov model for a Distributed Satellite System and how to use this model to learn important information useful in the design of the system architecture. We do so by creating Markov models for a three-spacecraft SFD array (Figure 5.1a) and a three-spacecraft MAMSC (Figure 5.1b) array [Jilla et al, 1997]. All other Markov models referenced in this thesis were implemented in the same manner as the two models we develop here.

The first step is to develop a fault tree diagram illustrating all the possible different modes of failure for each design (Figures 5.5 and 5.6). Recall that the minimum functionality required to measure interference fringes and develop images with an SSI is one combiner and two collectors, all three of which must be on separate spacecraft with functioning buses. In the SFD design, as illustrated in Figure 5.5, the system fails when any single component - collector, combiner, or bus - fails. On the other hand, individual components or even combinations of components can fail without leading to system failure in the MAMSC design. Figure 5.6 illustrates which component failure combinations will lead to system failure for the MAMSC design. Notice the complexity of the fault tree for the MAMSC architecture. This results from the multiple ways in which the three SSI core components can fail and still leave the system operable. This is the benefit of redundancy.

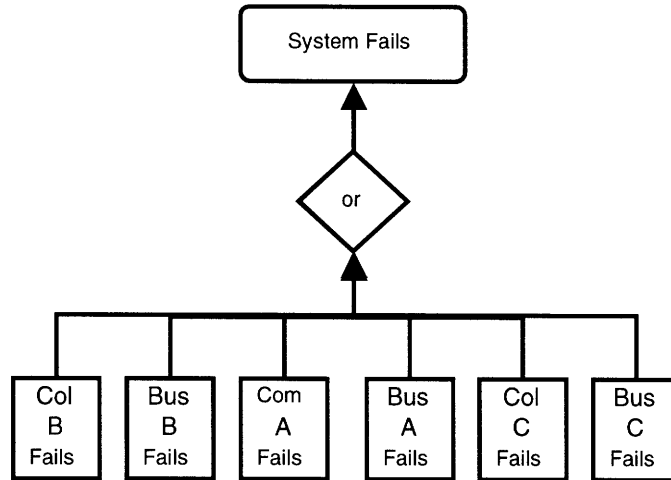


Figure 5.5: Fault Tree for the Three Spacecraft SSI SFD Architecture

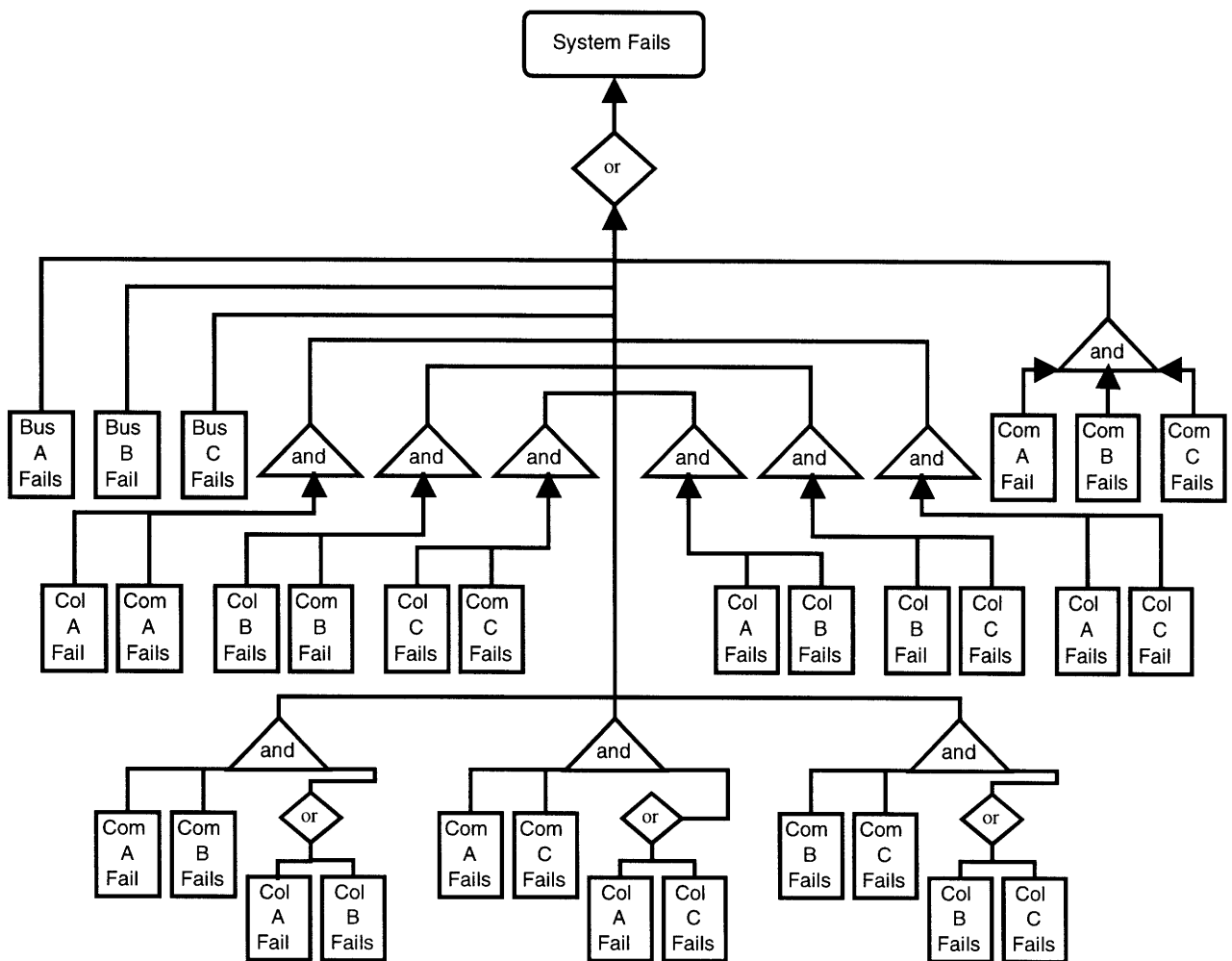


Figure 5.6: Fault Tree for the Three Spacecraft SSI MAMSC Architecture

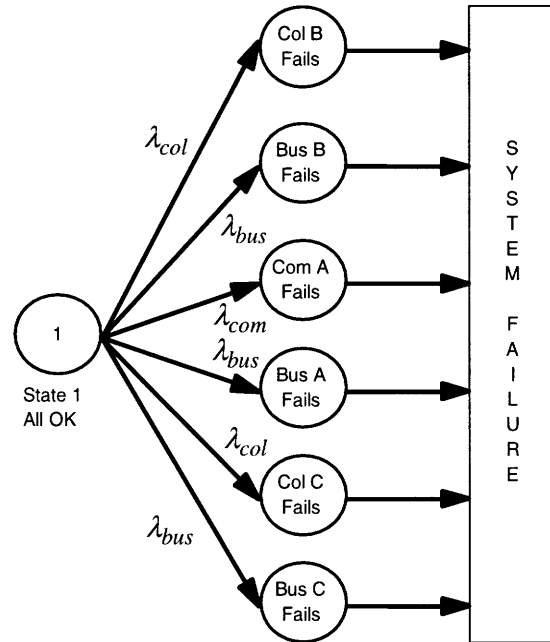


Figure 5.7: Markov Model for the 3 Spacecraft SSI SFD Architecture

From the fault trees, a Markov model illustrating each possible state of the system may be created for each architecture. Figure 5.7 illustrates the Markov model for the SFD architecture. This model contains only one possible functioning state, which occurs when all six components are working. Otherwise, the system is in a state of failure - no fringes can be measured, no images can be produced, and the capability requirements can no longer be met. On the other hand, the Markov model for the MAMSC design was considerably more complicated with 43 mutually exclusive states. Because the MAMSC Markov model is so large, it is not visually represented here as it would require several pages to portray.

From the Markov model diagrams, a system of differential equations can be written to determine the probability of the system being in any given state at any given time. This is done by representing each possible state of the system in the Markov model as a node in a network. To determine the differential equation for a particular state, simply balance the flow into and out of the node representing that state. For example, the Markov model (Figure 5.7) for the SFD architecture contains only one functioning state node. This node has no inflowing arcs, but has six outflowing arcs. Thus the system may be fully described with only one linear first order differential equation.

$$\dot{P}_1 = -(\lambda_{com} + 2\lambda_{col} + 3\lambda_{bus})P_1 \quad (5.14)$$

where \dot{P}_1 is the time rate of change of the probability of the system being in State 1, P_1 is the probability of being in State 1, λ_{com} is the failure rate of a combiner, λ_{col} is the failure rate of a collector, and λ_{bus} is the failure rate of a bus. Solving this differential equation yields the probability that the three-spacecraft SFD architecture is able to function and satisfy its mission requirements at any desired time.

More complicated architectures require multiple differential equations to fully describe the system and can be represented in matrix form.

$$\dot{\vec{P}} = A\vec{P} \quad (5.15)$$

where $\dot{\vec{P}}$ is the time rate of change of the state probability vector, A is the state coefficient matrix comprised of component failure rates, and \vec{P} is the state probability vector.

The three-spacecraft MAMSC architecture requires a set of 43 partially coupled linear first order differential equations to model the system. Because a 43x43 matrix will not fit on a page, each differential equation is written out individually here.

$$\dot{P}_1 = -(3\lambda_{bus} + 3\lambda_{com} + 3\lambda_{col})P_1 \quad (5.16)$$

$$\dot{P}_2 = \lambda_{col}P_1 - (3\lambda_{bus} + 3\lambda_{com} + 2\lambda_{col})P_2 \quad (5.17)$$

$$\dot{P}_3 = \lambda_{com}P_2 - (3\lambda_{bus} + 2\lambda_{com} + 2\lambda_{col})P_3 \quad (5.18)$$

$$\dot{P}_4 = \lambda_{com}P_3 - (3\lambda_{bus} + \lambda_{com} + 2\lambda_{col})P_4 \quad (5.19)$$

$$\dot{P}_5 = \lambda_{com}P_2 - (3\lambda_{bus} + 2\lambda_{com} + 2\lambda_{col})P_5 \quad (5.20)$$

$$\dot{P}_6 = \lambda_{com}P_5 - (3\lambda_{bus} + \lambda_{com} + 2\lambda_{col})P_6 \quad (5.21)$$

$$\dot{P}_7 = \lambda_{col}P_1 - (3\lambda_{bus} + 3\lambda_{com} + 2\lambda_{col})P_7 \quad (5.22)$$

$$\dot{P}_8 = \lambda_{com} P_7 - (3\lambda_{bus} + 2\lambda_{com} + 2\lambda_{col}) P_8 \quad (5.23)$$

$$\dot{P}_9 = \lambda_{com} P_8 - (3\lambda_{bus} + \lambda_{com} + 2\lambda_{col}) P_9 \quad (5.24)$$

$$\dot{P}_{10} = \lambda_{com} P_7 - (3\lambda_{bus} + 2\lambda_{com} + 2\lambda_{col}) P_{10} \quad (5.25)$$

$$\dot{P}_{11} = \lambda_{com} P_{10} - (3\lambda_{bus} + \lambda_{com} + 2\lambda_{col}) P_{11} \quad (5.26)$$

$$\dot{P}_{12} = \lambda_{col} P_1 - (3\lambda_{bus} + 3\lambda_{com} + 2\lambda_{col}) P_{12} \quad (5.27)$$

$$\dot{P}_{13} = \lambda_{com} P_{12} - (3\lambda_{bus} + 2\lambda_{com} + 2\lambda_{col}) P_{13} \quad (5.28)$$

$$\dot{P}_{14} = \lambda_{com} P_{14} - (3\lambda_{bus} + \lambda_{com} + 2\lambda_{col}) P_{14} \quad (5.29)$$

$$\dot{P}_{15} = \lambda_{com} P_{12} - (3\lambda_{bus} + 2\lambda_{com} + 2\lambda_{col}) P_{15} \quad (5.30)$$

$$\dot{P}_{16} = \lambda_{com} P_{15} - (3\lambda_{bus} + \lambda_{com} + 2\lambda_{col}) P_{16} \quad (5.31)$$

$$\dot{P}_{17} = \lambda_{com} P_1 - (3\lambda_{bus} + 2\lambda_{com} + 3\lambda_{col}) P_{17} \quad (5.32)$$

$$\dot{P}_{18} = \lambda_{com} P_{17} - (3\lambda_{bus} + \lambda_{com} + 3\lambda_{col}) P_{18} \quad (5.33)$$

$$\dot{P}_{19} = \lambda_{col} P_{18} - (3\lambda_{bus} + \lambda_{com} + 2\lambda_{col}) P_{19} \quad (5.34)$$

$$\dot{P}_{20} = \lambda_{com} P_{17} - (3\lambda_{bus} + \lambda_{com} + 3\lambda_{col}) P_{20} \quad (5.35)$$

$$\dot{P}_{21} = \lambda_{col} P_{20} - (3\lambda_{bus} + \lambda_{com} + 2\lambda_{col}) P_{21} \quad (5.36)$$

$$\dot{P}_{22} = \lambda_{col} P_{17} - (3\lambda_{bus} + 2\lambda_{com} + 2\lambda_{col}) P_{22} \quad (5.37)$$

$$\dot{P}_{23} = \lambda_{com} P_{22} - (3\lambda_{bus} + \lambda_{com} + 2\lambda_{col}) P_{23} \quad (5.38)$$

$$\dot{P}_{24} = \lambda_{col} P_{17} - (3\lambda_{bus} + 2\lambda_{com} + 2\lambda_{col}) P_{24} \quad (5.39)$$

$$\dot{P}_{25} = \lambda_{com} P_{24} - (3\lambda_{bus} + \lambda_{com} + 2\lambda_{col}) P_{25} \quad (5.40)$$

$$\dot{P}_{26} = \lambda_{com} P_1 - (3\lambda_{bus} + 2\lambda_{com} + 3\lambda_{col}) P_{26} \quad (5.41)$$

$$\dot{P}_{27} = \lambda_{com} P_{26} - (3\lambda_{bus} + \lambda_{com} + 3\lambda_{col}) P_{27} \quad (5.42)$$

$$\dot{P}_{28} = \lambda_{col} P_{27} - (3\lambda_{bus} + \lambda_{com} + 2\lambda_{col}) P_{28} \quad (5.43)$$

$$\dot{P}_{29} = \lambda_{com} P_{26} - (3\lambda_{bus} + \lambda_{com} + 3\lambda_{col}) P_{29} \quad (5.44)$$

$$\dot{P}_{30} = \lambda_{col} P_{29} - (3\lambda_{bus} + \lambda_{com} + 2\lambda_{col}) P_{30} \quad (5.45)$$

$$\dot{P}_{31} = \lambda_{col} P_{26} - (3\lambda_{bus} + 2\lambda_{com} + 2\lambda_{col}) P_{31} \quad (5.46)$$

$$\dot{P}_{32} = \lambda_{com} P_{31} - (3\lambda_{bus} + \lambda_{com} + 2\lambda_{col}) P_{32} \quad (5.47)$$

$$\dot{P}_{33} = \lambda_{col} P_{26} - (3\lambda_{bus} + 2\lambda_{com} + 2\lambda_{col}) P_{33} \quad (5.48)$$

$$\dot{P}_{34} = \lambda_{com} P_{33} - (3\lambda_{bus} + \lambda_{com} + 2\lambda_{col}) P_{34} \quad (5.49)$$

$$\dot{P}_{35} = \lambda_{com} P_1 - (3\lambda_{bus} + 2\lambda_{com} + 3\lambda_{col}) P_{35} \quad (5.50)$$

$$\dot{P}_{36} = \lambda_{com}P_{35} - (3\lambda_{bus} + \lambda_{com} + 3\lambda_{col})P_{36} \quad (5.51)$$

$$\dot{P}_{37} = \lambda_{col}P_{36} - (3\lambda_{bus} + \lambda_{com} + 2\lambda_{col})P_{37} \quad (5.52)$$

$$\dot{P}_{38} = \lambda_{com}P_{35} - (3\lambda_{bus} + \lambda_{com} + 3\lambda_{col})P_{38} \quad (5.53)$$

$$\dot{P}_{39} = \lambda_{col}P_{38} - (3\lambda_{bus} + \lambda_{com} + 2\lambda_{col})P_{39} \quad (5.54)$$

$$\dot{P}_{40} = \lambda_{col}P_{35} - (3\lambda_{bus} + 2\lambda_{com} + 2\lambda_{col})P_{40} \quad (5.55)$$

$$\dot{P}_{41} = \lambda_{com}P_{40} - (3\lambda_{bus} + \lambda_{com} + 2\lambda_{col})P_{41} \quad (5.56)$$

$$\dot{P}_{42} = \lambda_{col}P_{35} - (3\lambda_{bus} + 2\lambda_{com} + 2\lambda_{col})P_{42} \quad (5.57)$$

$$\dot{P}_{43} = \lambda_{com}P_{42} - (3\lambda_{bus} + \lambda_{com} + 2\lambda_{col})P_{43} \quad (5.58)$$

Upon solving this system of equations for the MAMSC architecture, the model may be simplified from 43 states to the functioning 6 states listed in Table 5.1. These are the six states in which the interferometer may still produce an image. This process of reducing the number of states in a Markov model is known as system aggregation. Aggregation can be exploited because there are multiple ways in which a certain kind of failure can occur. For example, the failure of any one of the three collectors will transition the system from State 1 to State 2. It is important to know that the system is now in State 2, but knowledge of which one of the three

Table 5.1: Aggregated Functioning States for the MAMSC Model

| State # | Functioning State |
|---------|--|
| 1 | Everything is working. |
| 2 | One collector has failed. |
| 3 | One combiner has failed. |
| 4 | Two combiners have failed. |
| 5 | One collector and one combiner have failed. |
| 6 | One collector and two combiners have failed. |

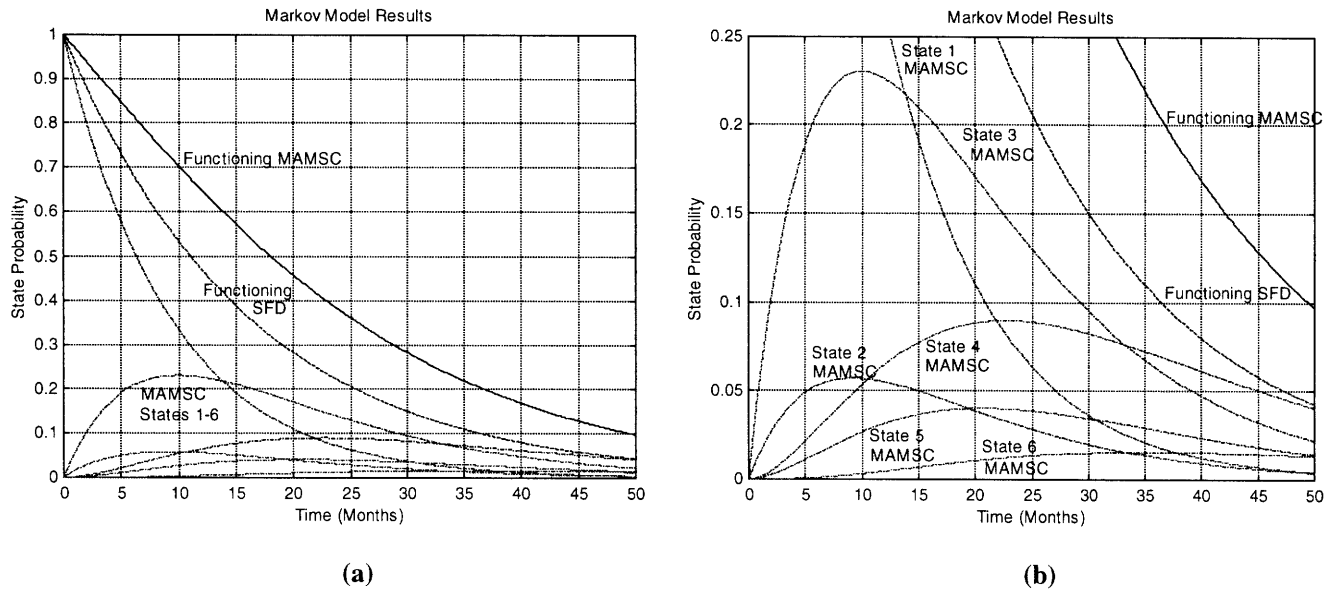


Figure 5.8: Markov Model Results for the 3 Spacecraft SFD and MAMSC Architectures (a) and the Results Magnified (b)

collectors failed is not important because it doesn't impact how the system functions in the degraded state. Therefore these three states are aggregated into one, thereby reducing the order of the model.

Figure 5.8 illustrates the results obtained after solving the systems of differential equations for the SFD and MAMSC three-spacecraft architectures. As was the case in the previous section, failure rates of $0.01042 \text{ month}^{-1}$ for the satellite bus, $0.005555 \text{ month}^{-1}$ for the collector payload, and $0.02083 \text{ month}^{-1}$ for the combiner payload were assumed. From the plots in Figure 5.8, one can see that the MAMSC design always has a greater probability of functioning than the SFD design. The likelihood of success remains above 50% for only 11 months in the SFD architecture and 18 months in the MAMSC architecture. Additionally, by viewing the aggregated states of the MAMSC architecture, we see which states, fully functioning (State 1) or degraded (States 2-6), the system is most likely to be functioning in at a given time. For example, Figure 5.5b illustrates that the MAMSC system transitions from state 1 to state 3 after approximately 13 months.

If we know the utility of operating in each of the six aggregated states, then we can use the results of the Markov model to predict the total utility of the mission. For example, let C_i represent the imaging rate in states 1 through 6. Then the total expected ($E(T)$) number of images at time T is

$$E(T) = \int_0^T \sum_{i=1}^6 C_i P_i(t) dt \quad (5.59)$$

where $P_i(t)$ is the probability that the system is functioning in state i at time t . Thus, Markov models can be utilized not only to tell us *if* a particular system meets its requirements, but also *how well* the system meets its requirements as a function of time. This latter information can then be used to predict the total utility of the system as a function of time.

5.4 Reliability Model Summary

In this Chapter, we have developed two models to simulate and predict the reliability of an SSI. The first model is a combinatorial model that allows us to determine the probability that an architecture meets the capability requirements at a specific time as a function of the number of collector, combiner, and MAMSC spacecraft in the array. This model shows us that the MAMSC architecture will always be more reliable than an SFD architecture with an identical number of spacecraft. The second model is a Markov model that allows us to determine the probability as a function of time that a complex system is still operating, although with reduced mission effectiveness, after failures of individual components within the system. This reliability model can now be coupled with the capability model in Chapter 4 to predict the *total performance* (targets imaged) over the mission life as a function of the system architecture. Both of the reliability models developed in this chapter are important system architecture design tools that will be used to compute the cost per function metric for different SSI architectures in Chapter 7.

Chapter 6

Cost Model

“It costs a lot to build bad products.”

- Norman Augustine

Aerospace engineering has historically been a performance-based endeavor as governments were willing to spend whatever it took to get the job done. With the end of the Cold War, however, cost became a more important issue as governments were no longer able to justify spending unlimited sums of money on space technologies. Now, cost drives the design of most modern space systems and is usually the determining factor in whether or not a program will succeed [Wertz et al, 1996]. In today’s market, the best system is the one that provides the best value in meeting the capability requirements. This is the rationale behind the Distributed Satellite System (DSS) cost per function metric (CPF), which serves as a quantitative basis for comparing different space system architectures [Shaw, 1998]. Computation of this metric for a separated spacecraft interferometer (SSI) requires a lifecycle cost model.

Figure 6.1 illustrates all of the costs generally taken into account when determining the lifecycle cost of a Distributed Satellite System. The three primary cost categories are the development of the spacecraft payloads and buses, deployment (launch) of the system, and the operation of the system. Secondary cost trades appear within the intersections of these primary categories. For example, adding autonomy to the system lowers operations costs by increasing design costs. Distributing payloads on multiple, identical satellites reduces design costs at the expense of launch costs, while increasing the multifunctionality of the satellites does the reverse. Furthermore, distribution reduces failure compensation costs by allowing for the replacement of only the components within the system that have failed. Finally, spending more money on launch at the beginning of a commercial program to create an early revenue stream can increase the total net present value and internal rate of return on the project due to the time value of money. For this study, which focuses on a non-commercial scientific mission, only the design/construction, launch, and operations costs are modeled.

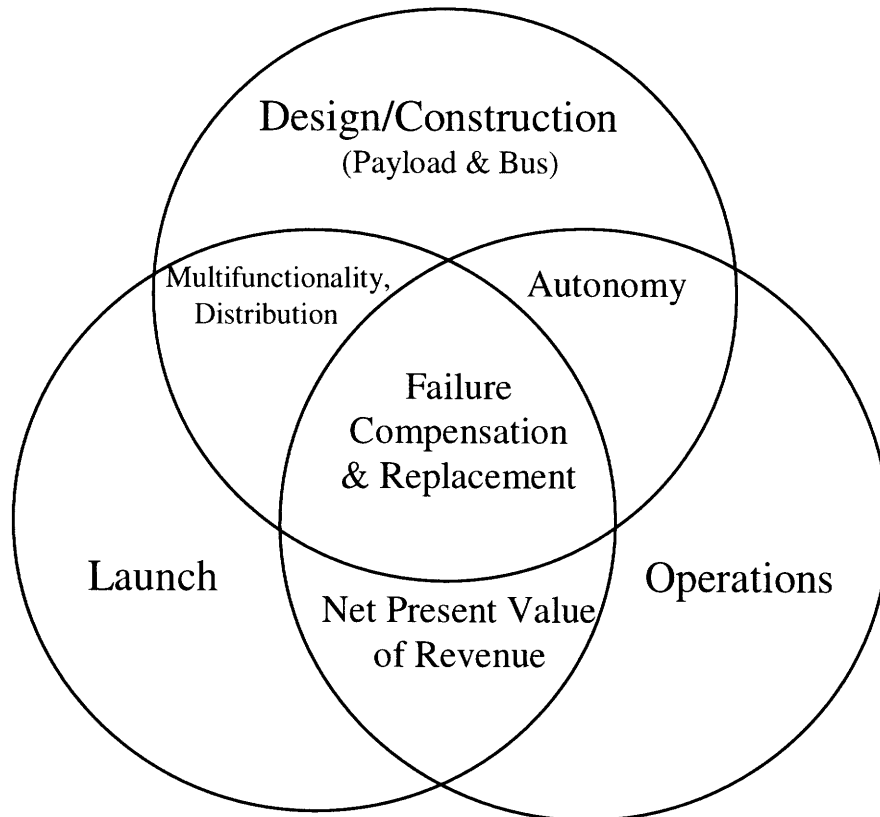


Figure 6.1: DSS Lifecycle Costs

This chapter outlines the development of the cost model. The first section of this chapter provides a summary of current space system cost modeling techniques and an overview of the SSI cost model. Each of the four components of the SSI cost model – payload, spacecraft bus, system launch, and mission operations – are then discussed in detail. Finally, a summary of the cost model is provided within the context of the SSI architecture design and optimization. It should be stressed that cost estimates early in the design process are very approximate. Accordingly, the lifecycle cost model presented in this chapter should be viewed as a tool for making relative cost comparisons between architectures and *not* as a tool to compute absolute costs for program budgeting.

6.1 Background

Cost is an engineering parameter that varies with the physical parameters of a system. Accordingly, the space systems community has developed several tools to analyze and predict project costs. Most of these tools use parametric models to mathematically relate system cost to the physical, technical, and performance parameters of the system.

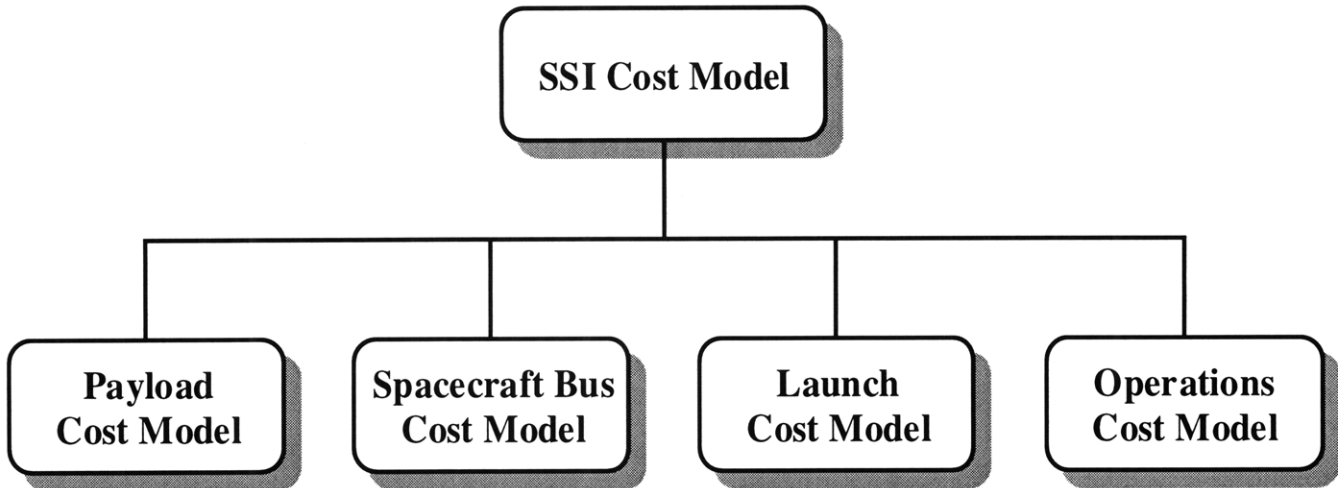


Figure 6.2: Structure of the SSI Cost Model

$$Cost_{SSI} = Cost_{Payload} + Cost_{s/c_Bus} + Cost_{Launch} + Cost_{Operations} \quad (6.1)$$

The SSI cost model is divided into four parts as illustrated in Figure 6.2 and Equation 6.1. The payload cost is the cost of all the collector and combiner optics in the array, and is a function of the collector aperture diameter, combiner complexity, number of spacecraft, and learning curve savings. The bus cost is the total cost of all of the satellite buses in the SSI. It includes design, manufacturing, integration, and testing costs as well as learning curve savings. The launch cost model is strictly a function of the total mass of the system and the launch vehicles used to deploy the system. Finally, the operations cost is the total cost to maintain and operate the SSI once the array has been deployed, and is a function of the number of spacecraft in the array, the reliability of each spacecraft, and the mission duration. By combining these four component costs, the total cost of the system may be estimated.

6.2 Payload Cost Model

More than any other component, the payload of a satellite determines the satellite’s final design, mass, and cost. Both total satellite power and mass usually scale as a fraction of the payload power and mass. The cost of a spacecraft bus scales directly with these two parameters. Additionally, launch costs scale nonlinearly with system mass. Thus, a large payload has a cascading effect on the total system cost.

Unfortunately, no historical cost databases exist for space-qualified interferometer optics as an interferometer has never flown in space. For this reason, there are no documented Cost

Estimating Relationships (CERs) for determining collector and combiner visible spectrum interferometer costs. The payload costs used in this thesis come from a DS3 costing workshop held by NASA in March 1997. Based on bids from various companies, the attendees of the workshop concluded that a single twelve centimeter aperture space-qualified interferometer collector will cost \$8.45 million and a space-qualified combiner for a two (12 cm aperture) collector interferometer will cost \$16.9 million.

6.3 Spacecraft Bus Cost Model

The spacecraft bus cost model estimates the total cost involved in designing, manufacturing, integrating, and testing each spacecraft bus. This cost will generally be proportional to the mass, power, and other subsystem requirements of the spacecraft. Over the years, several governmental organizations have created Cost Estimation Relationships (CERs) for satellite buses that show how the cost properties of a spacecraft bus vary with the subsystem parameters of the bus. These CERs are based on the historical data of past satellite programs and work on the assumption that future costs will reflect historical trends.

The two most commonly used CERs are the U.S. Air Force's Unmanned Spacecraft Cost Model (USCM) and the Aerospace Corporation's Small Satellite Cost Model (SSCM). The SSCM is valid for satellites approximately 500 kg or less and is based on 1990's technology. The USCM database contains much larger satellites, but is based on older 1970's and 1980's technology [Bearden, 1998]. Since SSI spacecraft are estimated to weigh less than 500 kg, the SSI satellite bus cost model outlined in this chapter uses the SSCM.

Over twenty separate CERs exist in the SSCM. Tables 6.1 and 6.2 list the CERs specifically selected for the SSI spacecraft bus cost model from SSCM versions 7.4 and 8.0. Each table lists the independent variable(s) in the CER, the applicable range of the independent variable as an input, the CER itself, and the standard error. The dependent variable C in each CER is the total cost of the spacecraft bus in millions of U.S. dollars. In SSCM Version 7.4, the standard error (σ) of the CER is an absolute value, while in SSCM Version 8.0 the standard error of the CER is expressed as a percentage of the CER value itself.

While any of these CERs may be used separately to obtain an independent estimate of the SSI combiner or collector bus cost, it is generally more effective to use several CERs

Table 6.1: Selected SSCM Cost Estimating Relationships - Version 7.4 [Bearden, 1996]

| Independent Variable (x) | Applicable Range | CER for Total Bus Cost (FY94\$M) | Standard Error (σ) (FY94\$M) |
|------------------------------------|------------------|----------------------------------|---------------------------------------|
| S/C Bus Dry mass (kg) | 20-400 | $C=0.704+0.0235x^{1.261}$ | 3.33 |
| Power System Mass (kg) | 7-70 | $C=-3.58+1.53x^{0.702}$ | 3.52 |
| Structures Mass (kg) | 5-100 | $C=1.47+0.07x\ln(x)$ | 5.40 |
| Number of Thrusters | 1-8 | $C=46.16-41.86x^{-0.5}$ | 8.95 |
| Pointing Accuracy (deg) | 0.25-12 | $C=1.67+12.98x^{-0.5}$ | 7.37 |
| Pointing Knowledge (deg) | 0.1-3 | $C=12.94-6.681x\ln(x)$ | 8.79 |
| BOL Power (W) | 20-480 | $C=-22.62+17.9x^{0.15}$ | 6.13 |
| Average Power (W) | 5-10 | $C=-8.23+8.14x^{0.22}$ | 5.71 |
| EOL Power (W) | 5-440 | $C=0.507+1.55x^{0.452}$ | 6.20 |
| Solar Array Area (m ²) | 1-1000 | $C=26.0-21.86x^{-0.23}$ | 6.37 |

Table 6.2: Selected SSCM Cost Estimating Relationships - Version 8.0 [Bearden, 1996]

| Independent Variables x and z | Applicable Range | CER for Total Bus Cost (FY94\$M) | Standard Error (σ) (%) |
|--|---------------------------------|-------------------------------------|---------------------------------|
| x: EOL Power (W) z: Pointing Accuracy (deg) | 5-500 0.05-5 | $C=6.47x^{0.1599}z^{-0.356}$ | 29.55 |
| x: Downlink Data Rate (kbps) z: Average Power (W) w: Propulsion System Dry Mass (kg) | 1-2000 5-410 1-35 | $C=1.44x^{0.0107}z^{0.509}1.0096^w$ | 35.66 |
| x: Spacecraft Dry Mass (kg) z: Pointing Accuracy (deg) | 20-400 0.05-5 | $C=0.6416x^{0.661}-1.5117z^{0.289}$ | 37.19 |
| x: Solar Array Area (m ²) y: ACS Type (3-axis or other) | 0.3-11 0: other 1: 3-axis | $C=4.291x^{0.255}1.989^z$ | 38.53 |
| x: Power Subsystem Mass (kg) | 7-70 | $C=0.602x^{0.839}$ | 37.07 |

simultaneously to reduce the effect of statistical outliers in the historical database of satellites [Bearden, 1996]. To estimate the spacecraft bus cost from multiple CERs, a weighted average algorithm is employed using the standard error of each CER to establish the appropriate weighting factor.

$$Cost_{s/c_bus} = \frac{\sum \frac{C_i}{\sigma_i^2}}{\sum \frac{1}{\sigma_i^2}} \quad (6.2)$$

where $Cost_{s/c_bus}$ is the theoretical first unit cost of the spacecraft bus, C_i is the i^{th} cost estimate, and σ_i is the i^{th} standard error.

6.4 Learning Curve

CERs predict the Theoretical First Unit (TFU) cost of a satellite bus, including all of the design work that takes place before the actual construction of the bus. However, CERs poorly estimate the costs for even the most modest production lines [Wong, 1992]. To take into account the fact that multiple payloads and spacecraft buses will be built, we will apply a *learning curve* to the TFU bus costs estimated from the CERs and the payload costs from the DS3 cost workshop. A learning curve is a mathematical technique that accounts for productivity improvements as larger numbers of units are produced. Factors which account for the cost reductions in a learning curve include economies of scale, design time, set up time, tooling cost amortization, bulk component procurements, and human learning [Wong, 1992]. Using the learning curve, the total production cost for N units, in this case collector or combiner buses, is

$$Cost_{production} = TFU \times L \quad (6.3)$$

$$L = N^B \quad (6.4)$$

$$B = 1 - \frac{\ln((100\%) / S)}{\ln 2} \quad (6.5)$$

where L is the learning curve factor and S is the learning curve slope in percent. In the aerospace industry, S varies between 85%-96%. Table 6.3 lists which values of S that Robert Wong, Manager of Economic Analysis in the Systems Engineering Division of TRW, recommends as a function of production quantity. These same values of S were applied to the learning curve calculations in the SSI cost model. After executing equations 6.3 through 6.5, the final per spacecraft bus costs can be calculated.

$$Cost_{per_unit} = \frac{Cost_{production}}{N} \quad (6.6)$$

Table 6.3: Learning Curve Slopes as a Function of Production Quantity in the Aerospace Industry

| # Units Produced | Recommended S |
|------------------|---------------|
| <10 | 95% |
| 10-50 | 90% |
| >50 | 85% |

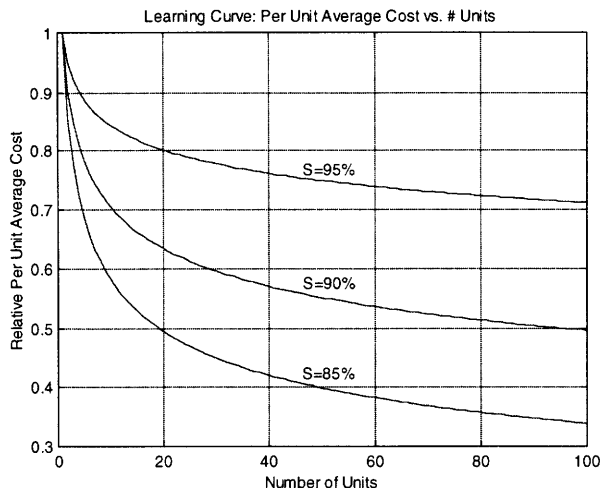


Figure 6.3: Per Unit Average Cost as a Function of Units Produced for Different Learning Curve Slopes

Figure 6.3 illustrates the effects of various learning curves on the per unit average costs. As one can see, the relative per unit average cost decreases as the number of units produced increases.

6.5 Launch Cost Model

Launch costs have been identified as the single most important factor holding back the scientific exploration and commercial development of space [NASA, 1996]. Today, it costs approximately \$10,000 to place one kg of payload into low Earth orbit. The U.S. government is currently trying to decrease the cost of access to space through several initiatives, including the Air Force’s Evolved Expendable Launch Vehicle (EELV) program and NASA’s Reusable Launch Vehicle (RLV) program. Additionally, many new start-up companies are trying to build their own low-cost launch vehicles with the hope of capturing the envisioned market for cheap access to space.

Selection of a launch vehicle for a payload depends on several factors, not all of which are technical. These factors include cost, performance, reliability, and politics. Currently, U.S. policy mandates that all government payloads must be launched on U.S. launch vehicles. Since development and deployment of an SSI will likely be a government initiative managed by NASA, rather than a private endeavor, this constraint restricts the pool of potential launch vehicles to American rockets. NASA currently prefers to use the Delta II launch vehicle for scientific satellite launches. For this reason, the SSI launch cost model only considers the three models of the Delta II rocket. Table 6.4 lists the capabilities of each of these three models along with the cost per kilogram to deploy a payload into a halo orbit about the Earth-Sun system’s

Table 6.4: Delta II Performance Characteristics to L2 [Boeing, 1997]

| Delta II Model | Payload* (kg) | Cost (\$M) | \$/kg |
|----------------|---------------|------------|--------|
| 7325 | 687 | 44 | 64,047 |
| 7425 | 789 | 46 | 58,302 |
| 7925 | 1261 | 56 | 44,409 |

*To an L2 halo orbit with a 10 m fairing.

second Lagrange point (L2). Such a halo orbit is a strong candidate for future SSI missions.

The goal is to select a set of launch vehicles to deploy all of the spacecraft in the SSI such that total launch costs are minimized. While linear programming is tailor-made to solve such optimization programs, it cannot be used in this case because it would lead to fractional answers. Because one cannot launch a fractional number of rockets, the solution to the optimization problem must be constrained to be integral. This field of mathematics is known as integer programming. In this case, because we have only three variables from which to choose – the number of Delta II 7325’s, 7425’s, and 7925’s – a straightforward optimization algorithm may be implemented to select a set of Delta II rockets such that the total launch cost is minimized.

Figure 6.4 illustrates ideally how the total launch cost scales with the total mass of the SSI. Notice the stair-step shape of the curve. This shape is due to the fact that more mass may be added at zero cost to the last rocket in the queue until its capacity is exceeded, at which time a new rocket and its associated cost must be added. It should be noted that the actual number of Delta II rockets required to deploy the SSI will depend not only on the total mass of the SSI, but also on the volumetric dimensions of each collector or combiner spacecraft, which could in turn place an upper bound on the total number of spacecraft that can fit in a single payload fairing. Thus, the total cost to deploy a given sized array could be more than illustrated in Figure 6.4.

The total cost required to launch and deploy an SSI can now be represented as

$$Cost_{Launch} = (\$44M)n_{7325} + (\$46M)n_{7425} + (\$56M)n_{7925} \quad (6.7)$$

where n_{73xx} is the number of each Delta II model required as determined by the optimization algorithm for an SSI with a given total mass.

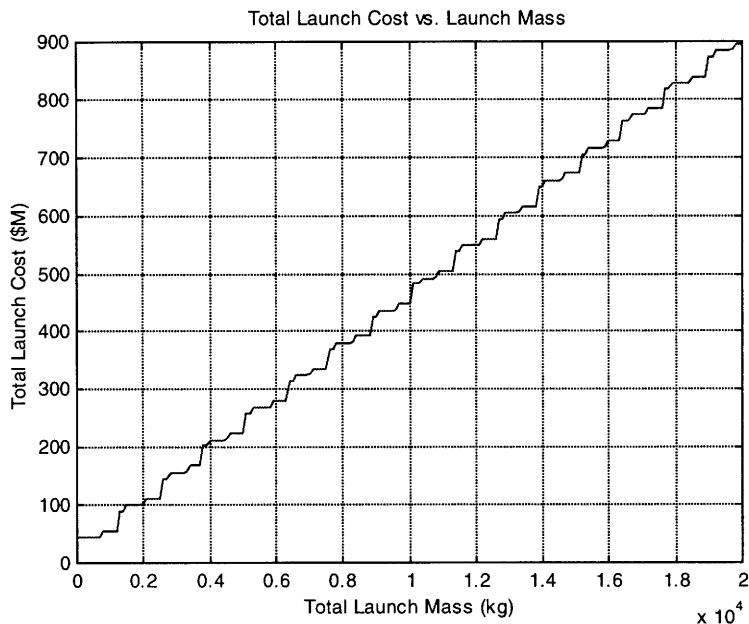


Figure 6.4: Total Launch Cost as a Function of Total SSI Mass

6.6 Operations Cost Model

Mission operations costs are the costs associated with command and control of an SSI. This includes health monitoring, housekeeping, navigation, imaging, tracking via the NASA Deep Space Network (DSN), and data collection. In a DS3 costing workshop in March of 1997, the NASA Jet Propulsion Laboratory estimated that 3 hours of tracking time through the 11m radio telescopes of the Deep Space Network would be required daily to maintain DS3. Over a mission life of six months, this would cost \$4.2 million, or \$700,000 per month [DS3, 1997]. If we assume a linear model for the relationship between the number of spacecraft in an SSI and the operations cost required to maintain an SSI, the monthly operations cost per spacecraft is \$233,000. The total cost to maintain an n spacecraft SSI is then

$$Cost_{operations_month} = (\$233,000)n \tag{6.8}$$

where n corresponds to the total number of functioning spacecraft in the SSI at a particular time.

Equation 6.8 fails to take into account the possible failures that can take place within an SSI array over its operational lifetime. To take into account the likely failures that will occur within the array during its mission, the Markov model developed in Chapter 5 is utilized. By multiplying equation 6.8 for each possible functioning state of the system by the probability that

the system is functioning in that state (obtained from the Markov model) and then integrating over the desired mission life (T), the total operations cost can be calculated.

$$Cost_{Operations} = \int_0^T \sum_{i=3}^n C_i P_i(t) dt \quad (6.9)$$

C_i is the monthly operations cost of an SSI with i spacecraft from Equation 6.8.

6.7 Cost Model Summary

Now that we have fully developed the cost model, we can estimate the total cost of an SSI with any given number of collector and combiner spacecraft. While the cost estimates do carry a degree of uncertainty, they give us a quantifiable means by which we may compare different architectures. The uncertainties will be addressed by an uncertainty analysis in Chapter 7. In Chapters 4, 5, and 6 we have completed the capability, reliability, and cost models for an SSI. In the next chapter, we link these models together to calculate the DSS GINA metrics and evaluate different system architectures.

Chapter 7

System Architecture Results

“Without analysis, no synthesis.”

- Friedrich Engels

In the preceding three chapters, we developed the capability, reliability, and cost models to evaluate and compare the performance and cost of different separated spacecraft interferometer (SSI) architectures for a future visible spectrum SSI. This chapter presents the results for each architecture on the basis of the model outputs and the cost per function metric. First, the different SSI architectures that were analyzed are introduced. The DSS GINA systems engineering and architecting (SE&A) process as applied to the SSI case study is then outlined in detail. Next, the model outputs for each architecture are shown and compared. Finally, uncertainty and sensitivity analyses are carried out to assess the elasticity of the results. Analyzing these results yields non-intuitive insight into the SSI design architecture trade space that can be used to improve the design of future separated spacecraft interferometers.

7.1 Architectures Analyzed

Eleven separate architectures were analyzed. Every spacecraft was modeled as a combination of a satellite bus, combiner payload(s), and/or collector payload(s). Possible spacecraft types that could be placed in each architecture included SFD combiner and collector spacecraft with no internal redundancy (no backup payloads), SFD combiner and collector spacecraft with internal redundancy (backup payloads), and MAMSC spacecraft with both combiner and collector payloads (no backup payloads).

Figure 7.1 illustrates in diagram form the eleven architectures analyzed. Each design can be identified by the following five digit code:

- Digit 1: Total number of spacecraft in the array.
- Digit 2: Number of SFD spacecraft in the array.
- Digit 3: Number of MAMSC in the array.
- Digit 4: Number of combiner payloads in the array.
- Digit 5: Number of collector payloads in the array.

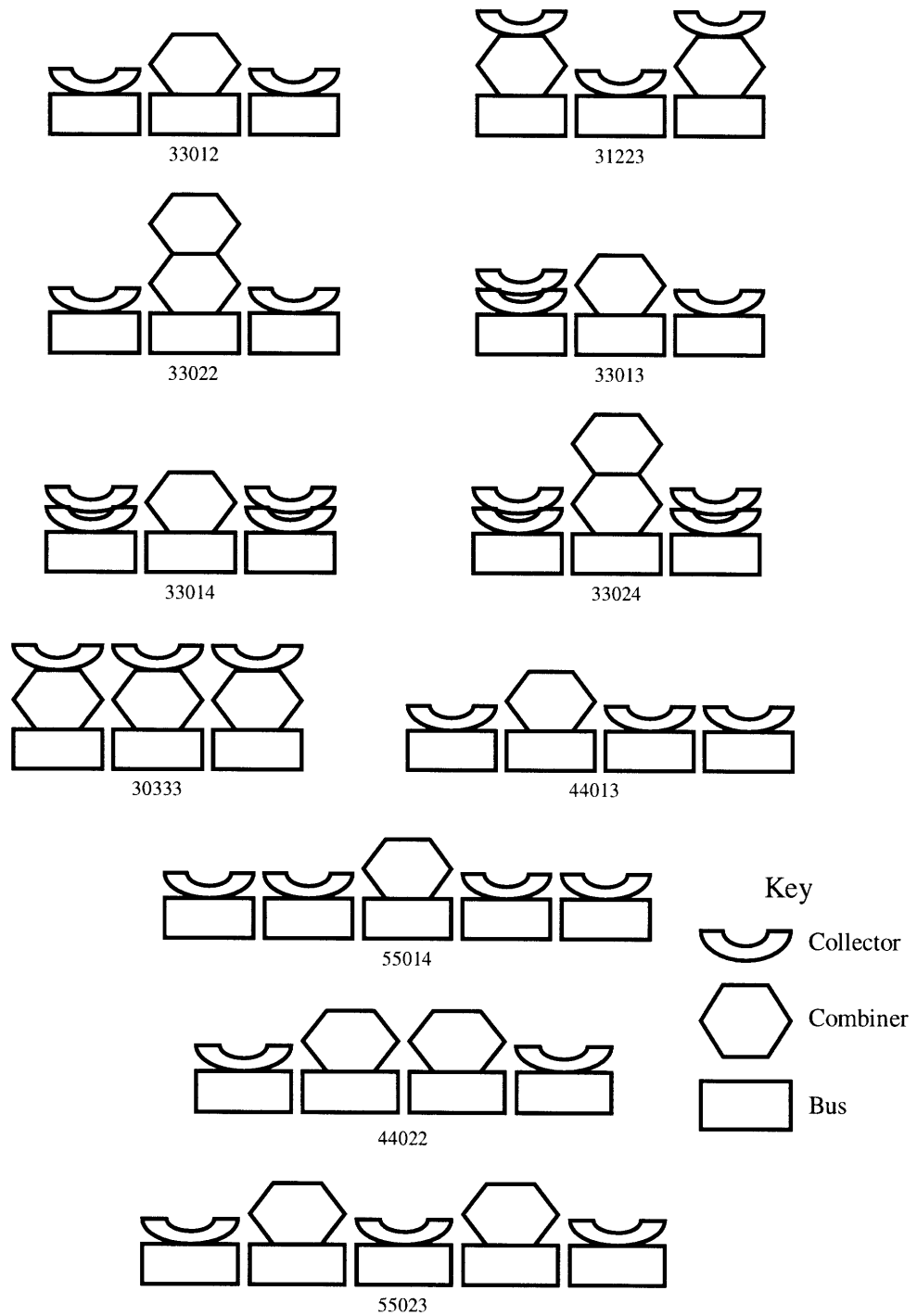


Figure 7.1: SSI Architectures Analyzed

For example, the sequence 33012 identifies a three-spacecraft SFD array with one combiner spacecraft and two collector spacecraft. In the diagrams, a rectangle denotes a spacecraft bus, a hexagon denotes a combiner, and a curved plate denotes a collector. All possible three-spacecraft SFD, MAMSC, and hybrid architectures were analyzed allowing a maximum of two payloads per spacecraft. Only a subset of the possible four and five spacecraft architectures were analyzed due to the growing size of the Markov models for these architectures.

7.2 System Architecture Design and Optimization Process

This section summarizes the implementation of the DSS GINA SE&A process to the SSI mission. While each of the models have been described in the preceding chapters, how they are integrated into the system architecture optimization has not yet been laid out. The results presented in this chapter employ the model as described below. For a detailed explanation of the equations or parameters, refer to the indicated section or equation.

SSI Systems Engineering and Architecting Process:

1. Define system capability “Quality of Service” parameters (Section 3.2):
angular resolution (isolation), imaging rate (rate), mean square error (integrity).
2. Establish design variables, architecture parameters, and capability requirements (Table 7.1):
total number of spacecraft, number of SFD, number of MAMSC, number of redundant payloads, aperture diameter, combiner type, maximum baseline, geometric configuration, combiner payload mass, collector payload mass, payload power requirements, wavelength of observation, number of spatial frequencies (uv points) to be sampled, spacecraft bus propulsion system type and performance, velocity profile for reconfigurations, learning curve slope, component failure rates, intended mission life.
3. Calculate the mass of each spacecraft in the array:
use mass fractions from DS3 six week study workshop [DS3, 1997]
4. Calculate the acceleration of each spacecraft (Eqn. 4.12).
5. Calculate capability (Chapter 4):
number of simultaneous baselines available in a single configuration (Eqn. 4.1), number of u-v points sampled in a snapshot (Eqn. 4.2), number of configurations required for a single image (Eqn. 4.10), snapshot MSE (Eqn. 4.3), image MSE (Eqn. 4.3), time per image (Eqn. 4.27), maximum imaging rate (Eqn. 4.28), theoretical number of images over the intended mission life (Figure 4.12).
6. Create system Markov model (Section 5.3):
fault tree (Fig. 5.5), state diagram (Fig. 5.7), system of differential equations (Eqn. 5.15), state probabilities as a function of time (solution to Eqn. 5.15).
7. Calculate the expected total number of images over the intended mission life (Eqn. 5.59).
8. Calculate the total cost for all of the payloads (Section 6.2):

- combiner cost, collector cost, total payload costs with learning curve (Eqns. 6.3-6.5).
9. Calculate the total cost for all of the spacecraft buses (Section 6.3):
SFD combiner bus cost (Eqn. 6.2), SFD collector bus cost (Eqn. 6.2), MAMSC bus cost (Eqn. 6.2), total spacecraft bus costs with learning curve (Eqns. 6.3-6.5)
 10. Calculate the total launch cost (Section 6.5).
 11. Calculated the expected operations cost over the intended mission life (Section 6.6):
monthly operations cost (Eqn. 6.8), total operations cost (Eqn. 6.9)
 12. Calculate the total lifecycle cost (Section 6.1):
total SSI architecture cost (Eqn. 6.1)
 13. Evaluate the model outputs and cost per function for each architecture (Section 7.3)
reliability, capability, cost, cost per function.

Table 7.1 lists the nominal values for certain architecture parameters that were held constant for each design architecture. Changing these nominal values, as may be desired for future trade studies, may change the results obtained here.

Table 7.1: Architecture Parameters Held Constant Across All Architectures

| Design Variable | Nominal Value |
|-----------------------------------|-----------------------------|
| Aperture Diameter | 0.12 m |
| Combiner Mass | 58 kg |
| Collector Mass | 23 kg |
| Combiner Power | 135 W |
| Collector Power | 35 W |
| # uv Spatial Frequencies Sampled | 100 |
| Maximum Baseline | 1000 m |
| Geometric Configuration | Cornwell |
| Propulsion System Type | PPT |
| # PPTs per Translation Direction | 1 |
| Bus Failure Rate | 0.0104 month ⁻¹ |
| Combiner Failure Rate | 0.0208 month ⁻¹ |
| Collector Failure Rate | 0.00556 month ⁻¹ |
| Learning Curve Slope | 0.95 |
| Operations Cost per S/C per Month | \$233,000 |

7.3 Model Outputs and the Cost Per Function Metrics

This section shows how each SSI architecture rates on the basis of the model outputs and the cost per function (CPF) metric. First, each architecture is evaluated solely on the basis of each model output. Then the architectures are evaluated according to the CPF metric.

7.3.1 Reliability

Figure 7.2 illustrates the reliability (probability that the system can still measure an interference fringe and obtain an image with at least one baseline) of each system architecture at the end of one year. This is the output of the reliability model. The numbers are low because the failure rates assumed in the reliability model in Chapter 5 were on the high side due to the novelty of placing an interferometer in space. As expected, the three-spacecraft SFD architecture with no payload redundancy, 33012, has the lowest reliability. Three-spacecraft SFD architectures 33022, 33013, 33014, and 33024 all improve system reliability by providing some degree of internal payload redundancy. Notice that adding a single redundant combiner (33022) improves the total system reliability more than adding two redundant collectors (33014). The reason for this was explained in Section 5.2.

The most reliable three-spacecraft architectures are the MAMSC design (30333) and the fully redundant SFD design (33024). Total system reliability was maximized by architecture 55023 with the most total spacecraft and a redundant combiner spacecraft. This result implies that to maximize total system reliability, the SSI should have as many individual combiner and collector spacecraft as possible under the cost and complexity constraints. Also notice the substantial improvement in reliability from architecture 55014 to architecture 55023. This is again the result of the fact that, under our assumptions, the combiner has the lowest reliability and is thus the weak link in the design. Accordingly, providing a redundant combiner substantially improves the reliability of the system.

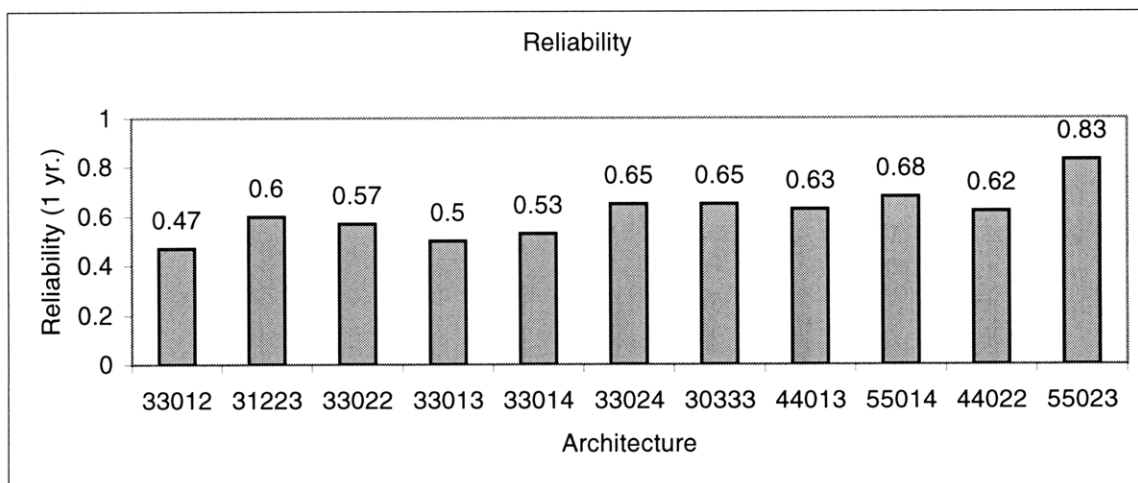


Figure 7.2: Reliability of the SSI Architectures

7.3.2 Performance

Figure 7.3 conveys the performance of each architecture in terms of the total expected number of images the system will produce in one year, taking into account failures. The performance was calculated by coupling the outputs from the capability and reliability models in the form of Equation 5.59. Two qualities boost system performance in an SSI – having more nonredundant baselines per array configuration and having a higher total system reliability. The first characteristic improves the system’s imaging rate and allows the SSI to take more images in a given amount of time. The second characteristic increases the probability that the system will be functioning at the end of its intended mission life, increasing the operational life over which the system may collect images. In other words, it allows the system to last longer in higher productivity states, and thus take more images.

Based on this reasoning, for an SSI with a fixed number of spacecraft, the array with MAMSC spacecraft should yield better performance than the same sized array with SFD spacecraft. This hypothesis holds true in Figure 7.3. The first seven architectures all contain three-spacecraft. The two architectures with MAMSC spacecraft, architectures 31223 and 30333, produce more images than any of the three-spacecraft SFD architectures. Architectures 33022, 33013, 33014, and 33024 all provide some degree of internal payload redundancy for one or more of the SFD spacecraft in that architecture. This redundancy increases the reliability of these three-spacecraft SFD architectures over the three-spacecraft SFD with no redundancy (33012), so that they essentially last longer and thus can produce more images as explained in the previous paragraph. However, the total number of images produced by these SFD

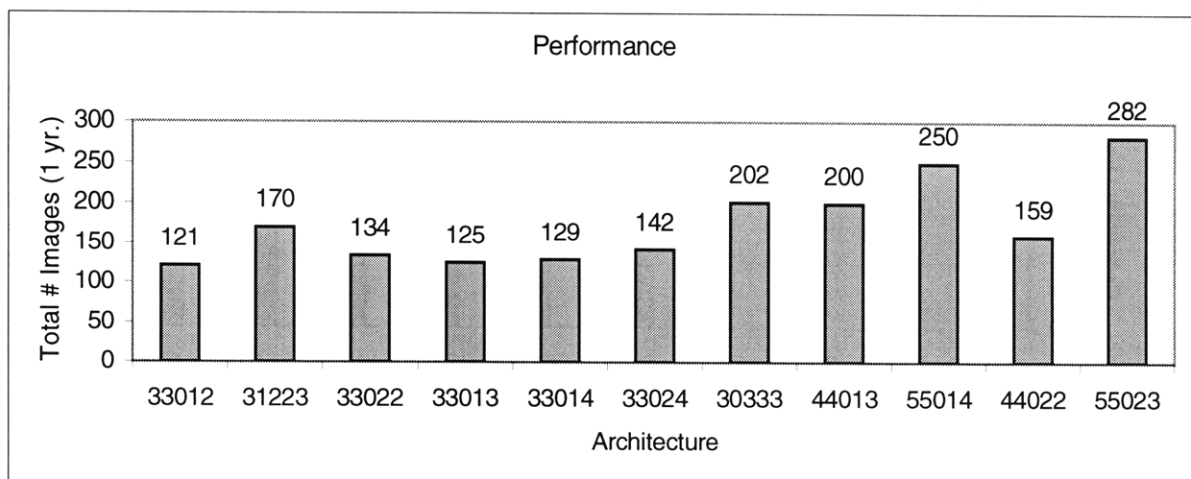


Figure 7.3: Performance of the SSI Architectures

architectures with internal redundancy still pales in comparison with the performance of the two MAMSC architectures. This is because both MAMSC architectures provide more than one instantaneous baseline for sampling the u-v plane per array configuration, while the SFD architectures provide only one instantaneous baseline. With more instantaneous baselines available per configuration, less time is consumed reconfiguring the arrays. This is why the MAMSC architecture 30333 produces 60 more images than the SFD 33024 architecture, even though both designs have the same 0.65 reliability at the end of one year.

Figure 7.3 provides many other observations that yield insight into the trade space of separated spacecraft interferometers. Architectures 55023, 55014, 30333, and 44013 have the best performance. These three architectures also provide the most baselines per configuration and have the highest total system reliability. On the basis of these results for the performance metric, one may conclude that, when trying to improve the performance for an SSI, it is more effective to spend money on additional spacecraft than to spend money to increase the reliability of the components of an array with fewer spacecraft.

7.3.3 Cost

Figure 7.4 shows the cost of each architecture according to the cost model developed in Chapter 6. The most striking observation is that the total system cost appears to scale directly with the total number of combiners in the array. Figure 7.5 shows the same plot with the number of combiners in the SSI increasing from left to right. This direct correlation may be attributed to two factors. First, a combiner payload is the single most expensive item in an SSI array, twice as

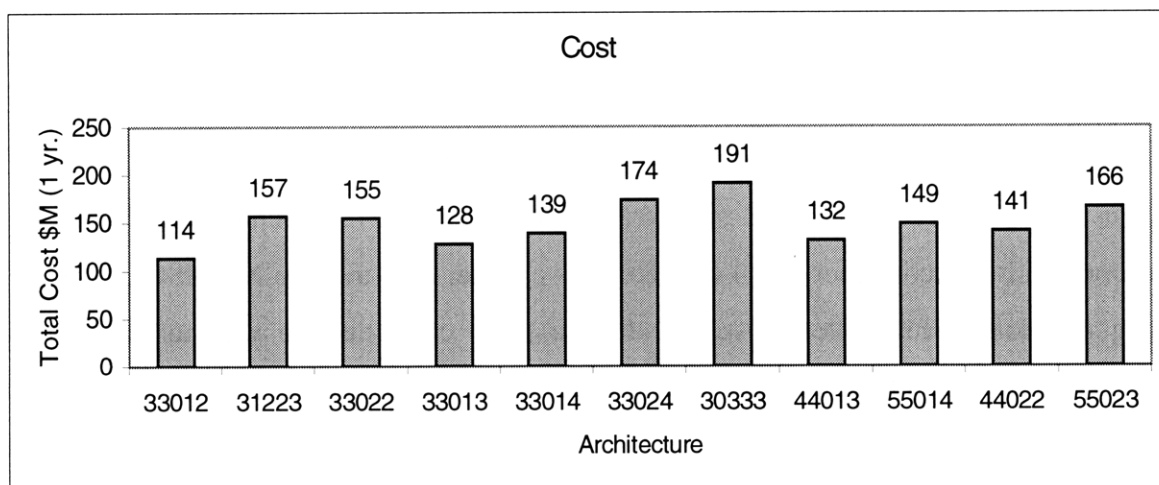


Figure 7.4: Cost of the SSI Architectures

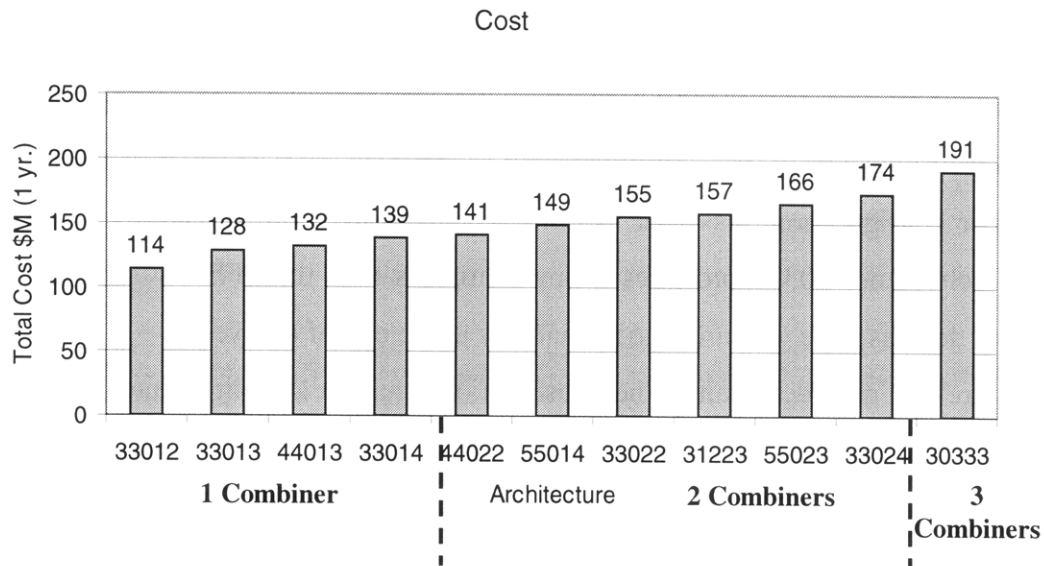


Figure 7.5: Cost of the SSI Architectures as a Function of the Number of Combiners in the Array

expensive as a collector payload and 1.1-1.5 times as expensive as a typical spacecraft bus. Second, a single combiner has a mass 2.5 times greater and requires 100 W more power than that of a single collector. This means that a combiner requires a significantly larger, more powerful bus to provide payload support than a collector. Thus, adding additional combiners to an SSI architecture increases the total payload cost, spacecraft bus cost, and possibly launch cost. To a lesser degree, the total system cost also scales with the total number of collectors in the array.

Figure 7.4 also shows that the SFD designs tend to be more affordable than the MAMSC designs, with architecture 33012 (3 SFD spacecraft with no payload redundancy) the cheapest at \$141 million and architecture 30333 (3 MAMSC spacecraft) the most expensive at \$191 million. A closer comparison of architectures 30333 and 44013 (4 SFD spacecraft with 1 combiner and 3 collectors) provides a case in point. Both architectures have a nearly identical reliability (0.65 vs. 0.66) and performance (202 images vs. 200), but the 4 SFD spacecraft architecture costs \$59 million less than the 3 MAMSC spacecraft architecture. Even architecture 55014 (5 SFD spacecraft with one combiner and 4 collectors) is cheaper than the two MAMSC designs. Thus, adding additional SFD collector spacecraft is a more cost-effective way to improve system performance and reliability than using MAMSC under the assumptions we have made.

7.3.4 Cost Per Function

Figure 7.6 shows the cost per function of each architecture. Recall that the cost per function is calculated by dividing the lifecycle cost by the total number of images produced (Eqn. 3.1). This yields the cost per image (CPI). This metric combines the outputs from the three models to tell the designer which architecture provides the best value for the money. Among the three-spacecraft architectures, design 31223 had the lowest cost per function of \$0.92 million per image. The fact that this hybrid SFD/MAMSC architecture rates as the most cost effective of the three-spacecraft architectures comes as somewhat of a surprise as the hybrid design did not distinguish itself individually during the evaluation of the previous three model outputs. This in turn shows the power of the cost per function metric to find non-intuitive solutions to design problems with many variables, solutions that might otherwise be hidden by the complexity of the system.

Of all the architectures analyzed, designs 44013, 55014, and 55023 had by far the lowest cost per function values of 0.66, 0.60, and 0.59. According to these results, the most efficient design is a design with many SFD spacecraft. Reflecting upon the previous three metrics, we see that:

1. Reliability was maximized by maximizing the number of spacecraft in the array and having a redundant combiner spacecraft.
2. Performance was maximized when both the number of available instantaneous baselines in a single configuration and the total reliability of the system were high. Both of these properties scale directly with the total number of spacecraft in the array.
3. It is cheaper to insert additional collector payloads into an SSI array than additional combiner payloads.

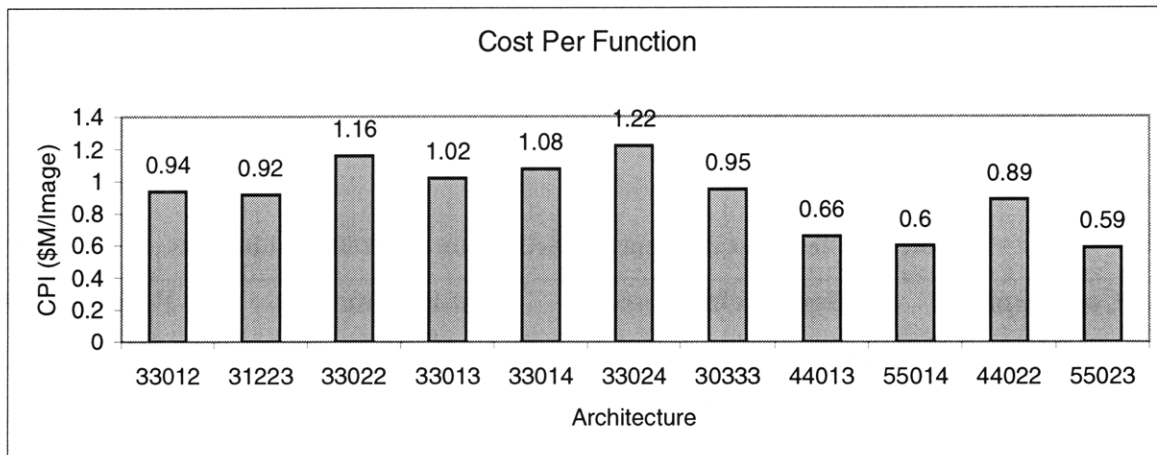


Figure 7.6: Cost Per Function of Each SSI Architecture

In keeping with these trends, the best architecture on the basis of cost per function was 55014 and 55023. These SFD architectures had the most spacecraft of all the arrays analyzed. Larger SFD arrays may further reduce the cost per function, but were not tested due to computational limitations.

7.3.5 Architecture Rankings

The DSS GINA methodology has provided a careful, quantitative analysis of the various SSI architectures. At the end of this process, the systems designer must choose the “best” design to carry into the next phase of the systems engineering process. There is no single method to choose the best design. In fact, this selection often depends on many programmatic, political, and technical factors. Ignoring political factors, this section briefly outlines two separate methods by which one may select a single architecture on the basis of the metrics calculated from the DSS GINA analysis.

One way to select the best design is to directly rate each architecture against the model outputs. For example horizontal lines could be drawn on Figures 7.2-7.4 denoting the minimum required reliability, minimum needed performance, and maximum allowable cost due to program constraints. Each design that exceeds these bounds is immediately removed from the set of acceptable design architectures. Of the remaining designs for consideration, select the design that meets all the capability requirements at minimum cost. Table 7.2 lists the best SSI architecture on the basis of the cost per image metric for different mission cost caps. Notice that the first three architectures, all of which use five spacecraft, provide roughly the same value.

Absolute cost may not be the overriding issue, however. Rather, the customer might like to receive the most value for the money. In this case, the DSS cost per function metric directly identifies the best design. For the SSI architectures considered here, 55014 and 55023 provide the most number of images per dollar spent.

Table 7.2: Best Cost Per Function Architecture for Different Budgets

| Cost Limit (\$M) | Best Architecture | Cost Per Image (\$M) | Performance (# Images) |
|-----------------------------|--------------------------|---------------------------------|-----------------------------------|
| 200 | 55023 | 0.59 | 282 |
| 175 | 55023 | 0.59 | 282 |
| 150 | 55014 | 0.60 | 250 |
| 135 | 44013 | 0.66 | 200 |

7.4 Uncertainty Analysis

An uncertainty analysis is a measure of how variations in certain architecture assumptions affects the entire system “performance” in terms of the system metrics. Uncertainty analyses are conducted because in reality the exact values for many of the architecture assumptions are unknown during the conceptual design stage, but bounds on their variations may be specified with some accuracy. Thus, it becomes important to know the degree to which these uncertainties may affect the results and whether or not they will change the determination of the best architecture. The next three sections perform an uncertainty analysis to see how uncertainties in the spacecraft bus cost, learning curve, and component reliability affect CPI metric of the eleven architectures presented in this chapter.

7.4.1 Spacecraft Bus Cost

All of the spacecraft bus costs were calculated via a weighted-average algorithm (Eqn. 6.2) encompassing selected Cost Estimation Relationships (CERs) from Versions 7.4 and 8.0 of the Aerospace Corporation Small Satellite Cost Model (SSCM). Each CER has associated with it a standard error (σ), which gives a spacecraft bus cost range over which there exists a 66% chance that the true bus cost will fall within this interval. The total standard error of each final spacecraft bus cost estimate is also the squared weighted average of all the squared standard errors [Bearden, 1996]. Thus, each spacecraft bus cost has associated with it an uncertainty. These uncertainties lead to an overall uncertainty in the output of the spacecraft bus subsection of the cost model, which in turn creates an uncertainty in the CPI metric used to compare and rank the different SSI architectures.

Figure 7.7 plots the nominal values (asterisk) of the cost per function metric for each SSI design architecture along with error bars signifying the upper and lower bounds ($\pm 1\sigma$) illustrating the possible effect of the spacecraft bus cost uncertainties on the total cost per image. As one can see, significant overlap exists among the seven three-spacecraft architectures when the uncertainty in the cost of each spacecraft bus is taken into account. This may change the ranking of the three-spacecraft SSI architectures. From Figure 7.7, it appears that architectures 33012, 31223, and 30333 all rate about equally for the best three-spacecraft SSI architecture when taking into account the uncertainty of the spacecraft bus costs. Architectures 55014 and 55023 still rate as the best overall designs.

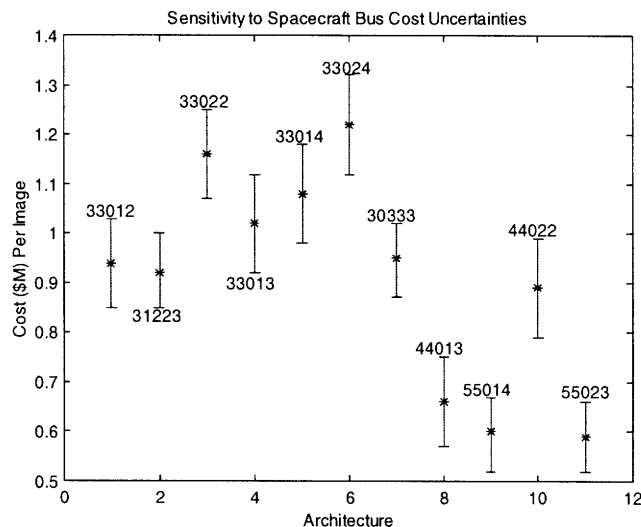


Figure 7.7: Effect on the Cost Per Image Metric of the Spacecraft Bus Cost Uncertainties in the Aerospace Corporation’s Small Satellite Cost Model

with the difference between the two being indistinguishable when taking into account the spacecraft bus cost uncertainties.

7.4.2 Learning Curve

As defined in Chapter 6, the learning curve is a mathematical technique that accounts for productivity improvements as larger numbers of units are produced (Eqns. 6.3–6.5). While the slope of the learning curve (S) in the aerospace industry varies between 85% and 100%, all simulations in the SSI cost model assumed an S of 95%. Changing the slope of the learning curve directly affects both the total payload cost and total spacecraft bus cost subsections of the cost model. This in turn changes the entire cost of the mission and introduces an uncertainty in the CPI metric.

Figure 7.8 plots the nominal values (asterisk) of the CPI metric for each SSI architecture along with error bars signifying the upper and lower bounds, illustrating the maximum possible effect a variation in the learning curve slope can have on the total cost per function. The upper bound represents the case where there is no learning curve ($S=100\%$), and the lower bound represents the case where the learning curve is the maximum allowable ($S=85\%$). Notice that the error bars are not as large here as in the previous section. While there is less overlap in this case, architectures 33012, 31223, and 30333 still rate as the best three-spacecraft designs and architectures 55014 and 55023 are still the best overall designs.

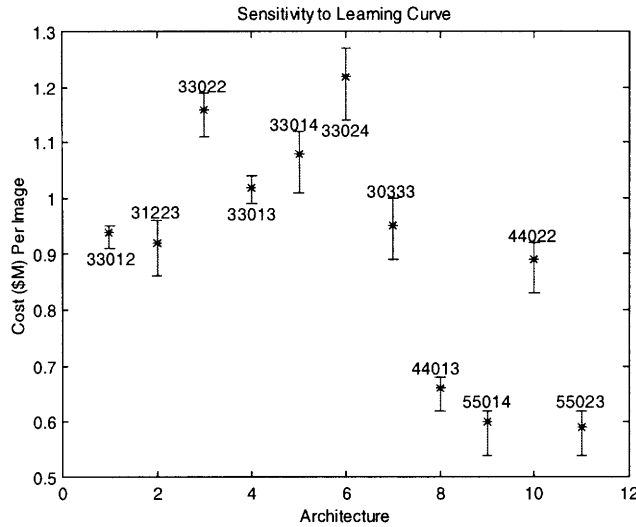


Figure 7.8: Effect on the Cost Per Image Metric of the Learning Curve Slope Uncertainties

7.4.3 Failure Rates

In Section 5.2, the rationale behind the component failure rates used in the reliability model were explained. While there is a large historical database on the failure rates of satellite buses, no such database exists for space-qualified interferometer collector and combiner components. The failure rates for the actual collector and combiner components that fly on an SSI could significantly differ from those assumed in Section 5.2. A variation in these failure rates, which serve as an input to the Markov model, influences calculation of the total number of images the system can produce in a given period of time and the operations cost over this time, both of which affect the cost per function metric.

Figure 7.9 plots the CPI metric for each architecture over a wide range of values of a quantity termed the “Reliability Ratio,” which is the ratio between the failure rate of the collector and combiner.

$$\text{Reliability Ratio} = \frac{\lambda_{col}}{\lambda_{com}} \quad (7.1)$$

As one can see, the cost per function of each architecture varies only slightly as the reliability ratio is varied from 40% below to 40% above the nominal value (0.267) used in the original reliability model simulations. This implies that the CPI of SSI architectures is fairly insensitive to 40% variations in the collector and combiner failure rates.

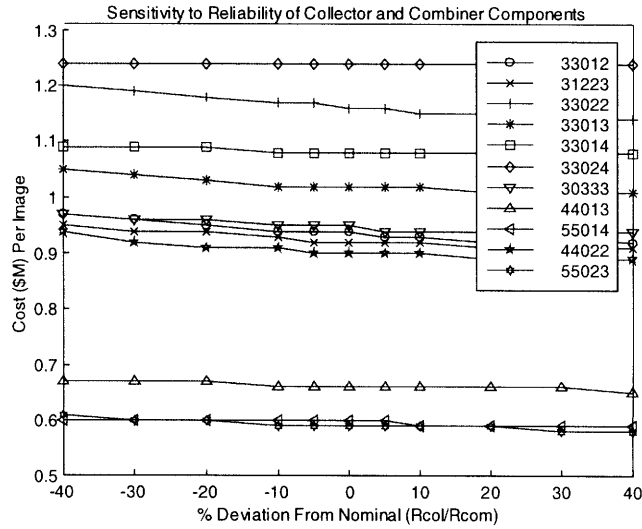


Figure 7.9: Sensitivity of the Cost Per Function Metric to the Reliability Ratio

7.5 Sensitivity Analysis

A sensitivity analysis is a measure of how a change in a single architecture assumption or requirement affects the entire system “performance” in terms of the system metrics. Sensitivity analyses are conducted because, in reality, no point design remains frozen as all designs change over time. This occurs because the actual values for the architecture variables used in the implementation of a design will be different from the theoretical values used during the conceptual design phase of the project. A sensitivity analysis allows the user to assess ahead of time how such changes will affect the capability, reliability, and cost of the system; and whether or not such variations will change the choice of the “best” architecture.

In Section 3.3a.3, the GINA adaptability metric was defined as the sensitivity or elasticity of the cost per function of an architecture to incremental changes in a particular design variable. Elasticity is a tool commonly used in the field of economics to determine the responsiveness of the demand for a product to a change in price of the product [McEachern, 1994]. For SSI design, elasticity (E) may be thought of as the responsiveness of the cost per image of a particular architecture to a change in value of an architecture design variable, assumption, or requirement; and can be calculated in the following manner:

$$E = \frac{\left[\frac{CPI_O - CPI_N}{0.5(CPI_O + CPI_N)} \right]}{\left[\frac{x_O - x_N}{0.5(x_O + x_N)} \right]} \quad (7.2)$$

where CPI_O is the original cost per image, CPI_N is the new cost per image, x_O is the old value for the parameter x , and x_N is the new value for the parameter x . Essentially, the elasticity is a measure of the percentage change in one variable due to a percentage change in another variable.

From economic theory, the relationship between the two variables in Equation 7.2 may be defined as inelastic, unitarily elastic, or elastic [McEachern, 1994]. When E has a value less than one, the CPI is said to be inelastic to that parameter – the percentage change of the CPI is less than the percentage change of the parameter. If E equals one, the CPI is unitarily elastic- the percentage change in the CPI is equal to the percentage in the parameter. Finally, when the CPI is greater than one, it is termed elastic – the percentage change in the CPI is greater than the percentage change in the parameter.

Evaluating the elasticity of the CPI for an SSI helps one to determine which variables are the most important in the design architecture. The next five sections perform a sensitivity analysis to see how the SSI architecture design variables of cost, learning curve slope, component reliability, imaging rate, and mission design life affect the cost per image of the eleven architectures presented in this chapter.

7.5.1 Costs

The CPI is unitarily elastic with the total system cost. Because the CPI is simply the total system lifecycle cost of the SSI divided by the then number of images it produces, a given percentage change in the total cost will produce an identical change in the CPI. Figure 7.10 plots the elasticity of the CPI to the different components of the lifecycle cost. The payload, spacecraft bus, and launch costs all exert approximately the same influence on the design, with elasticity ranging between 0.25 and 0.40. In contrast, the operations cost exerts considerably less influence on the CPI, with the elasticity of all the architectures being less than 0.1. Thus, SSI architectures are not as sensitive to changes in operations costs as they are to changes in payload, spacecraft bus, and launch costs.

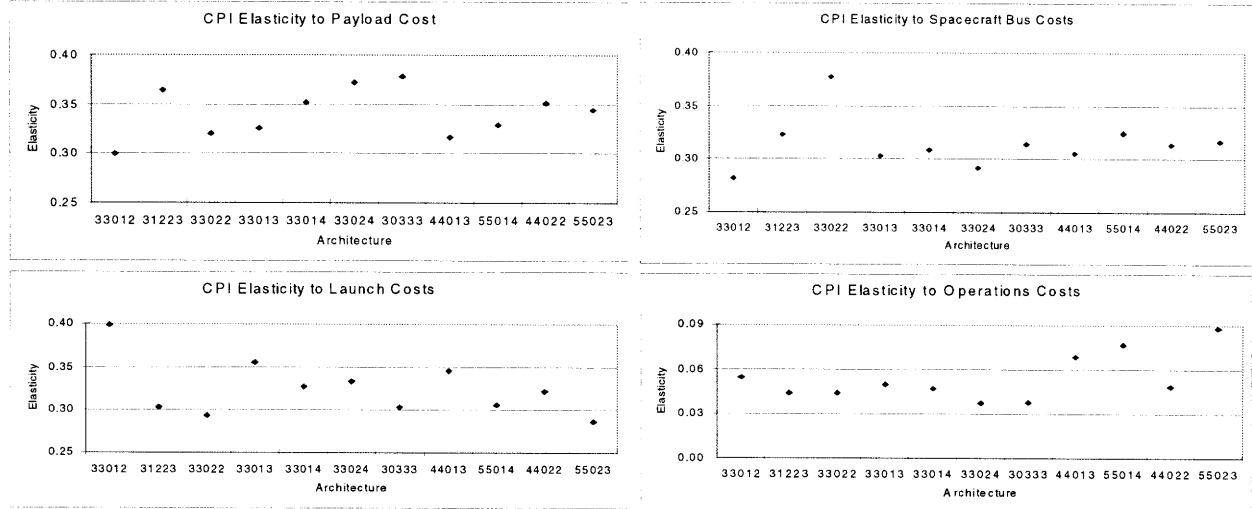


Figure 7.10: Cost Per Image Elasticity to (clockwise from top left corner) Payload Costs, Spacecraft Bus Costs, Operations Costs, and Launch Costs

7.5.2 Learning Curve Slope

Figure 7.11 plots the elasticity of the CPI to the learning curve slope used in the cost model. The architectures with the greater number of repeated components (collectors, combiners, and buses) are more elastic – a change in the slope of the learning will exert a greater influence on the payload and bus costs, and therefore the CPI. For example, architecture 44013 (three collectors and four buses) is more elastic than architecture 33012 (two collectors and three buses). Thus, we may conclude that learning curves play an increasingly important role as the size of a Distributed Satellite System increases. Therefore manufacturability plays an increasingly important role as more satellites are employed.

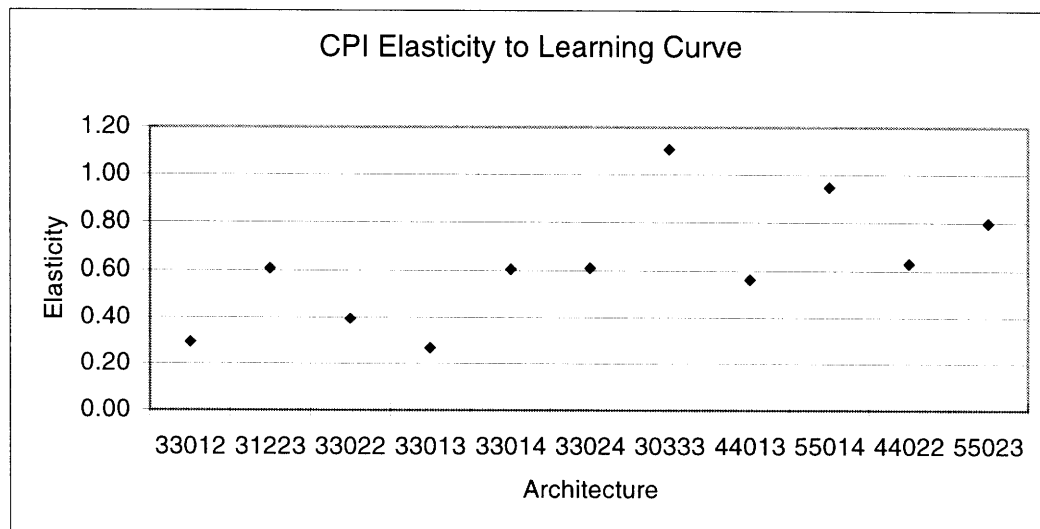


Figure 7.11: Elasticity of the Cost Per Image to the Learning Curve Slope

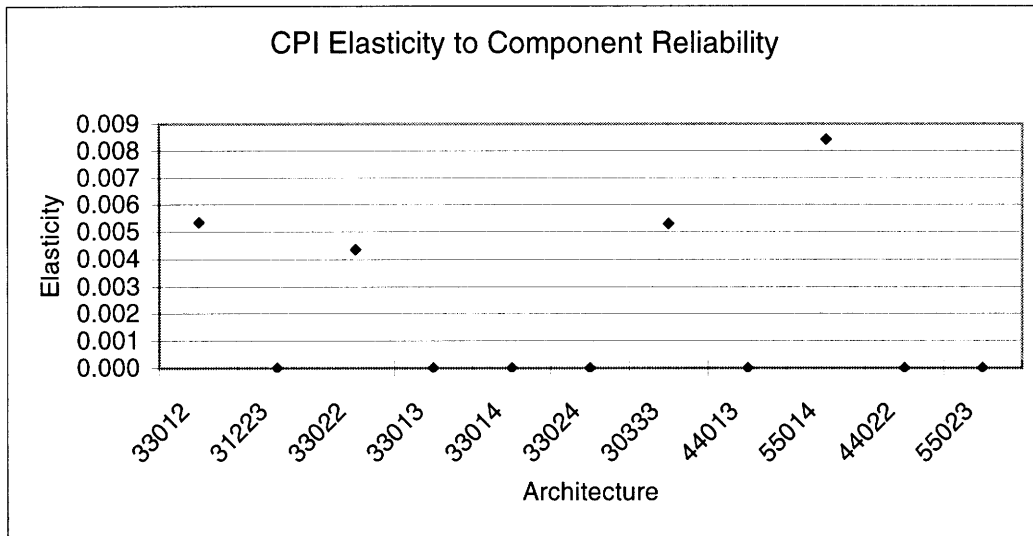


Figure 7.12: Cost Per Image Elasticity to Component Reliability

7.5.3 Component Reliability

Figure 7.12 plots the elasticity of the CPI to component reliability. The CPI of all the architectures is highly inelastic to changes in the reliability of different components for SSI missions with a design life of one year. All of the elasticity values are less than 0.01. These results correspond with our observation in Section 7.4.3 that the CPI was insensitive to uncertainties in the reliability ratio. Thus, we may conclude that spending money to increase the reliability of different components in the array will not yield a cost-effective improvement in the performance of the system.

7.5.4 Imaging Rate

Figure 7.13 plots the *CPI* elasticity to the imaging rate for each architecture. For the

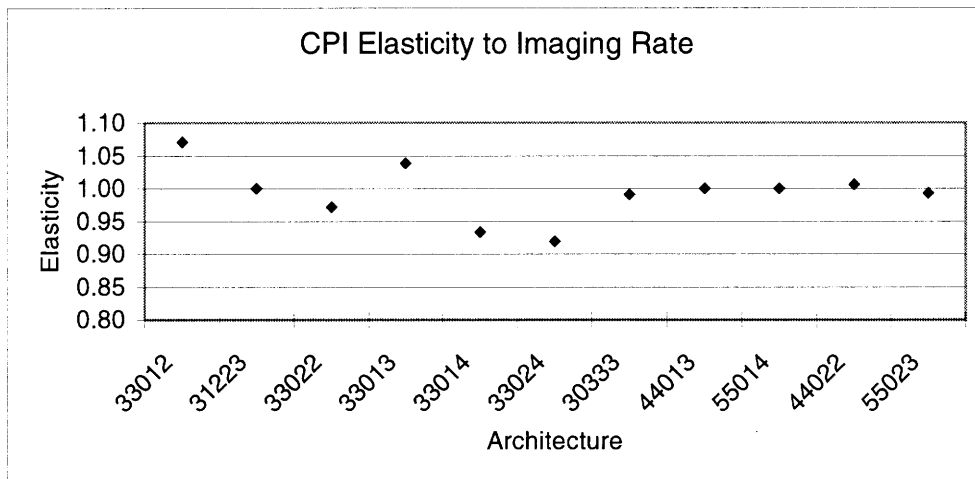


Figure 7.13: Cost Per Image Elasticity to the Imaging Rate

same reason as total system lifecycle cost, the *CPI* is nearly unitarily elastic to the imaging rate. Thus, designing SSI architectures for a higher imaging rate will exert a strong downward pressure on the *CPI* and improve the cost-effectiveness of the architectures.

7.5.5 Mission Design Life

The mission design life (MDL) refers to the period of time over which the sponsoring agency intends to operate the mission, and is usually dependent upon how much money that agency has allocated to operations costs. The MDL affects the cost per function metric by determining both the total number of images the system produces and the total operations cost of the system. The nominal value for the MDL used in the original simulations was one year. Figure 7.14 plots the elasticity of the *CPI* to the MDL. Each architecture exhibits similar behavior, with an elasticity between 0.50 and 0.70.

Figure 7.15 plots the cost per function of each architecture as a function of the mission design life from an MDL of 1 month to an MDL of 10 years. The MDL has a significant effect on the cost per image, with the value of the *CPI* decreasing as the MDL increases. This means that the increase in the total number of images enabled by lengthening the MDL outweighs the increase in operations costs. The curve eventually flattens out when all of the components in the system fail (ie. no more images are being produced and no more money is being spent to operate the system). The relative ranking remains the same, however, with the performance of architectures 55014 and 55023 still the best and virtually indistinguishable from each other.

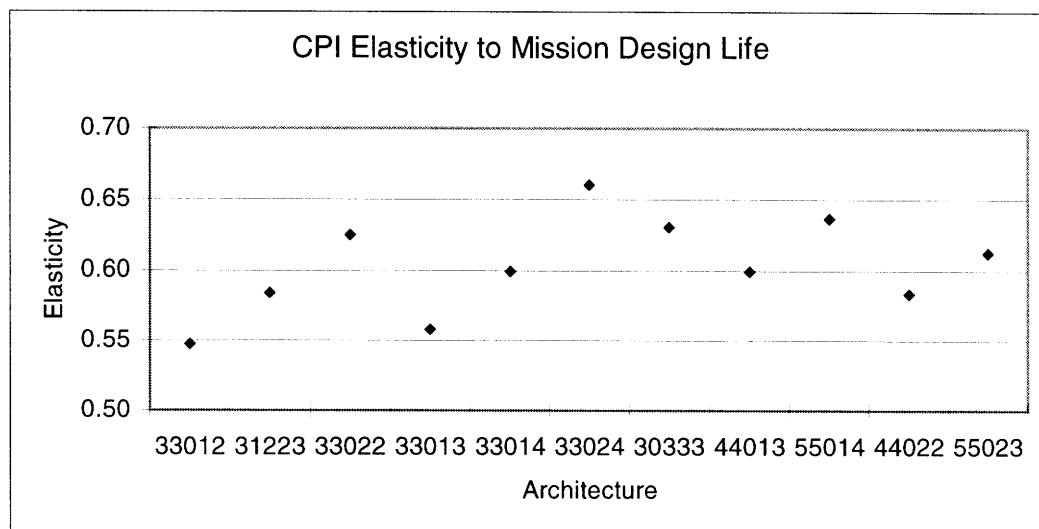


Figure 7.14: Cost Per Image Elasticity to Mission Design Life

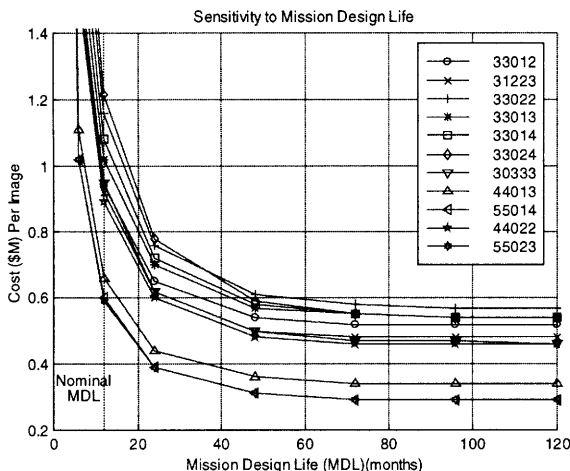


Figure 7.15: Sensitivity of the Cost Per Image Metric to the Mission Design Life

7.6 Results Summary

To review, architectures 55014 and 55023 – 5 SFD spacecraft with 1 combiner and 4 collectors and 5 SFD spacecraft with 2 combiners and 3 collectors - rate as the best designs on the basis of the DSS metrics for the given set of mission requirements and assumed design constants. This ranking is the result of many trends that have become evident throughout this work. SSI architectures with many available instantaneous baselines per configuration and a high total system reliability achieve the best performance in terms of the number of images produced in one year. Architectures 55014 and 55023 provide for many available interference baselines *and* provide the greatest total system reliability. Even though architecture 55023 has the third highest cost, it yields the lowest cost per function of \$590,000 per image produced. A sensitivity analysis shows that the cost per image of each architecture was insensitive to changes in the failure rate of the collector and combiner components, but decreased as the mission design life increased. Uncertainties in the total system cost due to the standard error in calculating spacecraft bus costs and assumptions in the learning curve also affected the cost per function metric. In all cases, however, the relative ranking of the architectures remained the same. The SSI design trends observed throughout this process as well as the final results illustrate the powerful ability of the DSS GINA methodology to find non-intuitive correlations and design solutions that might otherwise be masked within the nonlinear variable connectivity of complex systems with many design parameters. With this formal systems engineering and architecting process in place, additional design features and refinements, including additional architectures, can be added and analyzed.

Chapter 8

Conclusions

“The job is to ask questions – it always was – and to ask them as inexorably as I can. And to face the absence of precise answers with a certain humility.”

- Arthur Miller

The primary research objective was to explore and “optimize” via Distributed Satellite System (DSS) principles the trade space involved in the design of future separated spacecraft interferometers. Eleven separate design architectures for an optical separated spacecraft interferometer (SSI) ranging in size from three to five spacecraft were analyzed on the basis of four metrics – capability, performance, adaptability, and cost per function (CPF). The most important metric is the CPF, which is defined as the total lifecycle cost divided by the total number of images the system produces. Additionally, both single function design (SFD) spacecraft and modular and multifunction spacecraft (MAMSC) were considered. The two optimum system architectures are summarized in Table 8.1.

Table 8.1: Optimal System Design Architectures

| | Architecture 55014 | Architecture 55023 |
|---|-------------------------------|-------------------------------|
| Total Number of Spacecraft | 5 | 5 |
| Spacecraft Type | SFD | SFD |
| Number of Combiner Payloads | 1 | 2 |
| Number of Collector Payloads | 4 | 3 |
| Number Baselines Available Per Configuration | 6 | 3 |
| Max. Imaging Rate (images/month) | 26.8 | 29.9 |
| Reliability (t=1 year) | 0.68 | 0.83 |
| Total Number Images Produced (t=1 year) | 250 | 282 |
| Total Cost (\$M through 1 year of operations) | 148.9 | 166.3 |
| Cost Per Image (\$M) | 0.60 | 0.59 |

From these results, several primary conclusions may be drawn:

1. *Imaging Rate is the single most important design driver for the economical use of future separated spacecraft interferometers.*

The two optimal system design architectures had the highest imaging rates of all the architectures considered. The higher the system imaging rate, the more images the interferometer will be able to obtain in a given amount of time. It was demonstrated in Chapter 4 that imaging rate improves $O(n^2)$ with the number of collector spacecraft and $O(n)$ with the number of combiner spacecraft in the array.

2. *Improving total system reliability by adding redundant payloads to the same spacecraft is not cost effective. Improving system reliability by introducing new payloads on new spacecraft is cost effective.*

Adding redundant payloads to the same spacecraft allows the system to maintain the same slower imaging rate over a longer period of time. Placing these same payloads on new spacecraft allows them to be utilized immediately and boosts the imaging rate. In this case, the system does not enter the lower performance state (slower imaging rate) until after component failures begin to occur. The four SSI architectures with redundant payloads performed the worst on the basis of the CPF metric. However, it was assumed that the failure rate was not dependent upon whether a component was used or shut off.

3. *For similar sized arrays, total system cost scales directly with the total number of combiner payloads in the array.*

Combiner payloads are approximately twice as expensive, three times as massive, and require 100 more watts of power than collector payloads. Thus, combiners require significantly larger, more expensive spacecraft buses for support than do collectors. The increase in mass of the spacecraft bus cascades down to launch, where a more powerful, expensive launch vehicle is required to deploy the system. This conclusion is illustrated in Figure 7.5.

Based on these conclusions, the primary distinguishing factors, in order of influence on the CPF metric, for the design of future optical SSI's should be:

1. Imaging Rate
2. Total System Cost
3. System Reliability

These are the most important distinguishing factors as they drive the system performance and cost. The framework for the SSI performance model was developed in Chapter 4. In Chapter 5, a reliability model for SSI's was derived and coupled with the capability model to calculate the performance of each architecture taking into account the failures that are likely to occur once the system begins operation. Chapter 6 outlined the cost model used to estimate the cost of each architecture.

Throughout this process, the philosophy of Distributed Satellite Systems was stressed. Past space-based interferometry system studies found that distributing the collector and combiner payloads across several spacecraft, rather than placing all of the payloads on a single spacecraft, allowed for larger baselines and thus greater angular resolutions (Surka et al, 1996) as well as more flexibility in controlling the u-v coverage of the images (Stephenson et al, 1998). This study has shown that distribution also provides improved reliability, increased cost savings due to production learning curves, and a higher imaging rate.

In Chapter 1, it was stated that the primary goal of this work was *to explore and "optimize" via Distributed Satellite System (DSS) principles the trade space involved in the design of future visible spectrum astronomical separated spacecraft interferometers*. In doing so, it was found that by viewing a space-based interferometer as network, significant improvements in reliability, performance, and cost over current SSI designs can be achieved.

The seven objectives of this work, listed in Chapter 1, are restated below along with an explanation of how they were achieved.

1. *To develop capability, reliability, and cost models that quantify the SSI system cost per function for a variety of architectures.*

These models have been developed in Chapters 4-6. The cost model in Chapter 6 provides a means for estimating the total lifecycle cost of each candidate architecture. Lifecycle cost includes the cost of payload development, spacecraft bus development, launch, and operations. The denominator of the CPF metric requires a functionality model of the system over the lifetime of the mission in the presence of failures. The capability, or instantaneous performance, model in Chapter 4 calculates how each design variable affects the imaging rate of the SSI. The reliability model in Chapter 5 determines the probability that the SSI is functioning in each possible state as a function of time. The outputs from these two models are then coupled in a utility function to calculate the total lifetime performance of the architecture, taking into

account failures. These models may be used to evaluate a wide variety of SSI architectures not considered in this work.

- 2. To optimize the SSI system architecture with respect to the cost per function (CPF) metric.*

Eleven separate SSI architectures were examined in this thesis. The chosen baseline architecture (33012) was the three SFD spacecraft New Millennium Interferometer proposed for the Deep Space 3 (DS3) mission. Alternate architectures included SFD, MAMSC, and hybrid designs containing three to five spacecraft (Figure 7.1). Of these eleven architectures, the two architectures with five spacecraft (55014 and 55023) had the lowest CPF. This shows how increasing the distribution of an SSI can actually increase the value of the system.

- 3. To evaluate quantitatively the advantages and disadvantages of incorporating modular and multifunctional spacecraft (MAMSC) into SSI arrays.*

In this study, the MAMSC architectures (31223 and 30333) contained both collector and combiner payloads on a single spacecraft bus. In Chapter 7, it was shown that while the three-spacecraft MAMSC architectures are more expensive than the three-spacecraft SFD architectures, their improved system reliability and increased imaging rate actually lead to a decrease in the CPF metric. However, even greater reductions in the CPF were achieved by adding additional SFD spacecraft (44013, 44022, 55014, and 55023) to the baseline architecture (33012).

- 4. To identify how the performance of SSI arrays evolves with respect to each metric as a function of the number of spacecraft in the array.*

In Chapter 4, it was shown that increasing the number of collector spacecraft and/or combiner spacecraft in an SSI increases the SSI imaging rate. From equations 5.7 and 5.13, it was seen that increasing the total number of spacecraft in an SSI also improves the reliability of the architecture. The cost model in Chapter 6 illustrates that the cost of an SSI increases as the number of spacecraft in the array increases. Finally, Figure 7.6 illustrates how the CPF decreased as the number of spacecraft in an SSI increased. It is not yet known at what size architecture this trend reverses itself.

- 5. To determine the sensitivity of the cost per function metric to different design assumptions and requirements.*

Sections 7.4 and 7.5 compute the sensitivity of the CPF metric to various design uncertainties, assumptions, and requirements. Uncertainty in the assumed spacecraft bus cost estimation relationships and assumed learning curve slopes exerted a noticeable effect on the CPF, while uncertainty in the failure rates of components did not. The computed elasticity's show that the CPF is most sensitive to the mission design life and the learning curve slope.

6. To develop design rules of thumb for optical separated spacecraft interferometers.

Several design rules of thumb may be derived from this case study. First, for a given number of spacecraft with given failure rates for each component, an array consisting entirely of MAMSC spacecraft will always have a higher total system reliability than an array consisting solely of SFD spacecraft. This rule of thumb flows naturally from the derivation of the formulas for total system reliability in Chapter 5. Second, if instantaneous system performance is the chief concern, then a design with as many collector spacecraft as allowed within budgetary constraints should be used. Additional combiner spacecraft also improve performance, but not as fast as additional collector spacecraft. This results from the fact that the instantaneous u-v coverage of an SSI improves $O(n^2)$ with the number of collector spacecraft. Finally, for a given set of conflicting mission objectives and parameters, the best compromise between performance and economy over the mission design life is the system with the lowest cost per function.

7. To document the Distributed Satellite System (DSS) Generalized Information Network Analysis (GINA) methodology on a real space system for reuse in the future.

Chapter 3 describes the DSS GINA methodology within the framework of the systems engineering and architecting process. It also explains the application of this methodology to the SSI mission. Section 7.2 then outlines in detail how each SSI architecture was developed and evaluated, referencing all pertinent equations. The mathematical models and associated computer codes developed in Chapters 4-6 may be applied to future SSI architecture studies. The GINA methodology is a useful systems engineering tool that reduces a large, complex design problem into manageable pieces with a core set of underlying metrics for comparing all architectures on the same basis. In doing so, GINA provides a generalized framework for analyzing and designing all types of space systems – commercial, scientific, and military. Thus, GINA is a powerful tool for the design of future distributed satellite systems.

A goal of future work will be to mathematically represent DSS design problems in a framework such that they can be solved by autonomous optimization algorithms, such as the simulated annealing and genetic algorithms. The process outlined here has yielded insight into the SSI design trade space that may someday be used to develop an operational separated spacecraft interferometer.

References

- Bearden, David A. The Aerospace Corporation. Personal Communication. August 3, 1998.
- Bearden, D.A. *Chapter 8.2: The Aerospace Corporation Small Satellite Cost Model. Reducing Space Mission Cost*. Editors J.R. Wertz and W.J. Larson. Microcosm Press. Torrance, CA. 1996.
- Beichman, C.A., ed., et al. *A Road Map for the Exploration of Neighboring Planetary Systems (ExNPS)*. NASA Jet Propulsion Laboratory Report. Number JPL 96-22. Pasadena, CA. August, 1996.
- Blackwood, G.H., Dubovitsky, S., Linfield, R.P., and Gorham, P.W. *Interferometer Instrument Design for New Millennium Deep Space 3*. SPIE International Symposium on Astronomical Telescopes and Instrumentation. Paper No. 3350-83, March 1998.
- Boeing. Delta II Family of Launch Vehicles. Boeing Informational Brochure. 1997.
- Boppe, Charles. Aerospace Product Design Personal Class Notes. 1998.
- Bracewell, R. *The Fourier Transform and Its Applications*. McGraw-Hill, New York. 1978.
- Colavita, M.M. McGuire, J.P. Bartman, R.K. Blackwood, G.H. Laskin, R.A. Lau, K.H. Shao, M. Yu, J.W. *Separated Spacecraft Interferometer Concept for the New Millennium Program*. SPIE Vol. 2807. 1996.
- Cornwell, T.J. *A Novel Principle for Optimization of the Instantaneous Fourier Plane Coverage of Correlation Arrays*. IEEE Transactions on Antennas and Propagation, Vol. 36, No. 8. August 1988.
- CNN. Congress: Why Didn't CIA Know About Indian Tests? <http://cnn.com/WORLD/asiapcf/9805/13/india.cia.wed/index.html>. CNN Web Page. May 13, 1998.
- DS3 Costing Workshop. New Millennium Program. PowerPoint Slides. March 21, 1997.
- Doody, David. *Deep Space Network*. The Planetary Report. July/August 1997.
- ESA. The Darwin Space Infrared Interferometer Project. <http://ast.star.rl.ac.uk:80/darwin/>. ESA DARWIN Web Page. 1998.
- Gelb, Arthur. *Applied Optimal Estimation*. The M.I.T. Press. Cambridge, MA. 1974.

- Gordon, Gary D. *Spacecraft Technology Reliability*. Communications Satellite Corporation. Clarksburg, Maryland. 1980.
- Hariharan, P. *Basics of Interferometry*. Academic Press Inc. San Diego, CA. 1992.
- Hecht, Herbert. *Reliability During Space Mission Concept Exploration*. Chapter 19.2 of Space Mission Analysis & Design. 2nd Edition. W.J. Larson and J.R. Wertz, Editors. Microcosm Inc. Torrance, CA. 1992.
- Jilla, C.D. and Miller, D.W. *A Reliability Model for the Design and Optimization of Separated Spacecraft Interferometer Arrays*. Proceedings of the 11th Annual AIAA/USU Conference on Small Satellites. 1997.
- Isakowitz, Stephen. International Reference Guide to Space Launch Systems. American Institute of Aeronautics & Astronautics. 2nd Edition. 1995.
- JPL. The Terrestrial Planet Finder. <http://origins.jpl.nasa.gov/missions/tpf.html>. JPL Origins Web Page. 1998.
- JPL. Multiple Spacecraft Interferometer Constellation (MUSIC). Presentation to NASA Headquarters. Jet Propulsion Laboratory Advanced Concepts Office. May 2, 1996.
- Kaplan, Mike. Origins Mission Definition and Technology. Presentation to Origins Technology Workshop. Dana Point, CA. June 4-6, 1996.
- Kong, M.C. Optimal Trajectories and Orbit Design for Separated Spacecraft Interferometry. Master's Thesis. MIT Department of Aeronautics and Astronautics. 1998.
- Kong, E.M. and Miller, D.W. *Optimization of Separated Spacecraft Interferometer Trajectories in the Absence of a Gravity Well*. SPIE Paper # 3350-13. Astronomical Interferometry Conference Proceedings. Kona, Hawaii. 1998.
- Larson, W.J. and Wertz, J.R. Eds. Space Mission Analysis and Design. Microcosm Inc. Torrance, CA. 1992.
- Lau, K. Colavita, M. and Shao, M. *The New Millennium Separated Spacecraft Interferometer*. Jet Propulsion Laboratory. 1996.
- LeDuc, J.R., Bromaghim D.R., Peterson, T., Pencil, E., Hoskins, W.A., and Meckel, N.J. *Pulsed Plasma Thruster (PPT) Development and Ground Testing in Support of PPT Flight Demonstrations on MightySat*. 11th AIAA/USU Conference on Small Satellites, Paper SSC97-XII-1.
- Linfield, R. *DS3 in Geosynchronous Orbit: A First Look at Orbital Dynamics, u-v Coverage and Detection Thresholds*. Jet Propulsion Laboratory Interoffice Memorandum 335.1-98-003. March 31, 1998.

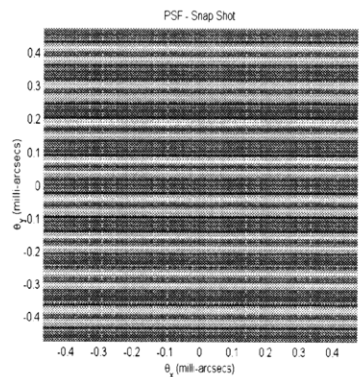
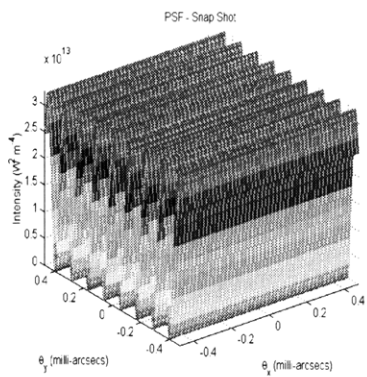
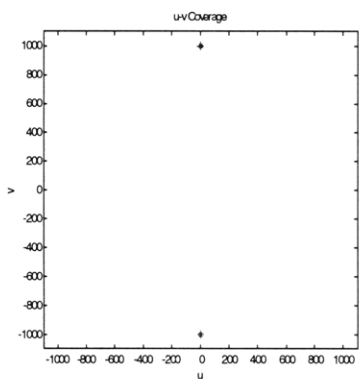
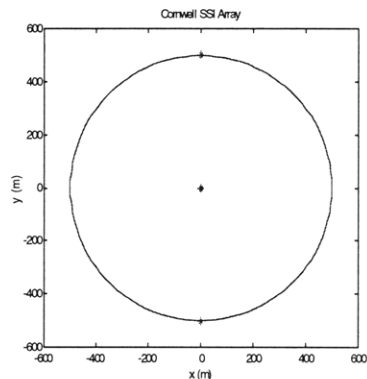
- McEachern, William A. Economics – A Contemporary Introduction. 3rd edition. South-Western Publishing Company. Cincinnati, Ohio. 1994.
- Miller, D.W., Crawford, S.L., Hyde, T.T., Masters, B.P., Crawley, E.F., Blackwood, G.H., Colavita, M.M., Yu, J.W., Shao, M., and Laskin, R. *System-wide design issues for the Stellar Interferometer Technology Experiment (SITE)*. SPIE Paper #2477-23. Spaceborne Interferometry II Proceedings. Orlando, FL. 1995.
- NASA Strategic Plan. National Aeronautics and Space Administration. Washington D.C. February, 1996.
- Narayan, R. and Nityanda, R. *Maximum Entropy Image Resolution in Astronomy*. Annual Review of Astronomy and Astrophysics. Vol. 24. 1986.
- Nisbet, A.M. Design of an Optical Interferometer Spacecraft. Master's Thesis. MIT Department of Aeronautics and Astronautics. 1992.
- Olliver, D.W. Kelliner, T.P., Keegan, J.G. Engineering Complex Systems. McGraw Hill. New York. 1997.
- Rohlfs, K., and Wilson, T.K. Tools of Radio Astronomy. 2nd Edition. Springer-Verlag. New York. 1996.
- Shao, M. and Colavita, M.M. *Long-Baseline Optical and Infrared Stellar Interferometry*. Annual Review of Astronomy and Astrophysics. 1992.
- Schwarz, V.J. *The Method "CLEAN" – Use, Misuse, and Variations*. Annual Review of Astronomy and Astrophysics. Reidel, Dordrecht. 1979.
- Shaw, G.B. The Generalized Information Network Analysis Methodology for Distributed Satellite Systems. PhD Thesis. MIT Department of Aeronautics and Astronautics. 1998.
- Shaw, G.B. and Hastings, D.E. *A Generalized Analysis Methodology for Distributed Satellite Systems*. 1997 IAF International Workshop on Satellite Constellation Analysis and Design. Analysis and Design of Satellite Constellations. Kluwer Academic Publishers. 1998.
- Shaw, G.B. Yashko, G. Schwarz, R. Wickert, W. Hastings, D. "Analysis Tools and Architecture Issues for Distributed Satellite Systems." H. Helvajian, ed. Aerospace Press. El Segundo, CA. 1998.
- Stephenson, R.L., Miller, D.W., and Crawley, E.F. Comparative System Trades Between Structurally Connected and Separated Spacecraft Interferometers for the Terrestrial Planet Finder Mission. SERC Report #3-98. MIT Space Systems Laboratory. 1998.
- Surka, D.M., and Crawley, E.F. A Comparison of Structurally Connected and Multiple Spacecraft Interferometers. SERC Report #9-96. MIT Space Systems Laboratory. 1996.

- Su, Frederick. *Interferometry at Keck Telescopes Creates Powerful Array*. An Interview of Dr. Mark Colavita. OE Reports. SPIE-The International Society for Optical Engineering. March, 1998.
- Thompson, A.R., Moran, J.M., and Swenson, G.W. Interferometry and Synthesis in Radio Astronomy. Krieger Publishing Company. Malabar, Florida. 1986.
- Wertz, J.R. and Larson, W.J., Editors. Reducing Space Mission Cost. Microcosm Press. Torrance, CA. 1996.
- Wohlleben, R., Mattes, H., and Krichbaum, T.H. Interferometry in Radio Astronomy and Radar Techniques. Kluwer Academic Publishers, Netherlands. 1991.
- Wong, Robert. *Chapter 20: Cost Modeling*. Space Mission Analysis and Design. 2nd Edition. W.J. Larson and J.R. Wertz. Microcosm Press. Torrance, CA. 1992.

Appendix A: u-v Coverage Results

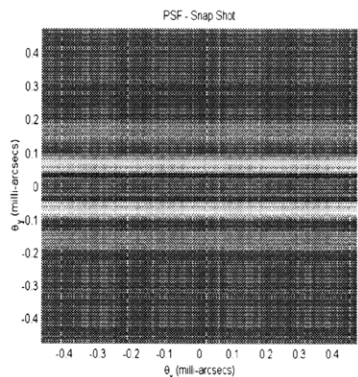
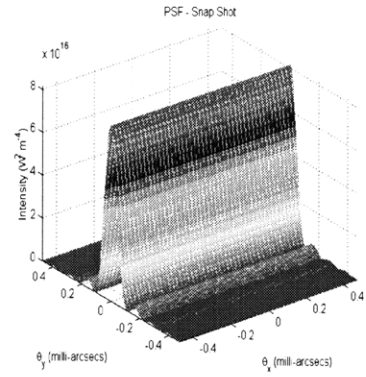
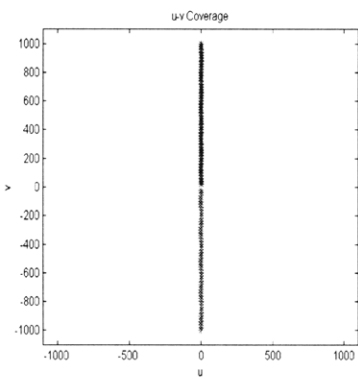
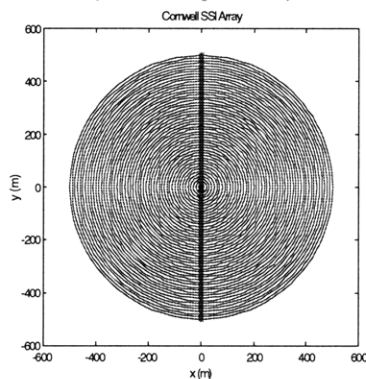
Architecture 33012

Snapshot



MSE=0.3851 (W/m²)²

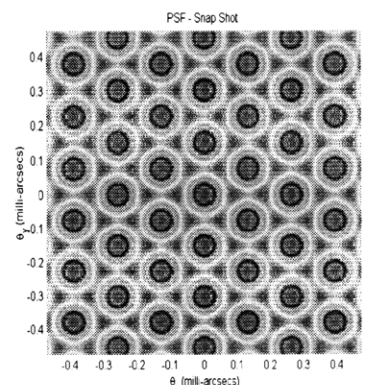
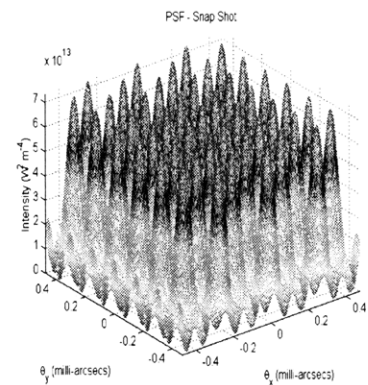
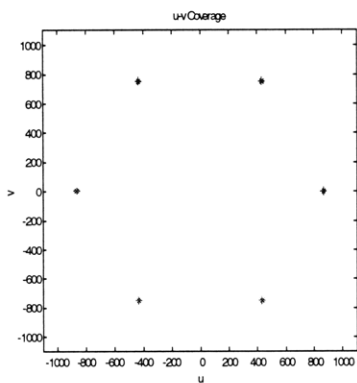
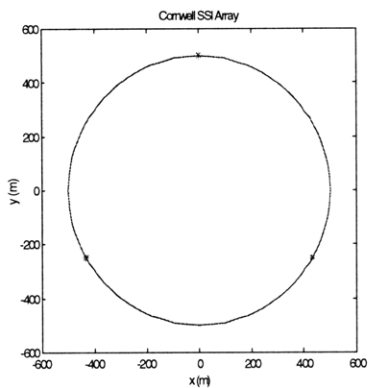
**High Resolution
(100 uv points)**



MSE=0.0653 (W/m²)²

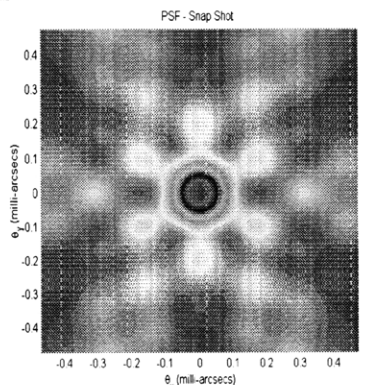
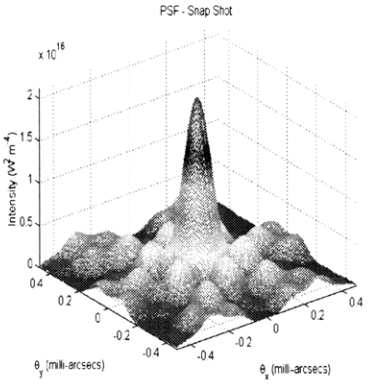
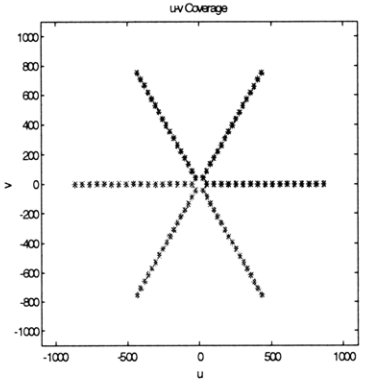
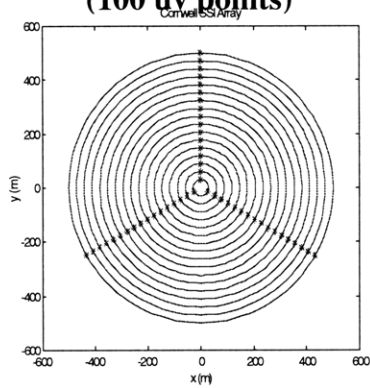
Architecture 31223

Snapshot



MSE=0.1751 (W/m²)²

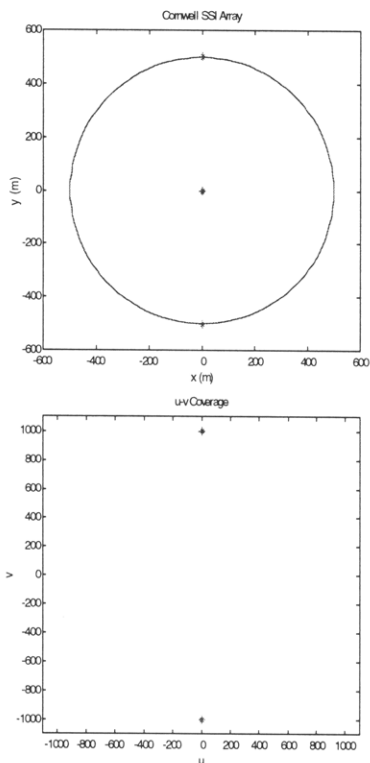
**High Resolution
(100 uv points)**



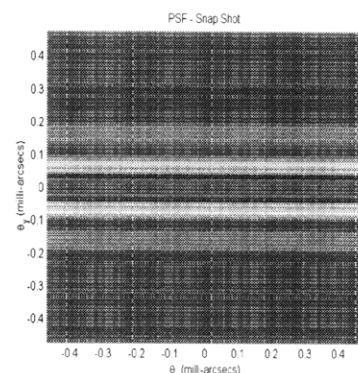
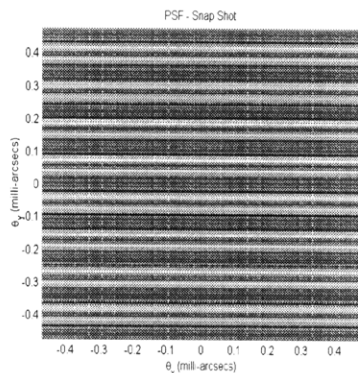
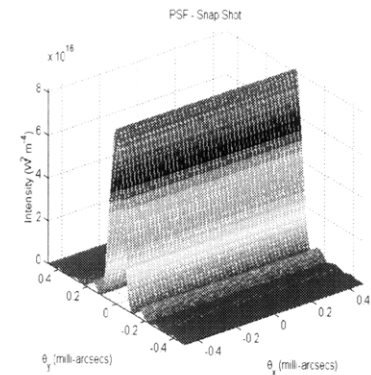
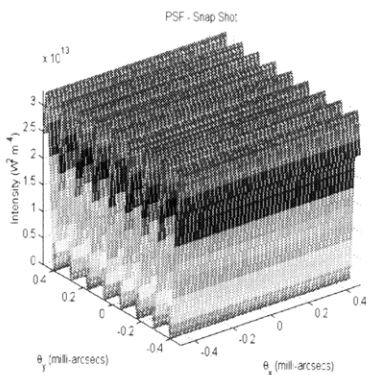
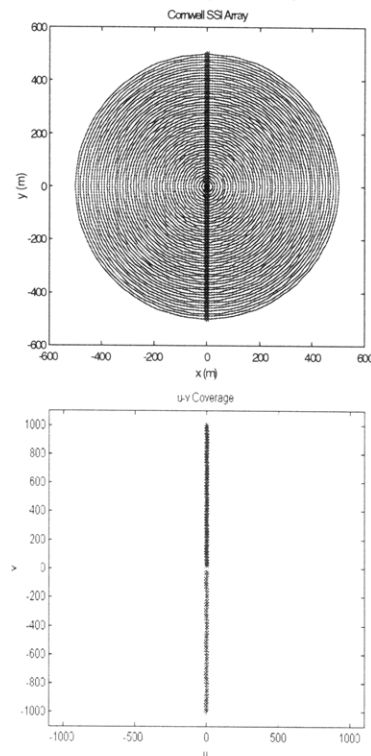
MSE=0.0069 (W/m²)²

Architecture 33022

Snapshot



**High Resolution
(100 uv points)**

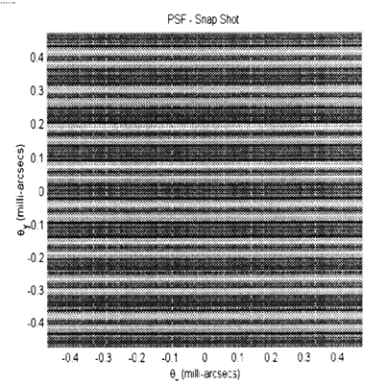
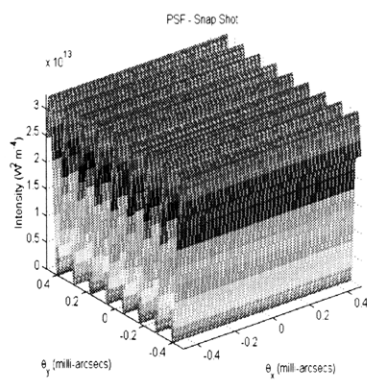
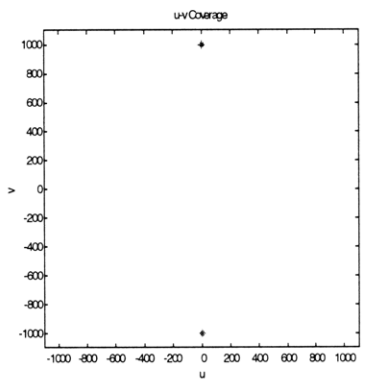
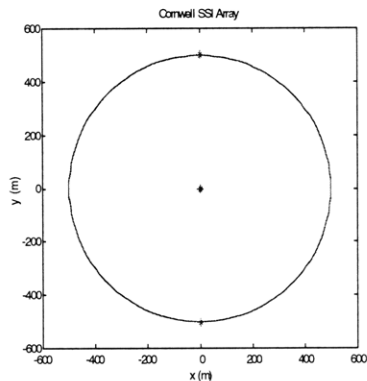


MSE=0.3851 (W/m²)²

MSE=0.0653 (W/m²)²

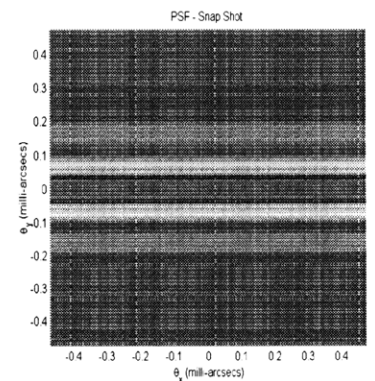
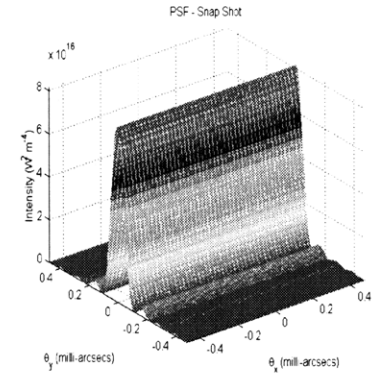
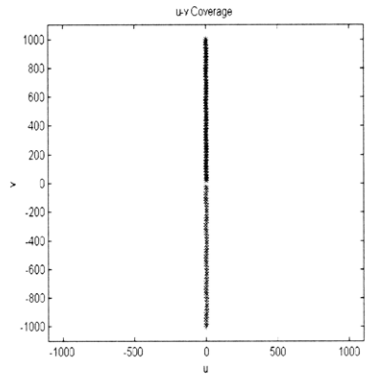
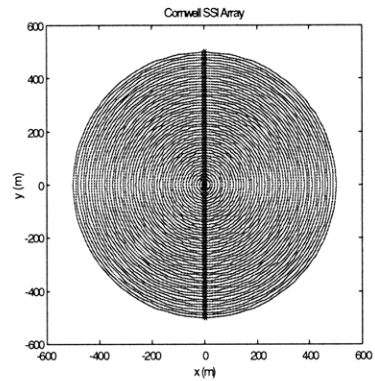
Architecture 33013

Snapshot



$$\text{MSE}=0.3851 \text{ (W/m}^2\text{)}^2$$

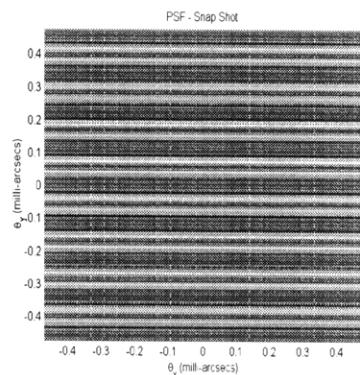
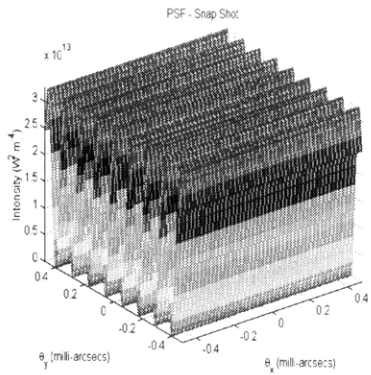
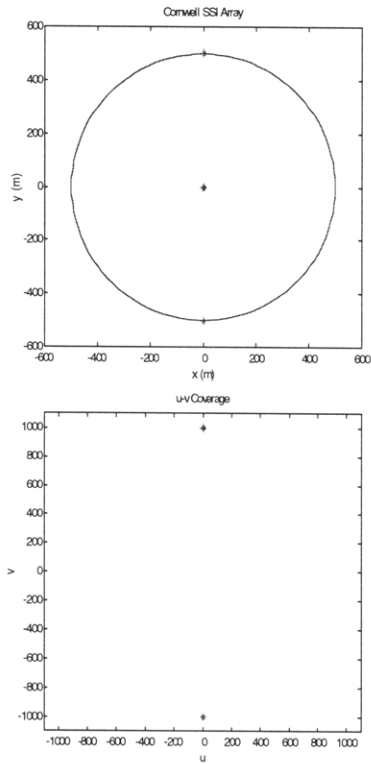
**High Resolution
(100 uv points)**



$$\text{MSE}=0.0653 \text{ (W/m}^2\text{)}^2$$

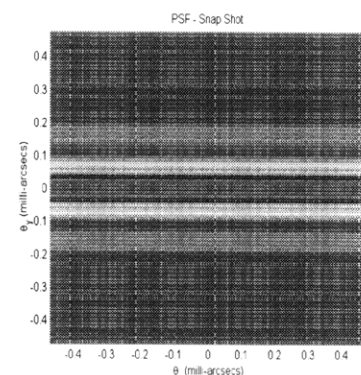
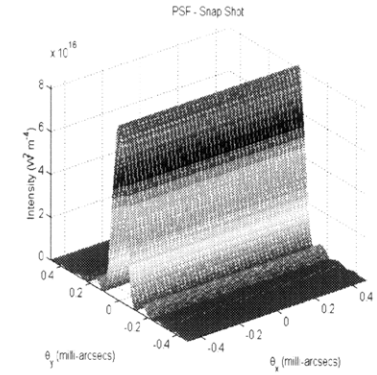
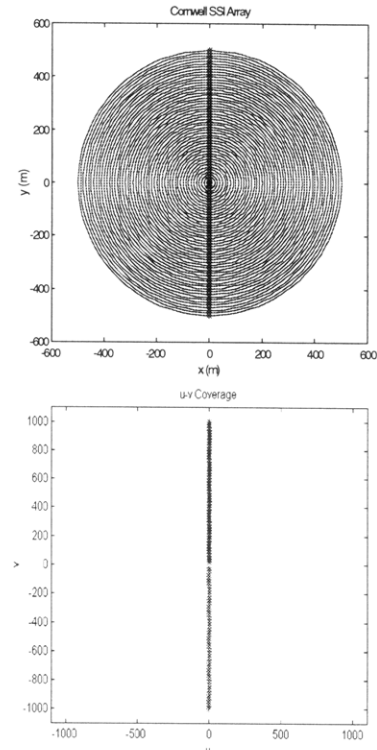
Architecture 33014

Snapshot



MSE=0.3851 (W/m²)²

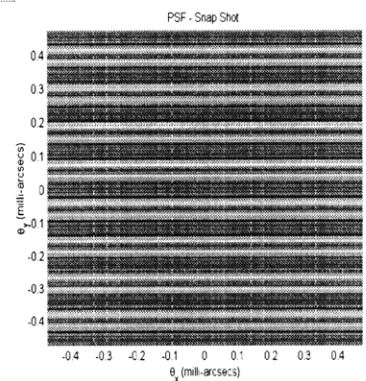
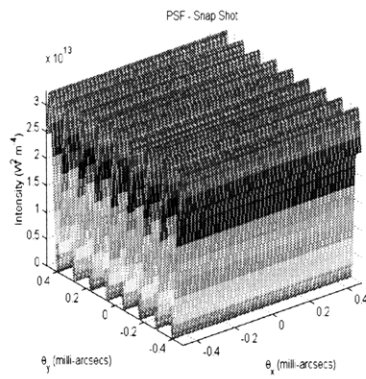
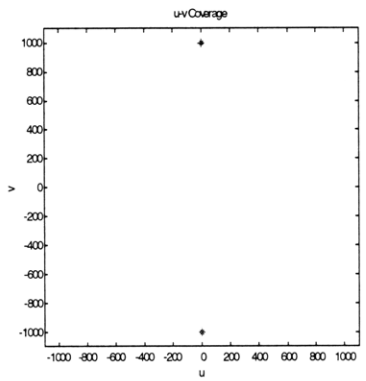
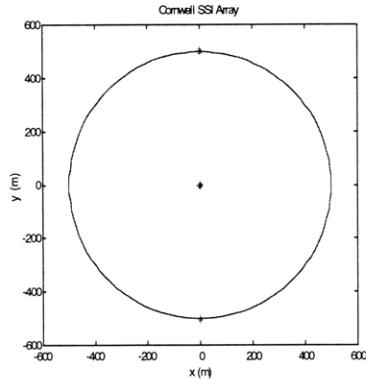
**High Resolution
(100 uv points)**



MSE=0.0653 (W/m²)²

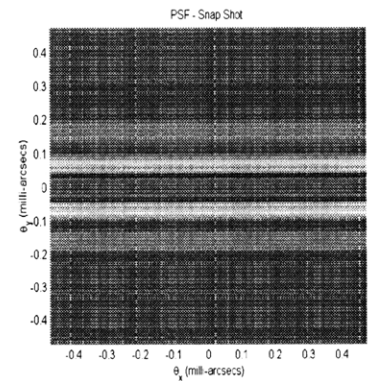
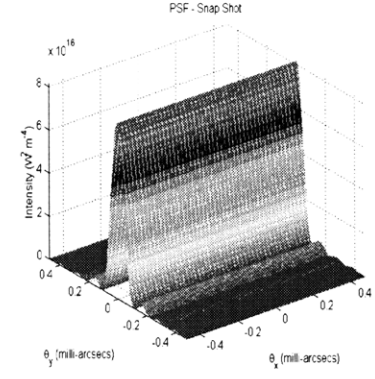
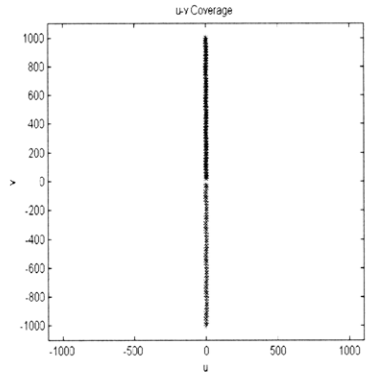
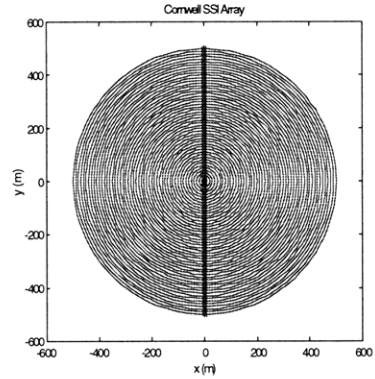
Architecture 33024

Snapshot



$MSE=0.3851 \text{ (W/m}^2\text{)}^2$

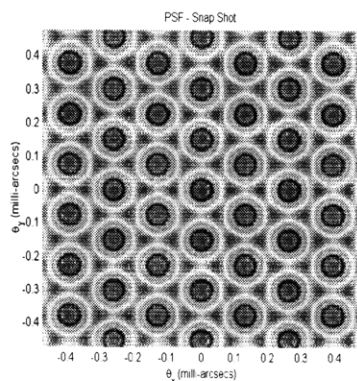
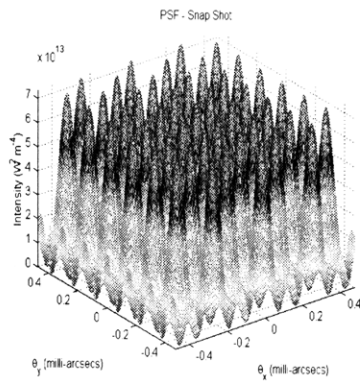
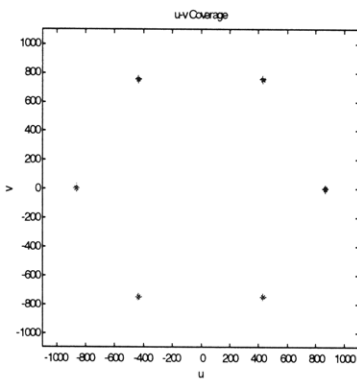
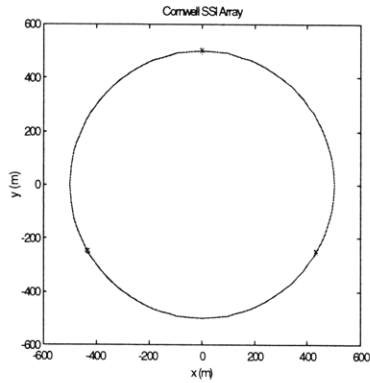
**High Resolution
(100 uv points)**



$MSE=0.0653 \text{ (W/m}^2\text{)}^2$

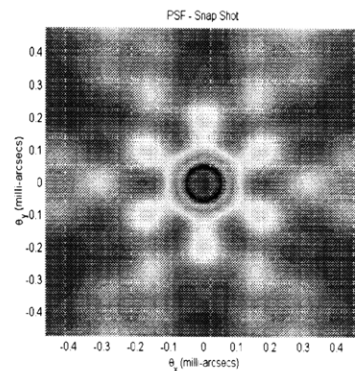
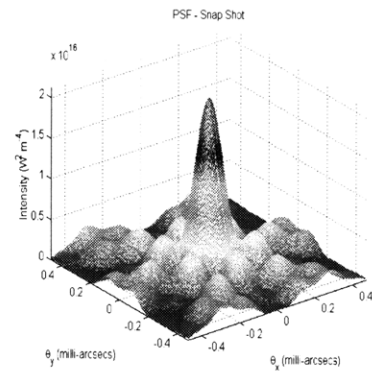
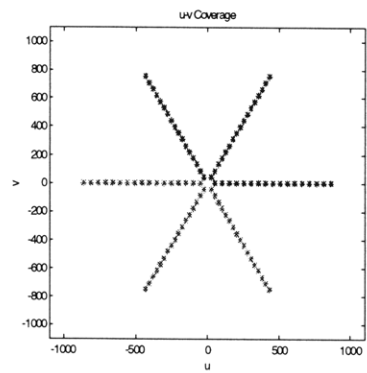
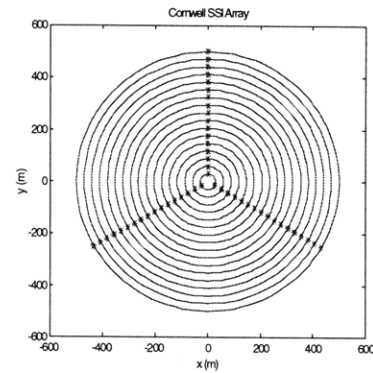
Architecture 30333

Snapshot



$MSE=0.1751 (W/m^2)^2$

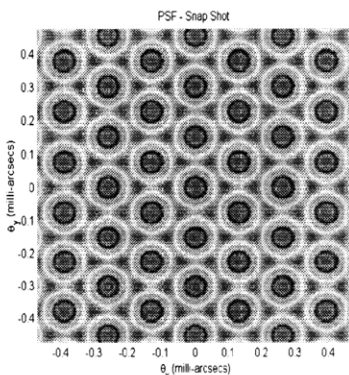
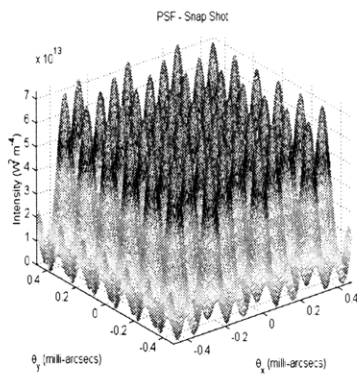
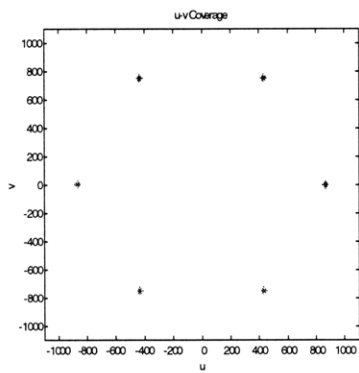
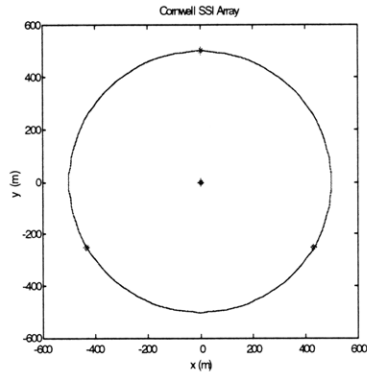
High Resolution (100 uv points)



$MSE=0.0069 (W/m^2)^2$

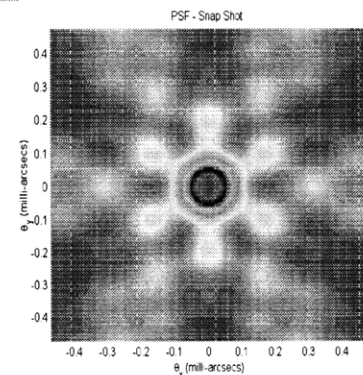
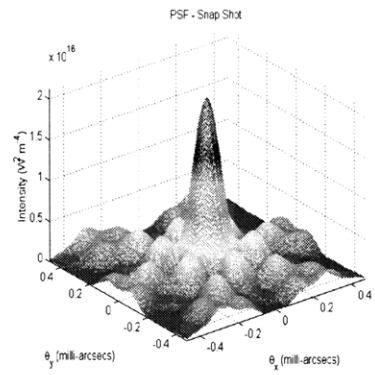
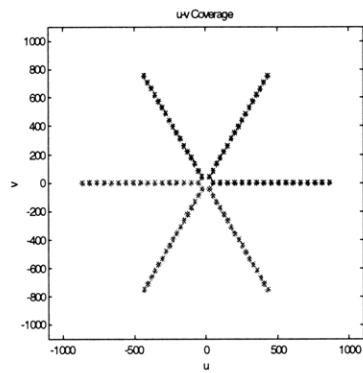
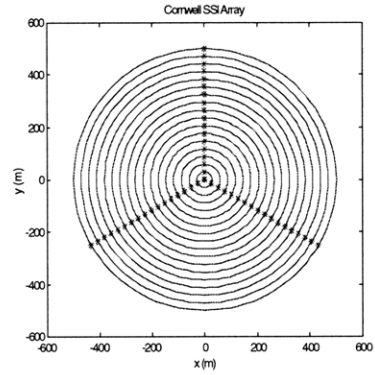
Architecture 44013

Snapshot



$MSE=0.1751 \text{ (W/m}^2\text{)}^2$

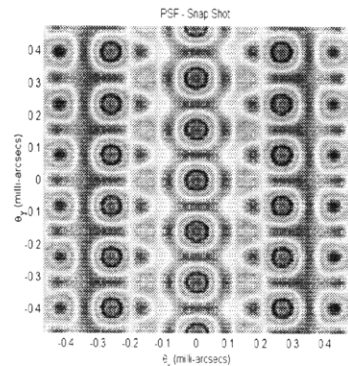
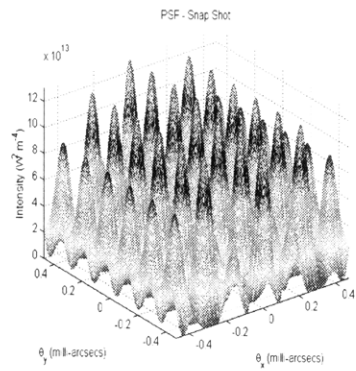
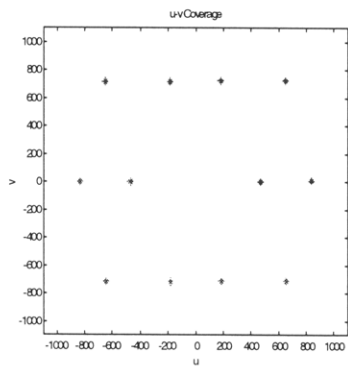
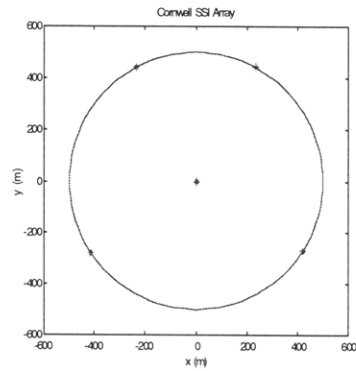
**High Resolution
(100 uv points)**



$MSE=0.0069 \text{ (W/m}^2\text{)}^2$

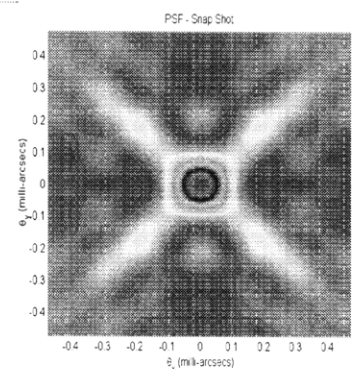
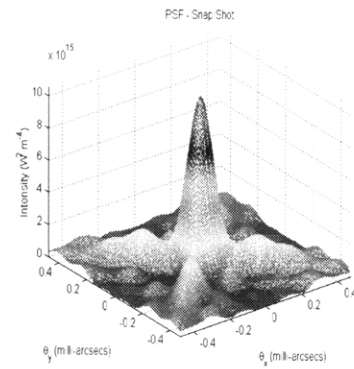
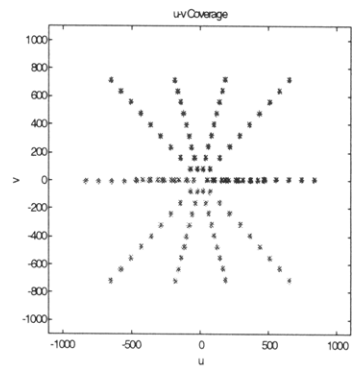
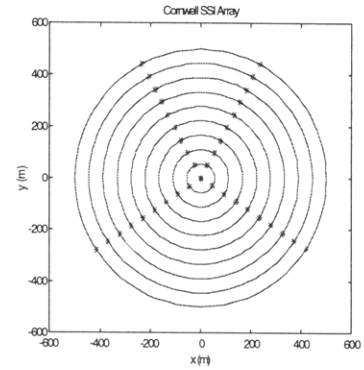
Architecture 55014

Snapshot



MSE=0.1034 (W/m^2)²

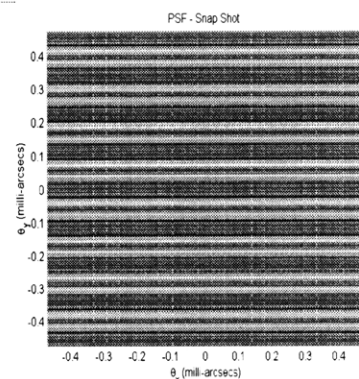
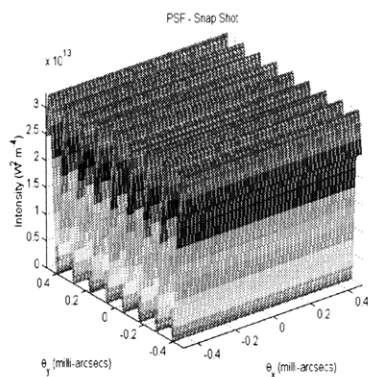
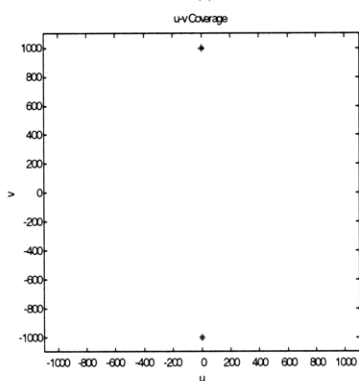
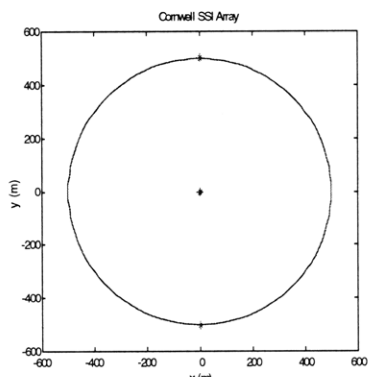
**High Resolution
(100 uv points)**



MSE=0.0653 (W/m^2)²

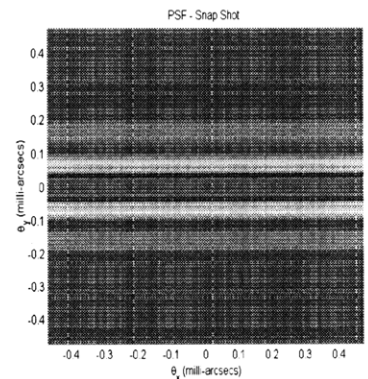
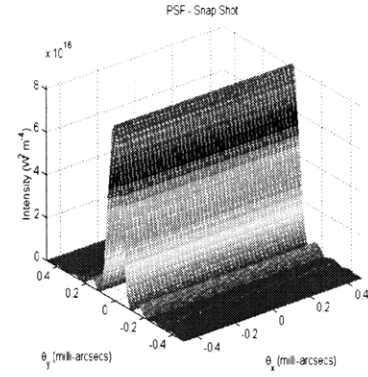
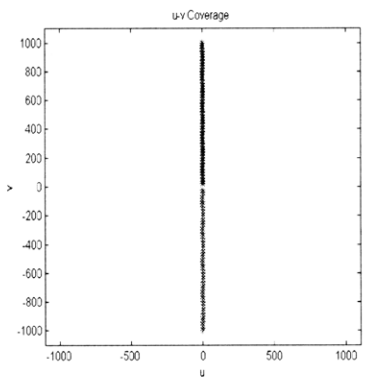
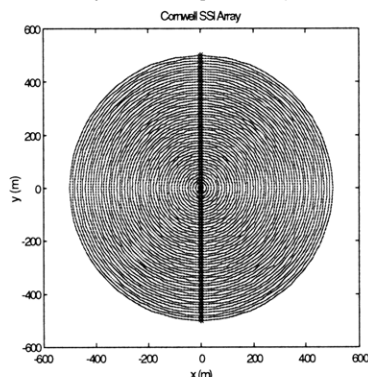
Architecture 44022

Snapshot



MSE=0.3851 (W/m²)²

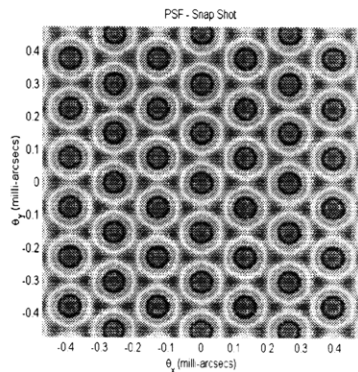
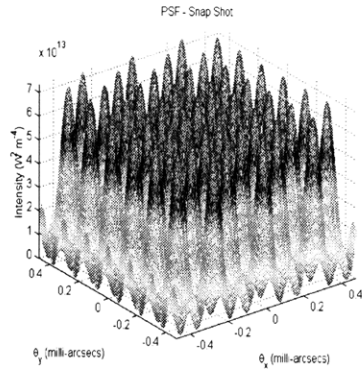
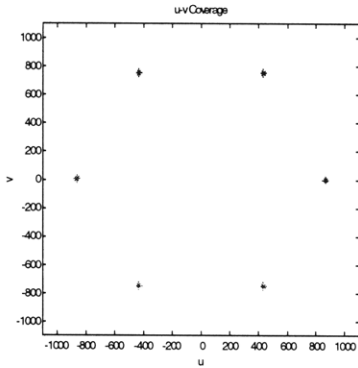
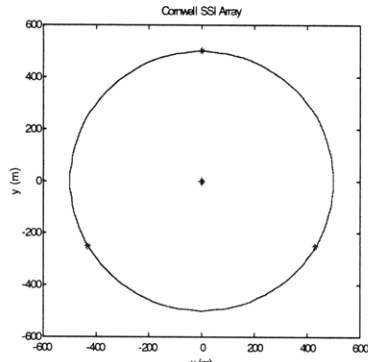
**High Resolution
(100 uv points)**



MSE=0.0045 (W/m²)²

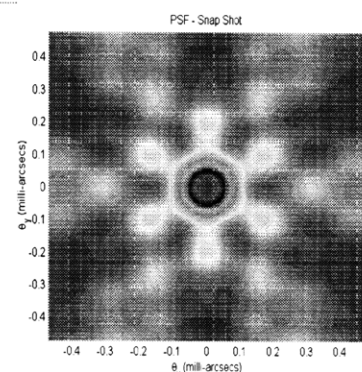
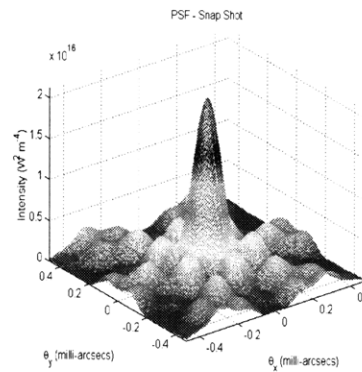
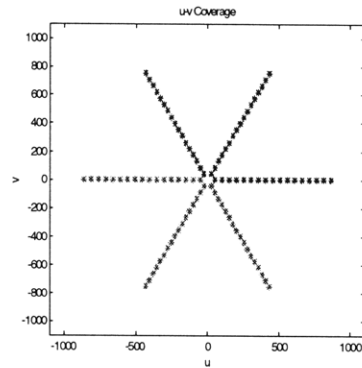
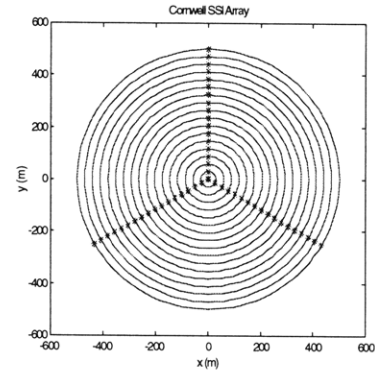
Architecture 55023

Snapshot



$$\text{MSE} = 0.1751 \text{ (W/m}^2\text{)}^2$$

**High Resolution
(100 uv points)**



$$\text{MSE} = 0.0069 \text{ (W/m}^2\text{)}^2$$

Appendix B: Imaging Rate Results

Architecture 33012

| Imaging Task | Total Time (hours) |
|---|-------------------------------|
| Acquire Target | 8.3 |
| Acquire Metrology | 0.42 |
| Equalize Science Light Pathlengths | 0.83 |
| Search for and Acquire Fringes | 13.9 |
| Science Light Integration & Measurement | 0.83 |
| New Baseline Selection | 0.42 |
| Array Reconfiguration | 24.9 |
| Total Imaging Time | 49.6 |

Architecture 31223

| Imaging Task | Total Time (hours) |
|---|-------------------------------|
| Acquire Target | 4.2 |
| Acquire Metrology | 0.42 |
| Equalize Science Light Pathlengths | 0.83 |
| Search for and Acquire Fringes | 13.9 |
| Science Light Integration & Measurement | 0.23 |
| New Baseline Selection | 0.42 |
| Array Reconfiguration | 17.8 |
| Total Imaging Time | 37.8 |

Architecture 33022

| Imaging Task | Total Time (hours) |
|---|-------------------------------|
| Acquire Target | 8.3 |
| Acquire Metrology | 0.42 |
| Equalize Science Light Pathlengths | 0.83 |
| Search for and Acquire Fringes | 13.9 |
| Science Light Integration & Measurement | 0.83 |
| New Baseline Selection | 0.42 |
| Array Reconfiguration | 24.9 |
| Total Imaging Time | 49.6 |

Architecture 33013

| Imaging Task | Total Time (hours) |
|---|-------------------------------|
| Acquire Target | 8.3 |
| Acquire Metrology | 0.42 |
| Equalize Science Light Pathlengths | 0.83 |
| Search for and Acquire Fringes | 13.9 |
| Science Light Integration & Measurement | 0.83 |
| New Baseline Selection | 0.42 |
| Array Reconfiguration | 24.9 |
| Total Imaging Time | 49.6 |

Architecture 33014

| Imaging Task | Total Time (hours) |
|---|-------------------------------|
| Acquire Target | 8.3 |
| Acquire Metrology | 0.42 |
| Equalize Science Light Pathlengths | 0.83 |
| Search for and Acquire Fringes | 13.9 |
| Science Light Integration & Measurement | 0.83 |
| New Baseline Selection | 0.42 |
| Array Reconfiguration | 24.9 |
| Total Imaging Time | 49.6 |

Architecture 33024

| Imaging Task | Total Time (hours) |
|---|-------------------------------|
| Acquire Target | 8.3 |
| Acquire Metrology | 0.42 |
| Equalize Science Light Pathlengths | 0.83 |
| Search for and Acquire Fringes | 13.9 |
| Science Light Integration & Measurement | 0.83 |
| New Baseline Selection | 0.42 |
| Array Reconfiguration | 24.9 |
| Total Imaging Time | 49.6 |

Architecture 30333

| Imaging Task | Total Time (hours) |
|---|-------------------------------|
| Acquire Target | 2.7 |
| Acquire Metrology | 0.13 |
| Equalize Science Light Pathlengths | 0.83 |
| Search for and Acquire Fringes | 13.9 |
| Science Light Integration & Measurement | 0.83 |
| New Baseline Selection | 0.42 |
| Array Reconfiguration | 13.8 |
| Total Imaging Time | 32.6 |

Architecture 44013

| Imaging Task | Total Time (hours) |
|---|-------------------------------|
| Acquire Target | 2.7 |
| Acquire Metrology | 0.13 |
| Equalize Science Light Pathlengths | 0.83 |
| Search for and Acquire Fringes | 13.9 |
| Science Light Integration & Measurement | 0.83 |
| New Baseline Selection | 0.42 |
| Array Reconfiguration | 13.8 |
| Total Imaging Time | 32.6 |

Architecture 55014

| Imaging Task | Total Time (hours) |
|---|-------------------------------|
| Acquire Target | 1.3 |
| Acquire Metrology | 0.07 |
| Equalize Science Light Pathlengths | 0.83 |
| Search for and Acquire Fringes | 13.9 |
| Science Light Integration & Measurement | 0.83 |
| New Baseline Selection | 0.42 |
| Array Reconfiguration | 9.5 |
| Total Imaging Time | 26.9 |

Architecture 44022

| Imaging Task | Total Time (hours) |
|---|-------------------------------|
| Acquire Target | 8.3 |
| Acquire Metrology | 0.42 |
| Equalize Science Light Pathlengths | 0.42 |
| Search for and Acquire Fringes | 6.9 |
| Science Light Integration & Measurement | 0.42 |
| New Baseline Selection | 0.21 |
| Array Reconfiguration | 24.9 |
| Total Imaging Time | 41.7 |

Architecture 55023

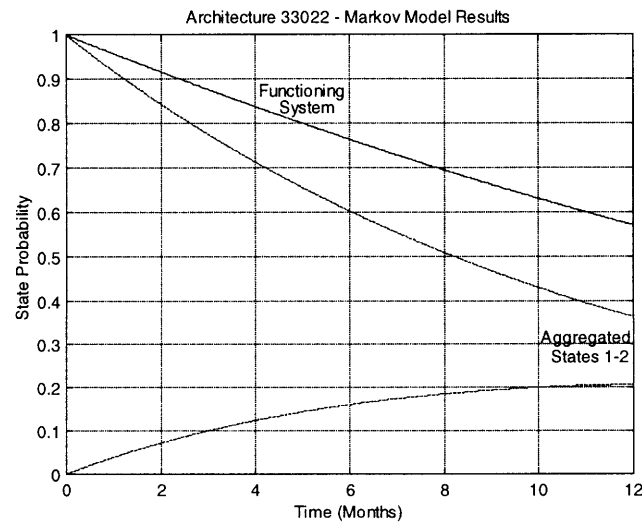
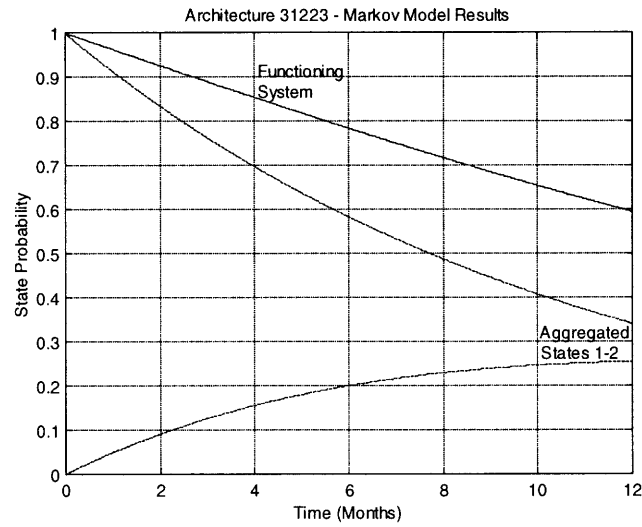
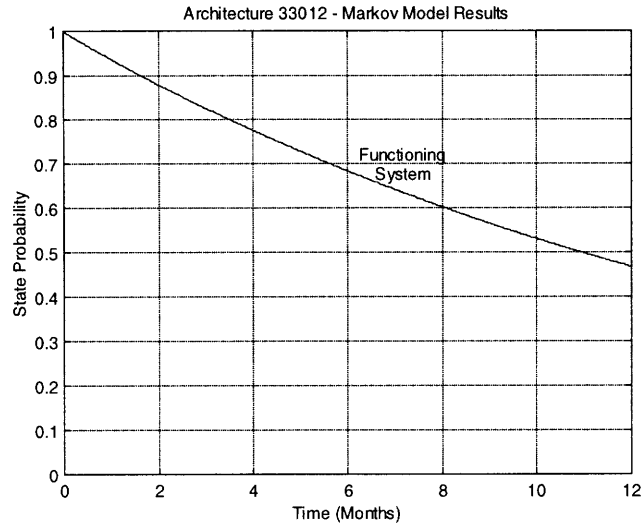
| Imaging Task | Total Time (hours) |
|---|-------------------------------|
| Acquire Target | 2.7 |
| Acquire Metrology | 0.13 |
| Equalize Science Light Pathlengths | 0.42 |
| Search for and Acquire Fringes | 6.9 |
| Science Light Integration & Measurement | 0.42 |
| New Baseline Selection | 0.21 |
| Array Reconfiguration | 13.8 |
| Total Imaging Time | 24.6 |

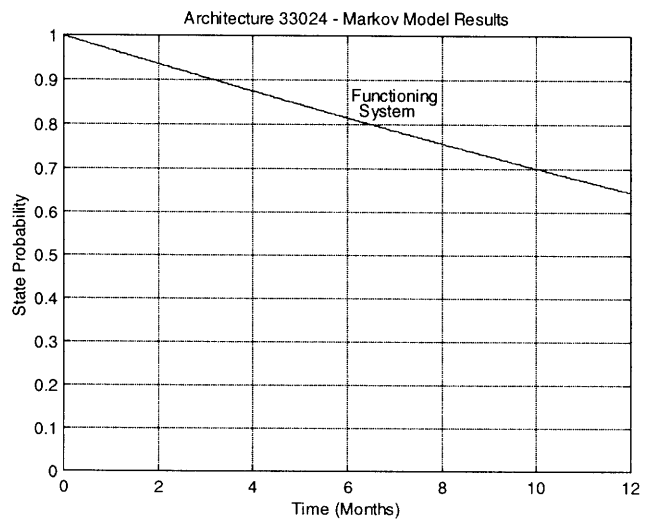
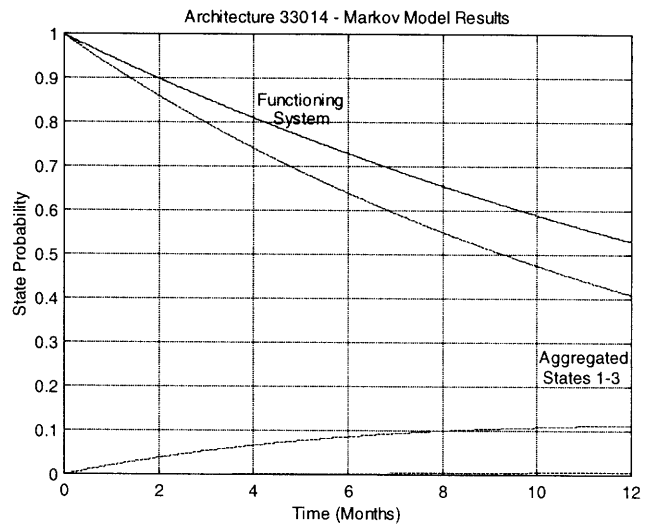
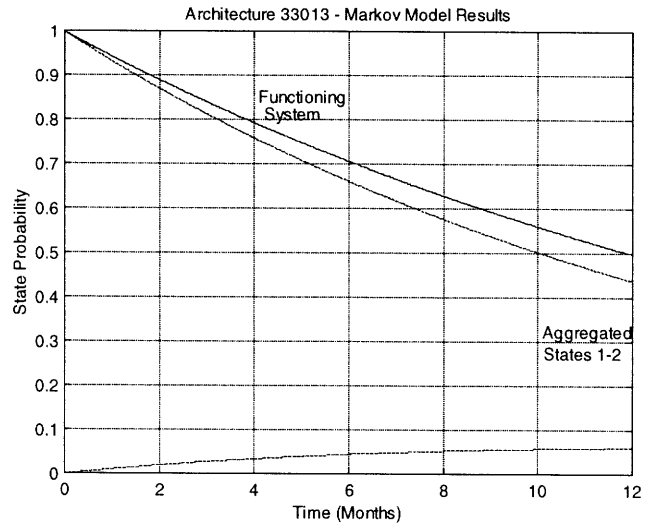
Appendix C: Markov Model Results

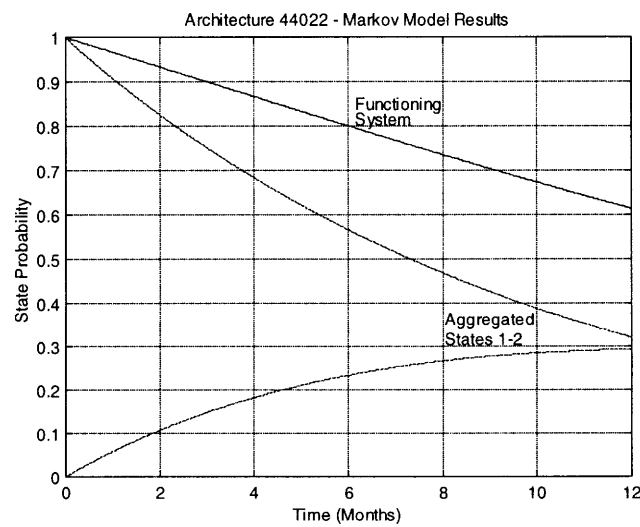
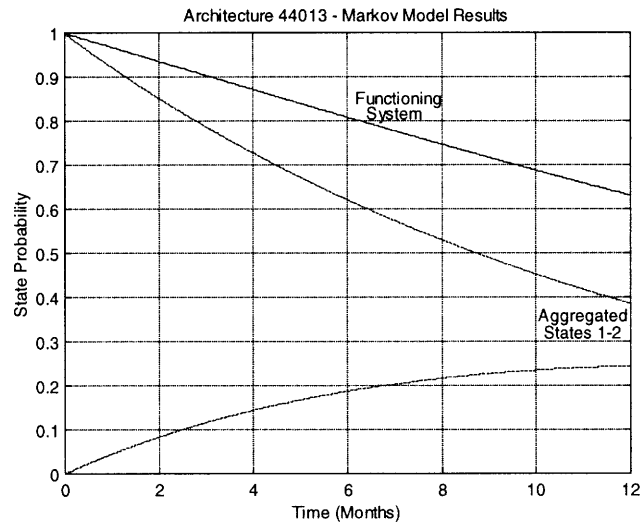
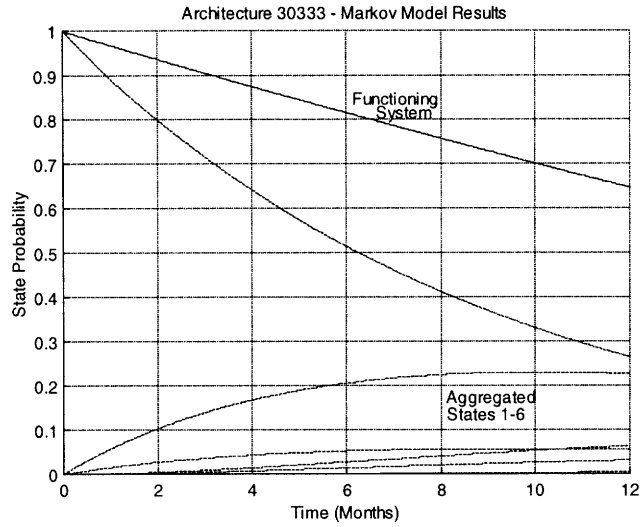
As one can see from Equations 5.16-5.48 for modeling the three-spacecraft MAMSC architecture, Markov models can increase in size very quickly. Table C.1 lists the number of differential equations required to model each of the eleven SSI architectures considered in this thesis. The figures in this Appendix plot the aggregated state probabilities for each architecture over the one-year mission design life. These models allow us to make educated predictions on the state of complex systems over time, and are a powerful tool for the design and analysis of Distributed Satellite Systems.

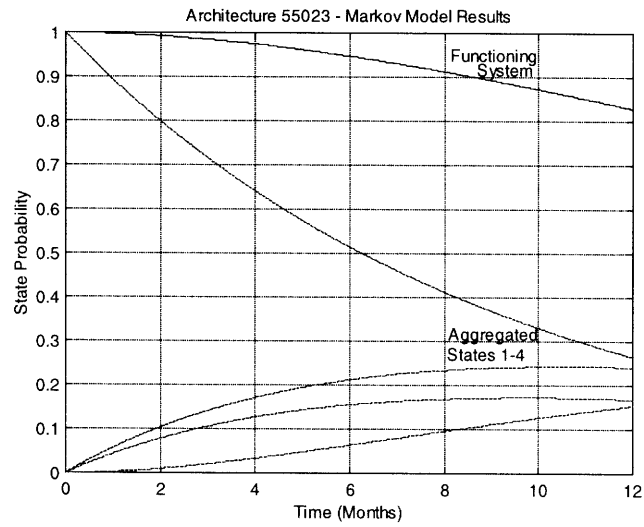
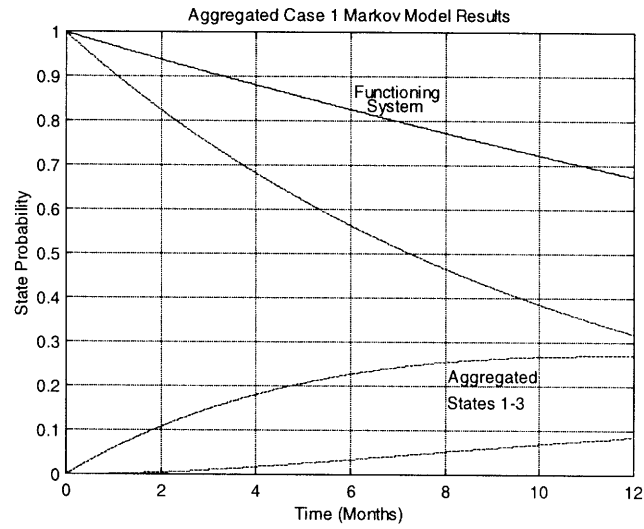
Table 5.1: SSI Architecture Markov Model Sizes

| Architecture | # of Differential Equations in Markov Model |
|--------------|---|
| 33012 | 1 |
| 31223 | 9 |
| 33022 | 3 |
| 33013 | 3 |
| 33014 | 13 |
| 33024 | 79 |
| 30333 | 43 |
| 44013 | 7 |
| 55014 | 57 |
| 44022 | 5 |
| 55023 | 59 |









Appendix D: Cost Model Results

Architecture 33012

| | Absolute Cost (\$M) | % of Total Mission Cost |
|---------------------------|--------------------------------|------------------------------------|
| Payloads | 32.9 | 28.9 |
| Buses | 30.9 | 27.2 |
| Launch(es) | 44 | 38.7 |
| Operations (1 yr.) | 5.9 | 5.2 |
| Totals | 113.7 | 100 |

Architecture 31223

| | Absolute Cost (\$M) | % of Total Mission Cost |
|---------------------------|--------------------------------|------------------------------------|
| Payloads | 55.5 | 35.3 |
| Buses | 49.1 | 31.2 |
| Launch(es) | 46 | 29.3 |
| Operations (1 yr.) | 6.6 | 4.2 |
| Totals | 157.2 | 100 |

Architecture 33022

| | Absolute Cost (\$M) | % of Total Mission Cost |
|---------------------------|--------------------------------|------------------------------------|
| Payloads | 48.1 | 31.0 |
| Buses | 56.8 | 36.6 |
| Launch(es) | 44 | 28.3 |
| Operations (1 yr.) | 6.5 | 4.2 |
| Totals | 155.4 | 100 |

Architecture 33013

| | Absolute Cost (\$M) | % of Total Mission Cost |
|---------------------------|--------------------------------|------------------------------------|
| Payloads | 40.3 | 31.5 |
| Buses | 37.4 | 29.3 |
| Launch(es) | 44 | 34.4 |
| Operations (1 yr.) | 6.1 | 4.8 |
| Totals | 127.8 | 100 |

Architecture 33014

| | Absolute Cost (\$M) | % of Total Mission Cost |
|---------------------------|--------------------------------|------------------------------------|
| Payloads | 47.4 | 34.1 |
| Buses | 41.5 | 29.8 |
| Launch(es) | 44 | 31.6 |
| Operations (1 yr.) | 6.2 | 4.5 |
| Totals | 139.1 | 100 |

Architecture 33024

| | Absolute Cost (\$M) | % of Total Mission Cost |
|---------------------------|--------------------------------|------------------------------------|
| Payloads | 62.6 | 36.1 |
| Buses | 48.8 | 28.1 |
| Launch(es) | 56 | 32.3 |
| Operations (1 yr.) | 6.2 | 3.6 |
| Totals | 173.6 | 100 |

Architecture 30333

| | Absolute Cost (\$M) | % of Total Mission Cost |
|---------------------------|--------------------------------|------------------------------------|
| Payloads | 70.1 | 36.7 |
| Buses | 58.1 | 30.4 |
| Launch(es) | 56 | 29.3 |
| Operations (1 yr.) | 6.9 | 3.6 |
| Totals | 191.1 | 100 |

Architecture 44013

| | Absolute Cost (\$M) | % of Total Mission Cost |
|---------------------------|--------------------------------|------------------------------------|
| Payloads | 40.3 | 30.6 |
| Buses | 38.9 | 29.5 |
| Launch(es) | 44 | 33.4 |
| Operations (1 yr.) | 8.6 | 6.5 |
| Totals | 127.8 | 100 |

Architecture 55014

| | Absolute Cost (\$M) | % of Total Mission Cost |
|---------------------------|--------------------------------|------------------------------------|
| Payloads | 47.4 | 31.8 |
| Buses | 46.6 | 31.3 |
| Launch(es) | 44 | 29.6 |
| Operations (1 yr.) | 10.9 | 7.3 |
| Totals | 148.9 | 100 |

Architecture 44022

| | Absolute Cost (\$M) | % of Total Mission Cost |
|---------------------------|--------------------------------|------------------------------------|
| Payloads | 48.1 | 33.5 |
| Buses | 42.9 | 29.9 |
| Launch(es) | 44 | 30.7 |
| Operations (1 yr.) | 8.5 | 5.9 |
| Totals | 143.5 | 100 |

Architecture 55023

| | Absolute Cost (\$M) | % of Total Mission Cost |
|---------------------------|--------------------------------|------------------------------------|
| Payloads | 55.5 | 33.4 |
| Buses | 50.9 | 30.6 |
| Launch(es) | 46 | 27.7 |
| Operations (1 yr.) | 13.9 | 8.4 |
| Totals | 166.3 | 100 |

30-12